



## 저작자표시-비영리-변경금지 2.0 대한민국

이용자는 아래의 조건을 따르는 경우에 한하여 자유롭게

- 이 저작물을 복제, 배포, 전송, 전시, 공연 및 방송할 수 있습니다.

다음과 같은 조건을 따라야 합니다:



저작자표시. 귀하는 원저작자를 표시하여야 합니다.



비영리. 귀하는 이 저작물을 영리 목적으로 이용할 수 없습니다.



변경금지. 귀하는 이 저작물을 개작, 변형 또는 가공할 수 없습니다.

- 귀하는, 이 저작물의 재이용이나 배포의 경우, 이 저작물에 적용된 이용허락조건을 명확하게 나타내어야 합니다.
- 저작권자로부터 별도의 허가를 받으면 이러한 조건들은 적용되지 않습니다.

저작권법에 따른 이용자의 권리는 위의 내용에 의하여 영향을 받지 않습니다.

이것은 [이용허락규약\(Legal Code\)](#)을 이해하기 쉽게 요약한 것입니다.

[Disclaimer](#)

공학박사 학위논문

**Preparation of Polymeric Nanofiber Composites  
Using Simultaneous Electrospinning/Electrospraying  
and Their Application to Protective Materials**

전기방사/전기분무 동시시행을 이용한

고분자 나노섬유 복합체 제조 및

이들의 보호소재 응용에 관한 연구

2016년 8월

서울대학교 대학원

재료공학부

류 수 열

# Preparation of Polymeric Nanofiber Composites Using Simultaneous Electrospinning/Electrospraying and Their Application to Protective Materials






전기방사/전기분무 동시시행을 이용한 고분자 나노섬유 복합체 제조  
및 이들의 보호소재 응용에 관한 연구

지도교수 곽 승 엽

이 논문을 공학박사 학위논문으로 제출함  
2016년 4월

서울대학교 대학원  
재료공학부  
류 수 열

류수열의 공학박사 학위논문을 인준함  
2016년 6월

위 원 장	강 지 영	
부위원장	곽 승 엽	
위 원	유 응 멸	
위 원	김 승 석	
위 원	정 재 우	

## **Abstract**

# **Preparation of Polymeric Nanofiber Composites Using Simultaneous Electrospinning/Electrospraying and Their Application to Protective Materials**

Su-Yeol Ryu

Department of Materials Science and Engineering

The Graduate School

Seoul National University

Nanomaterials demonstrate interesting physical and chemical properties compared with conventional materials. Various types of new materials, such as nanoparticle, nanorod, nanosphere and nanofiber, have been investigated. The creation of new functional nanomaterials contributes significantly to the innovation of nanoscience and nanotechnologies. Among them, electrospun nanofibers have been attracting the attention of highly functional materials due to their enhanced properties, such as high surface to volume ratio, very high porosity compared to other conventional fibers. So, nanofibers have been studied for various applications in fields of filtration, tissue engineering, sensor, protective material, electronic and photonic material and drug delivery. In

this study, the polymeric nanofiber composites were developed using simultaneous electrospinning/electrospraying, then applied to protective materials. In chapter 2, two types of electrospun polyamide nanofiber composites in which Ag-TiO<sub>2</sub> was located either in the interior or on the surface of the nanofiber using electrospinning and simultaneous electrospinning/electrospray (SEE) process, respectively. The performance of the obtained Ag-TiO<sub>2</sub>-embedded nanofiber composite (interior located Ag-TiO<sub>2</sub>: AT-*in*-NF) and Ag-TiO<sub>2</sub>-decorated nanofiber composite (surface located Ag-TiO<sub>2</sub>: AT-*sur*-NF) was compared by evaluating the decolorization of methylene blue (MB) stain and their antimicrobial ability. It was concluded that the positioning of nanomaterial additives is a crucial factor in the enhanced performance of such nanofiber composites, and provide a guide for designing and optimizing nanofiber composites with superior catalytic activities. In chapter 3, a potential application of nanofibrous composite materials impregnated the MgO and POM adsorbents was exhibited as an inner layer for the permeable protective clothing against CWA. The nanofiber composites, which were consisted of both polyamide nanofiber and adsorbents (MgO and POM), were prepared using the SEE process. The nanofiber composites were compared to neat polyamide nanofiber mat by evaluating the permeability of air, moisture and protectability against gas chemical warfare simulants. It was

suggested that the high possibility of the application of the nanofiber composites to the inner layer of permeable protective clothing. In chapter 4, it was reported that electrospun *meta*-aramid nanofibers with enhanced chemical stability and mechanical property using sequential post-treatment for removal of salt in the nanofiber and regeneration of crystalline structure. The aligned *meta*-aramid nanofibers with LiCl salt was prepared using electrospinning apparatus with drum-collector. The washing and heating sequential post-treated nanofiber mats showed improved chemicals stability. Furthermore, in order to estimate the possibility of their application to an outer layer for permeable protective clothing having the repellency against liquid chemical warfare simulants, the surface of *meta*-aramid nanofibers was modified via treatment using water and oil repellent. In chapter 5, lightweight nanofibrous assemblies with high protection ability against chemical warfare agents (CWAs) were developed using laminated outer and inner layers based on aromatic and aliphatic polyamide nanofiber composites with CWA adsorbents magnesium oxide and polyoxometalate. Thickness, weight density (weight per area), cool/warm feeling and air/moisture permeability of the assembly were compared with the permeable protective clothing of Korea Army as a reference. The thickness and weight density were varied according to the number of stacking, and finally, the lightweight assemblies

with high protectability against CWA can be developed. The assembly surpassed the reference in the cool feeling property, and provided good resistance to the penetration of chemical warfare agents in gas form, while still allowing significant water vapor transmission to promote evaporate cooling of the body. The development of the assembly suggests new approach to improving performance of a permeable protective materials, and provides a guide for designing and optimizing the permeable protective clothing.

**Keywords:** Nanofiber, Composite, Electrospinning, Electrospraying,  
Polyamide, *meta*-Aramid, Amphiphobicity, Protective material,  
Chemical warfare agent, Chemical warfare simulant.

**Student Number:** 2006-20861

# Contents

## **Chapter 1 Introduction..... 1**

1.1	Nanofiber .....	1
1.2	Electrospinning Process .....	9
1.2.1	Polymer solution parameter (materials variables).....	9
1.2.2	Processing parameter (processing variables) .....	13
1.2.3	Example: electrospinning condition of polyamide 66 .....	17
1.3	Application of Electrospun Nanofibers.....	21
1.3.1	Tissue scaffolds.....	21
1.3.2	Filtration.....	24
1.3.3	Protective clothing materials.....	25
1.3.4	Energy generation .....	26
1.3.5	Reinforcement materials .....	27
1.3.6	Cosmetics .....	28
1.4	Summary .....	29
1.5	Research Objectives .....	30

## **Chapter 2 Ag-TiO<sub>2</sub> Decorated Nylon 66 Nanofibrous Protective Materials with both Self-Cleaning and Antimicrobial Activities..... 37**

2.1	Introduction.....	37
2.2	Experiments .....	40
2.2.1	Preparation and characterization of Ag-TiO <sub>2</sub> .....	40
2.2.2	Preparation and characterization of Ag-TiO <sub>2</sub> -embedded and decorated nanofiber composites .....	41



2.3	Results and Discussion .....	46
2.3.1	Preparation and characterization of Ag-TiO <sub>2</sub> .....	46
2.3.2	Characteristics of Ag-TiO <sub>2</sub> -embedded and decorated nanofiber composites.....	55
2.3.3	Photocatalytic and antimicrobial activities of Ag-TiO <sub>2</sub> -embedded and decorated nanofiber composites ..	60
2.4	Summary .....	67

## **Chapter 3 Nanofibrous Inner Layer of Chemical Warfare Protective Materials with Adsorptivity of Chemical Warfare Agents..... 71**

3.1	Introduction .....	71
3.2	Experiments .....	76
3.2.1	Adsorptivity of chemical warfare agent simulants on MgO and POM particles .....	76
3.2.2	Nanofibrous inner layer for adsorptive protection against chemical warfare simulants .....	77
3.3	Results and Discussion .....	84
3.3.1	Adsorptivity of chemical warfare agent simulants on MgO and POM particles .....	84
3.3.2	Nanofibrous inner layer for adsorptive protection against chemical warfare simulants .....	87
3.4	Summary .....	100

## **Chapter 4 Nanofibrous Outer Layer of Chemical Warfare Protective Materials with Repellency of Chemical Warfare Agents ..... 103**

4.1	Introduction .....	103
4.2	Experiments .....	108
4.2.1	Materials .....	108
4.2.2	Optimization of preparation condition for <i>meta</i> -aramid nanofiber mat with improved chemical stability and mechanical property.....	109
4.2.3	Nanofibrous outer layer for repellent protection against chemical warfare agent simulants.....	113
4.3	Results and Discussion .....	118
4.3.1	Optimization of preparation conditions for <i>meta</i> -aramid nanofiber mat with improved chemical stability and mechanical property.....	118
4.3.2	Nanofibrous outer layer for repellent protection against chemical warfare agent simulants.....	135
4.4	Summary .....	144

## **Chapter 5 Multilayer Assemblies of Nanofiber Composites as Permeable Protective Materials against Chemical Warfare Agents..... 147**

5.1	Introduction .....	147
5.2	Experiments .....	151
5.2.1	Assembly of the outer and inner layers for nanofibrous protective materials against chemical warfare simulants..	151

5.2.2	Characterization of the assembly of the outer and inner layers.....	153
5.3	Results and Discussion .....	156
5.3.1	Assembly of the outer and inner layers for nanofibrous protective materials against chemical warfare simulants..	156
5.3.2	Characterization of the assembly of the outer and inner layers.....	157
5.4	Summary .....	172

<b>Conclusion.....</b>	<b>175</b>
------------------------	------------

<b>Korean Abstract .....</b>	<b>177</b>
------------------------------	------------

<b>List of Papers, Patents and Symposiums .....</b>	<b>180</b>
---	------------

## List of Tables

Table 2.1	Sample code and appearance of P25 and Ag-TiO <sub>2</sub> nanoparticles with various Ag contents .....	51
Table 3.1	Chemical warfare agent simulants (2-CEES and DMMP) adsorptivity of MgO and POM particles.....	86
Table 3.2	Mechanical properties of pristine polyamide 66 nanofiber (PANF) and nanofiber composites ([I]MgO/PANF and [I]POM/PANF).....	95
Table 3.3	Air permeability and water vapor transmittance rate of the nanofiber mats.....	97
Table 3.4	Permeation test of the simulant of chemical warfare agents through the nanofiber mats .....	99
Table 5.1	Weight, thickness and maximum heat transfer rate ( $q_{\max}$ ) of the assembled nanofiber composites	161
Table 5.2	Air permeability and water vapor transmission of the assembled nanofiber composites.....	164
Table 5.3	Permeation test of the simulant of chemical warfare agents through the assemblies.....	170

## **List of Figures**

Figure 1.1	The unique feature of nanofibers compared to a human hair, which has a diameter around 80 $\mu\text{m}$ and it is about 200 times bigger in diameter than nanofibers .....	2
Figure 1.2	Various techniques to prepare polymeric nanofibers except for the electrospinning: (A) Drawing, (B) Templating, (C) Self-assembly, (D) Phase separation, (E) Meltblowing, (F) Rotary jet-spinning .....	4
Figure 1.3	Schematic of electrospinning process. (A) Apparatus of electrospinning, (B) How the formation of charge in the Taylor cone, and (C) Diagram showing flight of nanofiber during electrospinning .....	8
Figure 1.4	Parameters affecting electrospinning process ...	10
Figure 1.5	Optimal electrospinning conditions for (A) 10 wt%, (B) 15 wt% and (C) 20 wt% PA66 solution without the salt and (D) 10 wt%, (E) 15 wt% and (F) 20 wt% PA66 solution with the BTMAC salt. Bright space means the good spinnable zone....	19

Figure 1.6	Morphologies of electrospun PA66 nanofibers (A) without salt at 10 wt%, 0.5 mL/h, 9 cm and 25 kV, (B) without salt at 15 wt%, 0.5 mL/h, 9 cm and 25 kV, (C) without salt at 20 wt%, 0.5 mL/h, 6 cm and 25 kV, (D) with BTMAC at 10 wt%, 0.5 mL/h, 12 cm and 25 kV, (E) with BTMAC at 15 wt%, 1.5 mL/h, 6 cm and 19 kV, and (F) with BTMAC at 20 wt%, 0.5 mL/h, 9 cm and 20 kV. Scale bar means 1 $\mu\text{m}$ .....	20
Figure 1.7	Applications of electrospun nanofibers in various fields .....	23
Figure 1.8	Research Objectives: Development of nanofibrous protective materials .....	33
Figure 2.1	Schematic representation of (A) electrospinning process used to fabricate (B) the Ag-TiO <sub>2</sub> -embedded nanofiber composite (AT- <i>in</i> -NF); and (C) simultaneous electrospinning/electrospraying (SEE) process used to fabricate (D) the Ag-TiO <sub>2</sub> -decorated nanofiber composite (AT- <i>sur</i> -NF)....	45
Figure 2.2	Ag 3d XPS spectra of Ag-TiO <sub>2</sub> and P25. Values in round brackets indicate the atomic percent ratio of Ag/Ti.....	49

Figure 2.3 Morphologies of P25 and Ag-TiO<sub>2</sub> with various Ag content: HR-TEM and FE-SEM images of (A) Ag-TiO<sub>2</sub>(0.11), (B) Ag-TiO<sub>2</sub>(0.37), (C) Ag-TiO<sub>2</sub>(0.37), (D) Ag-TiO<sub>2</sub>(0.74), (E) Ag-TiO<sub>2</sub>(1.01), and (F) P25. Values in round brackets indicate the atomic % ratio of Ag/Ti. (B, inset) Fast Fourier transform (FFT) pattern exhibiting 0.34-nm and 0.23-nm d-spacings corresponding to the (101) plane of standard bulk anatase TiO<sub>2</sub> and the (111) plane of metallic Ag, respectively. (C, inset) EDS mapping image; green and red dots indicate Ag and Ti elements, respectively..... 50

Figure 2.4 (A) Pseudo-first-order photodegradation of methylene blue (MB) under visible light irradiation ( $\lambda = 380\text{--}480$  nm) over P25 and Ag-TiO<sub>2</sub>. The slope of the lines corresponds to the rate constant for the photodegradation of MB. (B) Rate constants for MB photodegradation over P25 and Ag-TiO<sub>2</sub> under visible light irradiation, estimated to be about  $1.73 \times 10^{-3}$ ,  $2.80 \times 10^{-3}$ ,  $3.49 \times 10^{-3}$ ,  $2.43 \times 10^{-3}$ , and  $1.58 \times 10^{-3}$  min<sup>-1</sup>,

	respectively. Values in round brackets indicate the atomic % ratio of Ag/Ti in the samples.....	54
Figure 2.5	Antimicrobial activities of Ag-TiO <sub>2</sub> photocatalysts against <i>S. aureus</i> (Gram-positive bacteria) and <i>E. coli</i> (Gram-negative bacteria). Values in round brackets indicate the atomic ratio (%) of Ag/Ti in the samples .....	56
Figure 2.6	Morphology of (A and B) the pristine nanofiber, (C) the Ag-TiO <sub>2</sub> -embedded nanofiber composite (AT- <i>in</i> -NF), (D) AT- <i>in</i> -NF observed with higher acceleration voltage to check the presence of Ag-TiO <sub>2</sub> in the interior of nanofibers, (E) as-prepared Ag-TiO <sub>2</sub> -decorated nanofiber composite (AT- <i>sur</i> -NF), and (F) heat-pressed AT- <i>sur</i> -NF .....	58
Figure 2.7	Residual weight and derivative weight loss (inset) versus temperature (heating rate of 10 °C/min) of Ag-TiO <sub>2</sub> , pristine nanofiber, Ag-TiO <sub>2</sub> -embedded nanofiber composite (AT- <i>in</i> -NF), and Ag-TiO <sub>2</sub> -decorated nanofiber composite (AT- <i>sur</i> -NF)....	59
Figure 2.8	Visible light photocatalytic decolorization of methylene blue over pristine nanofiber, Ag-TiO <sub>2</sub> -embedded nanofiber composite (AT- <i>in</i> -NF), and	



	Ag-TiO <sub>2</sub> -decorated nanofiber composite (AT- <i>sur</i> -NF). Red, yellow, and blue stickers are placed on the top left of the figures for color comparison .....	62
Figure 2.9	Dependence of color strength ( $f_k$ ) of untreated and stained samples with methylene blue (MB) on visible light irradiation ( $\lambda = 380\text{--}480$ nm): (left) pristine nanofiber, (center) Ag-TiO <sub>2</sub> -embedded nanofiber composite (AT- <i>in</i> -NF), and (right) Ag-TiO <sub>2</sub> -decorated nanofiber composite (AT- <i>sur</i> -NF) .....	63
Figure 2.10	Antimicrobial activities of pristine nanofiber, Ag-TiO <sub>2</sub> -embedded nanofiber composite (AT- <i>in</i> -NF), and Ag-TiO <sub>2</sub> -decorated nanofiber composite (AT- <i>sur</i> -NF) against <i>S. aureus</i> (Gram-positive bacteria) and <i>K. pneumoniae</i> (Gram-negative bacteria) ..	66
Figure 3.1	Schematic representations of the chemical warfare protective clothing .....	72
Figure 3.2	Schematic representations of experimental system for (A) air permeability (ASTM D737) and (B) water vapor permeability (ASTM E96) .....	82
Figure 3.3	Schematic representations of experimental system to investigate the resistance of the nanofiber	

	composites to permeation by gas CWA simulants: (A) direct contact type and (B) dynamic diffusion type .....	83
Figure 3.4	Morphology of (A and B) the [I]MgO/PANF and (C and D) the [I]POM/PANF nanofiber composites for outer layers of nanofibrous protective materials .....	90
Figure 3.5	Thermal degradation behavior (TGA) of the neat polyamide nanofiber (PANF) and nanofiber composites ([I]MgO/PANF and [I]POM/PANF).....	91
Figure 3.6	Theoretical profiles of flow pore characteristics measured by capillary flow porometry: (A) dry and wet curves indicating range of flow pore size and (B) pore size distribution. Practical profiles of flow pore characteristics of the nanofiber mats: (C) neat polyamide 66 (PANF) and (D) [I]MgO/PANF ...	96
Figure 4.1	Experimental scheme of preparing the Nomex ( <i>meta</i> -aramid) nanofiber mat with improved chemical stability and mechanical property ....	112
Figure 4.2	Schematic representation of the simultaneous electrospinning and electrospraying (SEE) process..	117

Figure 4.3	Dissolution mechanism of <i>meta</i> -aramid in DMAc/LiCl solution.....	120
Figure 4.4	Morphology and elemental analysis of pristine <i>meta</i> -aramid nanofiber ( <i>mANF</i> ) (A and B) and washed <i>mANF</i> (LiCl removed) ( <i>W-mANF</i> ) (C and D)....	121
Figure 4.5	Thermal property of the nanofiber mats. (A) DTA/TGA curves of pristine <i>meta</i> -aramid nanofiber ( <i>mANF</i> ) and washed <i>mANF</i> ( <i>W-mANF</i> ). (B) First and second (insert) scans DSC curves of <i>mANF</i> , and <i>W-mANF</i> .....	124
Figure 4.6	(A and B) Chemical structure of commercial Nomex® fiber, pristine <i>meta</i> -aramid nanofiber mat ( <i>mANF</i> ), washed <i>mANF</i> ( <i>W-mANF</i> ), heat treated <i>mANF</i> (unwashed) at 300 °C for 20 min (HT300-unW- <i>mANF</i> ), and heat treated <i>W-mANF</i> at 300 °C for 20 min (HT300-W- <i>mANF</i> ) observed by ATR FT-IR. The insert number in Figure 5b is the transmittance peak intensity ratio of the C=O...H stretching band (amide I, 1647 cm <sup>-1</sup> ) verse the aromatic C–C skeleton or C=C vibration band (1604 cm <sup>-1</sup> ) and the increasing value means the regeneration of hydrogen bonding .....	127

Figure 4.7	Chemical structure of commercial Nomex fiber observed by ATR FT-IR .....	128
Figure 4.8	Crystalline structure of pristine <i>meta</i> -aramid nanofiber ( <i>m</i> ANF), washed <i>m</i> ANF (W- <i>m</i> ANF), heat treated W- <i>m</i> ANF at 250 °C for 20 min (HT250-W- <i>m</i> ANF), heat treated unwashed- <i>m</i> ANF at 300 °C for 20 min (HT300-unW- <i>m</i> ANF), and heat treated W- <i>m</i> ANF at 300 °C for 20 min (HT300-W- <i>m</i> ANF).....	131
Figure 4.9	(A) The appearance of pristine <i>meta</i> -aramid nanofiber ( <i>m</i> ANF), washed <i>m</i> ANF (W- <i>m</i> ANF), heat treated W- <i>m</i> ANF at 250 °C for 20 min (HT250-W- <i>m</i> ANF), heat treated unwashed- <i>m</i> ANF at 300 °C for 20 min (HT300-unW- <i>m</i> ANF), and heat treated W- <i>m</i> ANF at 300 °C for 20 min (HT300-W- <i>m</i> ANF) before being soaked in DMAc. (B, C, and D) Observation of chemical stability for <i>m</i> ANF), W- <i>m</i> ANF, HT250-W- <i>m</i> ANF, HT300- unW- <i>m</i> ANF, and HT300-W- <i>m</i> ANF soaked in DMAc for 0, 12, and 24 h, respectively .....	132

Figure 4.10 Young's Modulus of pristine <i>meta</i> -aramid nanofiber ( <i>m</i> ANF), washed <i>m</i> ANF (W- <i>m</i> ANF), heat treated W- <i>m</i> ANF at 250 °C for 20 min (HT250-W- <i>m</i> ANF), heat treated unwashed- <i>m</i> ANF at 300 °C for 20 min (HT300-unW- <i>m</i> ANF), and heat treated W- <i>m</i> ANF at 300 °C for 20 min (HT300-W- <i>m</i> ANF) in the longitudinal and transversal direction .....	134
Figure 4.11 Morphology of (A and B) the [O]MgO/ <i>m</i> ANF and (C and D) the [O]POM/ <i>m</i> ANF nanofiber composites for outer layers of nanofibrous protective materials .....	138
Figure 4.12 Thermal degradation behavior (DTA/TGA) of the neat <i>m</i> ANF, as-prepared MgO/ <i>m</i> ANF, and [O]MgO/ <i>m</i> ANF .....	139
Figure 4.13 Schematic of a liquid droplet showing the quantities in Young's equation.....	142
Figure 4.14 Amphiphobic surface property of [O]MgO/ <i>m</i> ANF for outer layers of nanofibrous protective materials....	143
Figure 5.1 Fabrication process for assembly of nanofiber composites via adhesion with glue spraying and hot pressing.....	152

Figure 5.2	Schematic representations of experimental system (static diffusion procedure) to investigate the resistance of the assembly of nanofiber composites to permeation by CWA simulants .....	155
Figure 5.3	Schematic representation of the assembled nanofibrous composite composed with inner and outer layers for protective materials against chemical warfare agent (CWA).....	158
Figure 5.4	Example of permeable protective clothing against chemical warfare agents .....	159
Figure 5.5	Amphiphobic surface property of the outer layer of permeable protective clothing for Korea Army (O-KA), and the assembly incorporated with MgO and POM for nanofibrous protective materials against the simulants (2-CEES and DMMP) of the chemical warfare agents .....	166
Figure 5.6	Penetration behavior of CWA simulants through the assembly with MgO: (A) 2-CEES and (B) DMMP..	171

# **Chapter 1**

## **Introduction**

### **1.1 Nanofiber**

The nanofiber definition and terminology are based on ISO documents (ISO/TS 27687:2008 “Nanotechnologies – Terminology and definitions for nano-objects – Nanoparticle, nanofiber and nanoplate”). The definition of nanofibers is as follows: the nano-object with two similar external dimensions in the nanoscale and the third dimension significantly larger. A nanofiber can be flexible or rigid. The two similar external dimensions are considered to differ in size by less than three times and the significantly larger external dimension is considered to differ from the other two by more than three times. The largest external dimension is not necessarily in the nanoscale. The nanofiber is generally accepted as the fibers with nanoscale diameters less than 100 nm as shown Figure 1.1. This definition can be extended to include fibers as large as 1  $\mu\text{m}$  diameter in the textile industry.<sup>1</sup> Due to its dimensions and its unique features, nanofiber show an improved properties in comparison to the conventional fibers as follows: high surface-to-volume ratio, small fiber-to-fiber distance, high porosity, large specific surface area, small pore size, and high controllability. These unique characteristics plus the

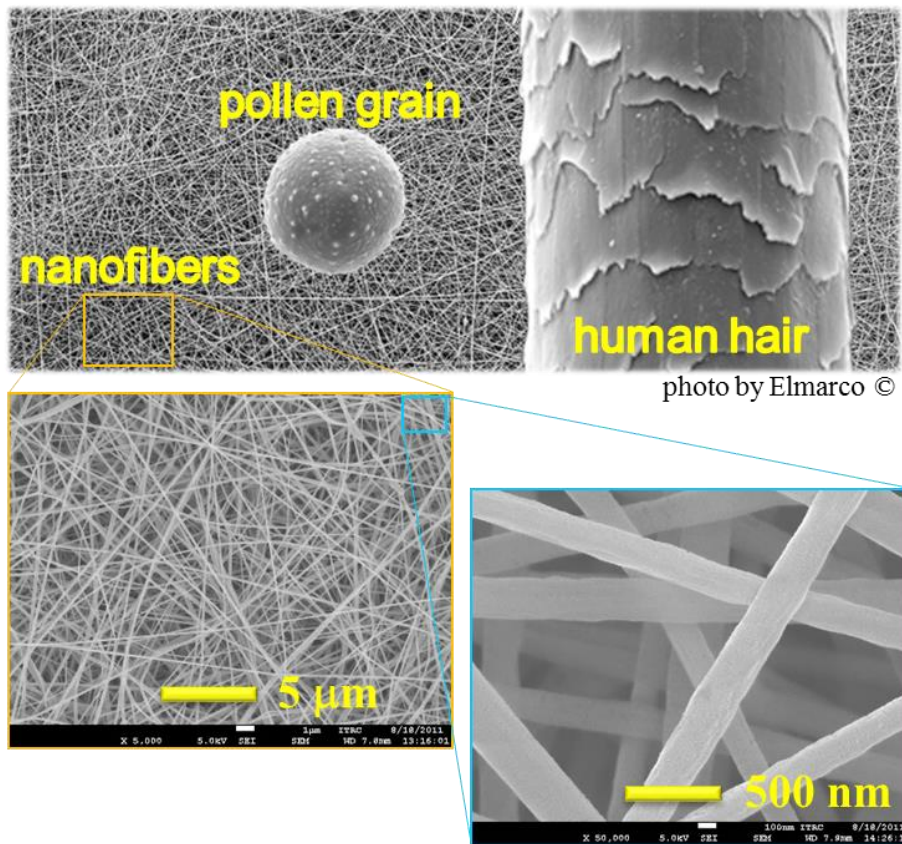


**Figure 1.1** The unique feature of nanofibers compared to a human hair, which has a diameter around 80 μm and it is about 200 times bigger in diameter than nanofibers.



functionalities from the materials themselves impart nanofibers with a number of novel properties for advanced applications.

There are various ways to make nanofibers. Polymeric nanofibers can be prepared by many techniques such as drawing, templating, self assembly, phase separation, meltblowing, rotary jet-spinning, and electrospinning, in Figure 1.2 and 1.3. In the case of the drawing, a rod was placed in a polymer melt and moved up, at a speed of approximately  $1 \times 10^{-4} \text{ ms}^{-1}$ , forming a thin filament that cooled to form a nanofiber.<sup>2</sup> The drawing of nanofibers is repeated several times on every molten droplet. The drawing process can be considered as dry spinning at a molecular level. Especially, drawing is suitable for a viscoelastic material, which can undergo strong deformations while being cohesive enough to support the stresses developed during pulling. The templating implies the use of a templates or molds, such as self-ordered porous alumina and an aluminum oxide membrane with nanoscale pores, to prepare a desired nanostructure.<sup>3</sup> The nanofiber arrays can be released from the self-ordered porous alumina template by destruction of the template or mechanical detachment. Another example, under the application of water pressure on one side and restraint from the porous membrane causes extrusion of the polymer which, upon coming into contact with a solidifying solution, gives rise to nanofibers whose diameters are determined by the pores of the membrane. The self assembly has been used for preparation of nanofibers.

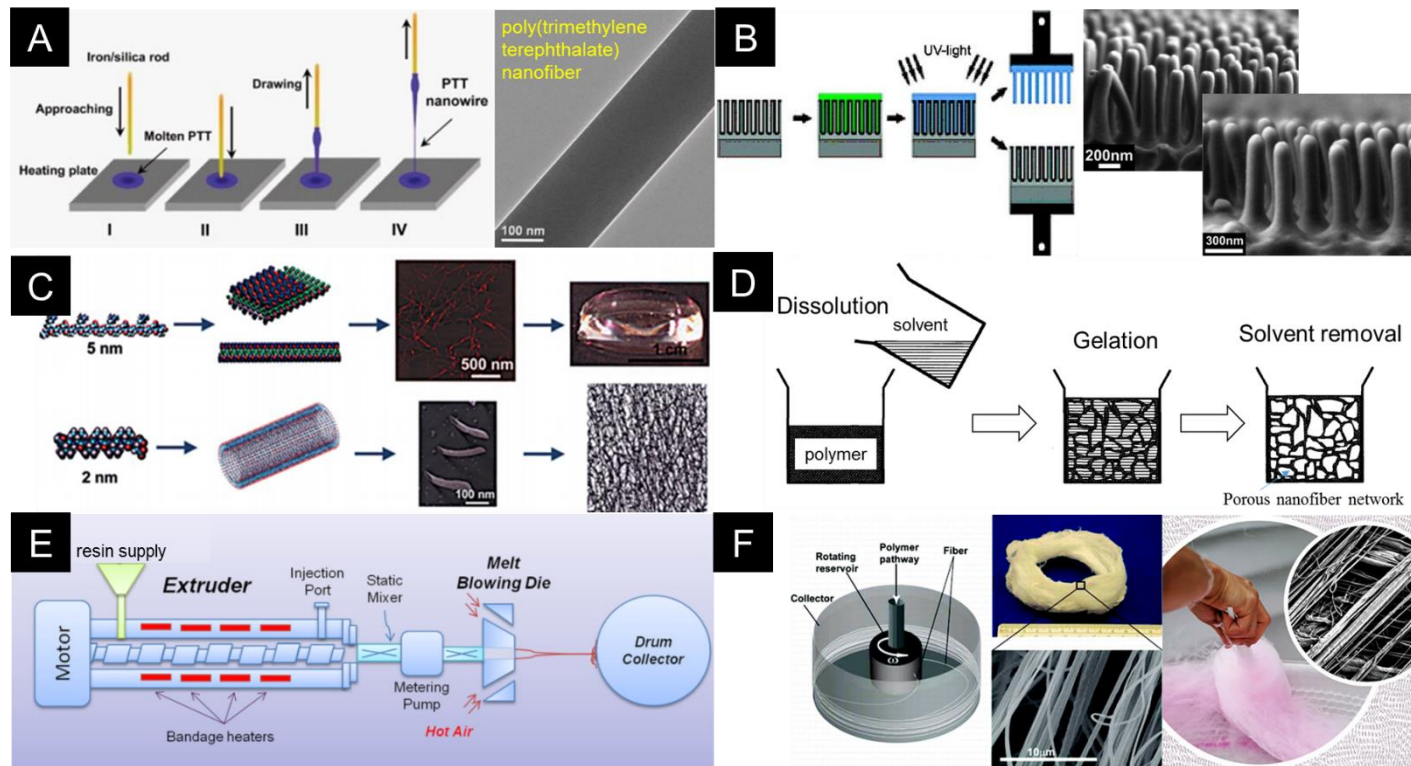


**Figure 1.2** Various techniques to prepare polymeric nanofibers except for the electrospinning: (A) Drawing, (B) Templating, (C) Self-assembly, (D) Phase separation, (E) Meltblowing, (F) Rotary jet-spinning.

Self assembly of nanofibers refer to the bottom-up fabrication of nanoscale fibers using molecules as basic unit.<sup>4</sup> The molecules organize and arrange themselves into patterns or structures through the intermolecular forces such as hydrogen bonding, hydrophobic forces, and electrostatic reactions. A small molecule is arranged in a concentric manner such that that the interaction can form among the concentrically arranged small molecules which, upon extension in the plane's normal gives the longitudinal axis of a nanofiber. The arranged small molecules forms the macromolecular nanofibers. In the case of the phase separation, the main mechanism of this method is the separation of phases due to physical incompatibility, leaving behind the other remaining phase.<sup>5</sup> First, a polymer is dissolved in a good solvent before being gelation. The polymer solution is stored at the gelation temperature. The gel was immersed in non-good solvent to allow the good solvent exchanged. And then, the gel is removed from the non-good solvent. At last, interconnected porous nanofibrous structure left behind. The nanofiber can also be formed via meltblowing.<sup>6</sup> The meltblowing, which have been used to prepare microscale fibers, produce the micro- and nanofibers by injecting molten polymer streams into high velocity gas/air jets that form a self-bonded nanofibers on a collector. The drag force caused by the hot air quickly attenuates the fiber, and reduces the diameter to nanoscale. In the case of the rotary jet-spinning, the system is consisted of a reservoir with two side wall orifices that was attached to the shaft

of a motor with controllable rotation speed. Nanofibers can be produced by exploiting a high-speed rotating nozzle to form a polymer jet which undergoes extension along the rotation direction before solidification.<sup>7</sup> The rotating jet-initiation induces the flow of the polymer solution through the orifice, and then, the jet-extension occurs toward to increase surface area of the propelled polymer stream. The solvent in the polymer stream evaporates, solidifying and contracting the jet. If the solvent is highly volatile, the jets form thicker fibers as the rapidly evaporating solvent potentiates rapid solidification, hindering the jet extension.

Among the various ways to prepare the polymeric nanofibers, electrospinning is the most popular and effective process, creating uniform nanofibers using electrostatic repulsion of a charged droplet of polymer liquid.<sup>8-10</sup> This process shares characteristics of both electrospraying and conventional solution-dry spinning of fibers.<sup>11</sup> The electrospinning is basically consisted of a syringe to hold the polymer solution, DC voltage supply in the kV range, and collector as shown in Figure 1.3A. When a sufficient voltage is supplied to a polymer droplet, located at the end of metal needle tip, the droplet becomes charged. In the charged droplet, electrostatic repulsion counteracts the surface tension and the droplet set about to stretch. At a critical point of the eruption of droplet from the surface, this point is known as the Taylor cone (Figure 1.3B). At this time, if the molecular cohesion of the droplet for polymer solution is

sufficiently high, the jet stream survives and starts flying to the collector. If the molecular cohesion is low, the droplets are electrosprayed. As the jet stream dries during the flight, the mode changes from ohmic flow to convective flow as the charge migrates to the surface of the fiber (Figure 1.3C). Then, in the region of convective flow, the jet is elongated by a whipping process induced by electrostatic repulsion. The elongation and thinning of the fiber resulting from the random bending brings about the formation of uniform nanofibers. Finally they are deposited on the collector.

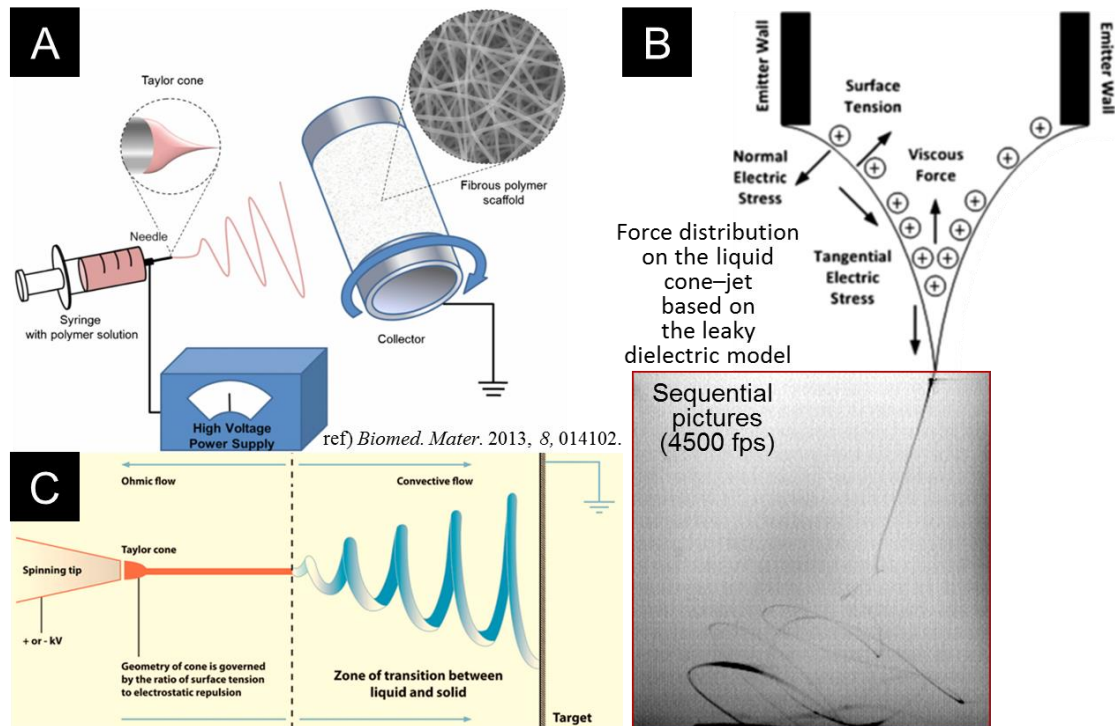


**Figure 1.3** Schematic of electrospinning process. (A) Apparatus of electrospinning, (B) How the formation of charge in the Taylor cone, and (C) Diagram showing flight of nanofiber during electrospinning.

## **1.2 Electrospinning Process**

The most electrospinning process have been carried out using polymer solution. There are three kinds of the parameters affecting the process: 1) polymer solution parameter, 2) processing condition parameter, and 3) ambient parameter. The nanofibers with the desired properties and characteristics can be developed with the understanding of these parameters as shown in Figure 1.4.

### **1.2.1. Polymer solution parameter (materials variables)**

The physical property of polymer solution, such as concentration, viscosity and surface tension, has a decisive effect on the process and the resultant product. The molecular weight and solution concentration significantly influences in the viscosity and surface tension of the solution. The surface tension plays an important role in the formation of defects, such as beads, along the nanofiber. The viscosity of the solution and its electrical properties determine the elongation extent of the solution, which have an effect on the diameter of nanofiber. One of the conditions necessary for electrospinning to occur where fibers are formed is that the solution must consists of polymer of sufficient molecular weight and the solution must be of sufficient viscosity.<sup>12</sup>

	<b>Materials variables</b>	
Chemical composition	Polymer MW	Polymer MWD
Solution viscosity (T)	Surface tension (T)	Solvent quality (T)
Solution concentration	Charge density	Solution conductivity
	<b>Processing variables</b>	
Electrode shape	Electrode materials	Electric field strength
Electrode-ground distance	Solution evaporation rate (T,P)	Solution flow rate

**Figure 1.4** Parameters affecting electrospinning process.



As the jet leaves the needle tip during electrospinning, the polymer solution is stretched and travels towards the collector. During the stretching of the polymer solution, it is the entanglement of the molecule chains that prevents the electrically driven jet from breaking up thus maintaining a continuous solution jet.

The molecular weight of the polymer indicates the length of the polymer chain, and it has an important effect on the viscosity of the solution. The polymer length can determine the amount of entanglement of the polymer chains in the solvent. Another way to increase the viscosity of the solution is the increase of the polymer concentration. Similar to increasing the molecular weight, an increasing of the concentration results in greater polymer chain entanglements within the solution, which is necessary to maintain the continuity of the jet during electrospinning.

The surface tension of polymer solution influences the electrospinnability. The initiation of electrospinning requires the charged solution to overcome its surface tension. But, as the jet travels towards the collector, the inappropriate surface tension can cause the formation of defects such as beads. Surface tension has the effect of decreasing the surface area per unit mass of a fluid. In the case of a high concentration of free solvent molecules, there is a greater tendency for the solvent molecules to congregate and adopt a spherical shape due to surface tension. A higher viscosity indicates the greater interaction

between the solvent and polymer molecules. Thus the solvent molecules tend to spread over the entangled polymer molecules and reduce the tendency for the solvent molecules to come together under the influence of surface tension. At high viscosity, the solvent molecules are distributed over the entangled polymer molecules, but in the case of a lower viscosity, the solvent molecules tend to congregate under the action of surface tension. Solvent such as ethanol has a low surface tension thus it can be added to encourage the formation of smooth fibers.<sup>13</sup> Another way to reduce the surface tension is to add surfactant to the solution. The nanofiber morphology was improved by The addition of surfactant in a polymer solution.<sup>14</sup>

The conductivity of a polymer solution also has an effect on the electrospinning. The stretching of the solution was induced by repulsion of the charges at its surface. As the conductivity of the solution is increased, more charges are carried to the jet. The conductivity of the solution can be increased by the addition of ionic salts. As mentioned, the defects such as beads should be form if the solution is not fully stretched due to the low conductivity of the solution. Therefore, when a small amount of salts is added to the solution, the the stretching of the solution can be occurred which may form smooth nanofibers. The increased in the stretching of the solution also tends to make nanofibers with smaller diameter. However, there are some cases about the increase of the nanofiber diameter. As the solution is being stretched, there

can be a greater viscoelastic force acting against the columbic forces of the charges. As a result, the thicker nanofibers were formed.<sup>15</sup> In addition, increased conductivity of the solution brings about decrease of the critical voltage for electrospinning. Another effect of the increased conductivity of the solution is that it results in a greater bending instability. As a result, the deposition area of the fibers is increased.

### **1.2.2. Processing parameter (processing variables)**

The parameters, including the supplied voltage, flow rate (feed rate) of polymer solution, distance between the needle tip and collector, diameter of needle and type of collector, are the external factors exerting on electrospinning jet and affect the electrospinning importantly. One of the curical parameters in electrospinning is the applied voltage to the solution. The high voltage will induce the necessary charges on the solution and together with the external electric field, will initiate the electrospinning process when the electrostatic force in the solution overcomes the surface tension of the solution. Generally, both high negative or positive voltage of more than 6 kV is able to cause the solution drop at the tip of the needle to distort into the shape of a Taylor Cone during jet initiation.<sup>16</sup> Depending on the flow rate of the solution, a higher voltage is required so that the Taylor Cone is stable. Then, the columbic repulsive force in the jet stretches the viscoelastic solution. When the applied

voltage is higher, the greater amount of charges causes the jet to accelerate faster and more volume of solution was drawn from the needle tip. When the drawing of the solution to the collection plate is faster than the supply from the source, the Taylor Cone hides into the needle.<sup>17</sup> As both the voltage supplied and the resultant electric field have an influence in the stretching and the acceleration of the jet, they have an influence on the morphology of the fibers obtained. In the most cases, a higher voltage leads to greater stretching of the solution due to the greater columbic forces in the jet as well as the stronger electric field. When a solution of lower viscosity is used, a higher voltage favors the formation of secondary jets during electrospinning. This has the effect of reducing the fiber diameter.<sup>18</sup>

The diameter of the nanofiber can be influenced by the flight time of the jet: a longer flight time will allow more time for the fibers to stretch and elongates before it is deposited on the collection plate. The reduced acceleration of the jet and the weaker electric field at a lower voltage increase the flight time of the jet which favors the formation of uniform nanofibers. The effect of high voltage is not only on the morphology of the nanofiber, it also affects the crystallinity of the nanofiber. The electrostatic field brings out the polymer molecules to be more ordered during electrospinning, thus induces a greater crystalline structure of the nanofiber. But it was reported that the crystallinity of the nanofiber was reduced above a certain voltage. With increased voltage,

the acceleration of the fibers also increases, and this reduces the flight time of the electrospinning jet. Since the orientation of the polymer molecules can take some time, the reduced flight time means that the nanofibers will be deposited before the polymer molecules have sufficient time to align itself. Thus, if sufficient flight time was given, the crystallinity of the nanofiber is improved with higher voltage.<sup>19</sup>

Generally, DC voltage is widely applied in electrospinning. Also, it is possible to use AC potential for electrospinning. In this case, the jet initiation, stretching and bending instability is caused due to the charges present in the solution. The charging of the solution is very rapid and jet initiation will occur before the voltage alternates in an AC supply. The regular segments of the jet can contain positive or negative charges on them alternately as the jets travel towards the collection plate. The columbic repulsive forces in the jet induces the bending instability during the flight. In other words, the regular segments in the jet of either positive or negative voltage would reduce the repulsive forces, so reducing the bending instability in the jet. The as-electrospun nanofibers can have a higher diameter than nanofibers that are formed by DC supply of the same voltage, because there is less bending instability and less stretching of the jet. Another advantage of an AC supply is that there is fewer tendencies for accumulation of like-charges on the fiber after it has been deposited. Thus, a thick nanofiber mat can be prepared when an insulating collection plate was

used.<sup>20,21</sup>

Among the the processing parameters, the flow rate (feed rate) is very important, because the flow rate determines the amount of solution during electrospinning. A stable Taylor cone can be formed and maintained only if the available flow rate was setted for a given voltage. When the flow rate increases, a much volume of solution is drawn away from the needle tip. This leads a corresponding increase of the diameter of nanofibers or defects size.<sup>22,23</sup> In the case of the fast flow rate, there must be a corresponding increase of voltage for supplying of sufficient charge to the jet. In addition the jet would take a longer time to dry, because of the greater volume of the solution drawn from the needle tip. The solvent in the jet can not have enough time to evaporate compared to the smaller volume of the solution pushing with slow flow rate, and it causes defects such as beads. Conclusionly, the slower flow rate was more desirable to prepare uniform nanofibers as the solvent will have more time to evaporate.<sup>24</sup>

The flight time of the jet affects the electrospinning process and the morphology of nanofibers. The flight time can be varied by control of the distance between the tip and the collector (tip to collector distance, TCD). TCD have a great influence in both the flight time and the electric field strength in electrospinning process. In the narrow TCD, the jet flies a short distance. It can be difficient time for the solvent to be evaporated. In ddition, the narrow TCD induces the

increase of electric field strength, and it allows the acceleration of the flying jet. So, too short TCD can cause the merged nanofibers that they contact each other to form junctions.<sup>25</sup> The increase of electric field strength by narrowing TCD also induces the instability of the jet, which can encourage defects formation.<sup>26</sup> If the electric field was at an optimal value, the electrostatic field would provide sufficient stretching to the jet, and so there was less defects formed.<sup>27</sup> If the TCD is too wide, no nanofibers were not able to deposit on the collector.<sup>28</sup> Therefore, an optimal electrostatic field strength must be provide via controll of the TCD to prepare the nanofibers effectively.

### **1.2.3. Example: electrospinning condition of polyamide 66**

It was reported that the optimal conditions for electrospinning of uniform polyamide 66 (PA66) nanofibers were determined by the control of various parameters, such as polymer solution concentration, flow rate, tip-to-collector distance (TCD), applied voltage, and electrical conductivity of the polymer solution.<sup>29</sup> An organic salt, benzyl trimethyl ammonium chloride ( $C_{10}H_{16}ClN$ , BTMAC), was added to the solutions for increase of electrical conductivity. When no salt was added to the PA66 solution, the uniform nanofibers were electrospun only at limited conditions, such as flow rate of 0.5 mL/h and electric fields greater than 2.0–3.5 kV/cm as shown in Figure 1.5A-C. In contrast, by the addition of BTMAC, range of

optimal conditions for uniform nanofibers was expanded; uniform nanofibers were obtained at flow rate of 0.5–1.5 mL/h and electric fields greater than 1.3–1.6 kV/cm as in Figure 1.5D-F. The expansion of optimal electrospinning conditions by improving conductivity, it means enhancement of electrospinnability and contribute to productivity improvement of uniform nanofibers. Furthermore, the addition of BTMAC affected the increasing of number average diameters and standard deviation of the nanofibers as shown in Figure 1.6. When the salt was not added, the nanofibers had an average diameter of  $92.75 \pm 15.91$  to  $162.21 \pm 19.40$  nm. In contrast, the nanofibers with increased electrical conductivity showed an average diameter of  $128.85 \pm 21.34$  to  $353.65 \pm 62.22$  nm. Also, addition of BTMAC influenced on the increase of diameter distribution. On the other hand, the process variables, such as flow rate, TCD, and voltage, exerted little influence on the diameter in this case.



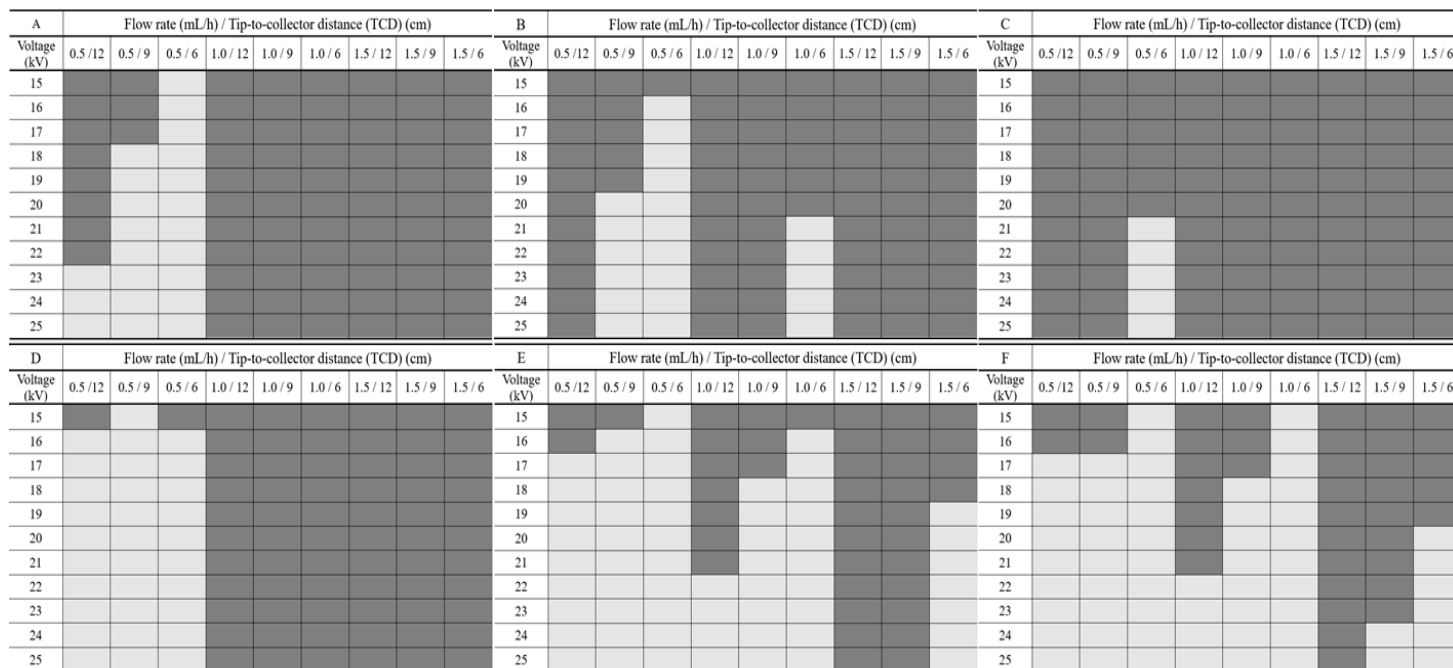


**Figure 1.5** Optimal electrospinning conditions for (A) 10 wt%, (B) 15 wt% and (C) 20 wt% PA66 solution without the salt and (D) 10 wt%, (E) 15 wt% and (F) 20 wt% PA66 solution with the BTMAC salt. Bright space means the good spinnable zone.

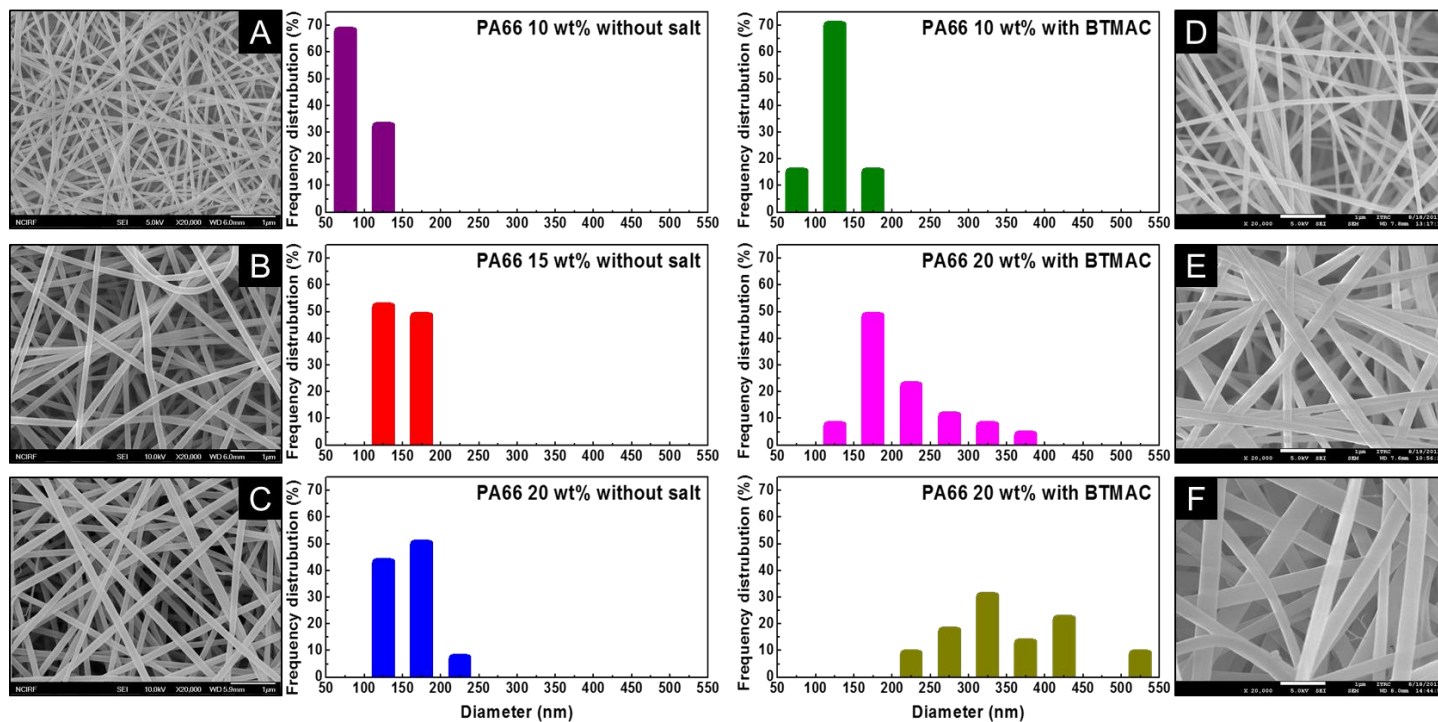


**Figure 1.6** Morphologies of electrospun PA66 nanofibers (A) without salt at 10 wt%, 0.5 mL/h, 9 cm and 25 kV, (B) without salt at 15 wt%, 0.5 mL/h, 9 cm and 25 kV, (C) without salt at 20 wt%, 0.5 mL/h, 6 cm and 25 kV, (D) with BTMAC at 10 wt%, 0.5 mL/h, 12 cm and 25 kV, (E) with BTMAC at 15 wt%, 1.5 mL/h, 6 cm and 19 kV, and (F) with BTMAC at 20 wt%, 0.5 mL/h, 9 cm and 20 kV. Scale bar means 1  $\mu$ m.

## **1.3 Application of Electrospun Nanofibers**

Electrospun nanofibers have been attracting the attention of highly functional materials due to their enhanced properties, such as high surface to volume ratio, very high porosity and enhanced physico-mechanical properties. Manipulation of the solution and process parameters can be easily controlled to get the desired morphology and mechanical properties, required for application in specific areas like biomedical applications, filtration, sensors, defensive materials, energy generation, reinforcement material, and cosmetics. In addition, reviewing the number of patents, approximately two-thirds of all electrospinning applications are in the medical field. Of the remaining patents, one-half deals with filtration applications, and all other applications share the remaining half.<sup>30</sup> Various research and developments are going in the fields of electrospinning owing to application of these nanofibers in diverse fields. A brief schematic of the applications with nanofibers and related nanomaterials is shown in Figure 1.7. In future electrospun nanofibers will prove to be a promising candidate for a wider range of applications.

### **1.3.1. Tissue scaffolds**

For engineering living tissues, biodegradable scaffold is generally considered as an indispensable element as these are used as temporary templates for cell seeding, proliferation, invasion, and differentiation prior to the regeneration of

natural extracellular matrix (ECM) or biologically functional tissue. There has been an increased surge in the use of electrospinning techniques to create nanofibrous tissue scaffolds as there are reports that these scaffolds positively promote cell–matrix and cell–cell interactions with the cells having gene expression and a normal phenotypic shape.<sup>31,32</sup> Natural polymers are often used for preparing nanofibrous scaffolds due to their enhanced biocompatibility and bio-functional motifs such as alginate, starch, collagen, silk protein, hyaluronic acid, fibrinogen, chitosan and others. In addition, blending of natural polymers into synthetic polymers can improve the overall cytocompatibility of the scaffold.<sup>33</sup> A variety of polymeric nanofibers have been considered for use as scaffolds for engineering tissues such as cartilages,<sup>34</sup> dermal tissue engineering,<sup>35</sup> and bones.<sup>36</sup> Electrospun poly(lactic-co-glycolic acid) (PLGA) nanofibers are considered for tissue engineering scaffolds because their porosity is greater than 90%, the high surface area allows higher cellular attachment. Also due to nano-sized fiber diameters, there are multiple focal adhesion points on different fibers. This electrospun nanofibers supports growth and proliferation of a wide variety of cell types for example, mouse fibroblasts adhere and spreadwell on PLGA nanofibers according to fiber orientation.<sup>37</sup> Silk fibroin fiber scaffolds containing bone morphogenetic factor 2 (BMP-2) and/or nanoparticles of hydroxypetite (nHAP) via electrospinning have been used for in vitro bone formation from human bone



**Figure 1.7** Applications of electrospun nanofibers in various fields.

marrowderived mesenchymal stem cells (hMSCs) and suggest that silk fibroin nanofibrous scaffolds serve as ideal candidates for bone tissue engineering.<sup>38</sup>

### **1.3.2. Filtration**

Nanofibers have been used in air and water filtration applications for more than a decade. For filtration, the channels and structural elements of a filter must be matched to the scale of the particles or droplets that are to be captured in/on the filter. It has been realized that electrospinning is rising to the challenge of providing solutions for the removal of unfriendly particles in such submicron ranges. Generally, tiny particles of the order of  $< 0.5 \mu\text{m}$  can be easily trapped in the electrospun nanofibrous filters due to the very high surface area to volume ratio and the resulting high surface cohesion, and this improves the filtration efficiency. The nanofiber membrane shows an extremely effective removal ( $> 99\%$  rejection) of airborne particles with diameters between  $1 \mu\text{m}$  and  $5 \mu\text{m}$  by the electrokinetic capture in the air filter as well as by the physical entrapment mechanism.<sup>39</sup> Also, by integrating the spinning and charging of polymer into nanofibers in one step, nanofibers can be electrostatically charged to modify the ability of electrostatic attraction of particles without increase in pressure drop to further improve filtration efficiency.<sup>40</sup> Filtration efficiency, which is closely associated with fiber fineness, is one of the most important concerns for filter performance. The enhanced filtration efficiency at the

same pressure drop is possible with fibers having diameters less than 0.5  $\mu\text{m}$ .<sup>41</sup> Researchers have evaluated the filtration efficiency of nylon 6 nanofibers with 80–200 nm in diameter and pressure drop across the filter and found that 99.99% superior filtration efficiency of nylon 6 nanofibers than commercialized high efficiency particulate air (HEPA) filter using 0.3  $\mu\text{m}$  test particles at the face velocity of 5 cm/s.<sup>42</sup> Few research groups have successfully synthesized electrospun polyurethane cationomers (PUCs) containing different amounts of quaternary ammonium groups into non-woven nanofiber membranes for use in antimicrobial nanofilter applications and showed very strong antimicrobial activities against *Staphylococcus aureus* and *Escherichia coli*.<sup>43</sup> Also, there are numerous studies of applying adsorptive membranes/felts for the purification of large biomolecules such as proteins.<sup>44</sup>

### **1.3.3. Protective clothing materials**

Current protective clothing is based on permeable adsorptive protective overgarments and full barrier protection such as hazardous materials (HAZMAT) suits such as those used by the US military. The protective clothing should have some essential properties such as, breathable nature, light weight, air and moisture permeability, insolubility in all solvents and enhanced toxic chemical resistance. Electrospun nanofibers have been recognized as potential candidates for protective clothing applications, because of their large

surface area, high porosity, great filtration efficiency, light weight, resistant to penetration of harmful chemical agents in aerosol form and their ability to neutralize the chemical agents without impedance of the air and moisture permeability to the clothing materials.<sup>45</sup> A variety of methods for modification of nanofiber surfaces have been tried to get improved protection against toxins. Protection methods, which have been used, includes chemical surface modification and attachment of reactive groups such as oximes, cyclodextrins, and chloramines that bind and detoxify warfare agents.<sup>39</sup>

#### **1.3.4. Energy generation**

Conductive nanofibrous membranes have potential for applications such as, photovoltaic device, electrostatic dissipation, corrosion protection, electromagnetic interference shielding, fabrication of tiny electronic devices or machines such as Schottky junctions, sensors and actuators, as the rate of electrochemical reactions is proportional to the surface area of the electrode.<sup>46</sup> In addition, conductive nanofibrous membranes are quite suitable for use as porous electrodes in developing high performance batteries and polymer electrolyte membrane fuel cells (PEMFCs) due to its high porosity and inherent large total surface area. Also, polymer batteries have been developed for cellular phones to replace conventional, bulky lithium batteries. The components of polymer batteries are a carbon anode, a lithium cobalt oxide



cathode, and a polymer gel electrolyte. Conductive nanofibers offers noteworthy properties of polymer batteries, for example, less electrolyte leakage, high dimension flexibility, and high energy density per weight.<sup>47</sup> However, there is still a need to improve energy density per weight of polymer batteries to increase their market share.

### **1.3.5. Reinforcement material**

Carbon nanofiber (CNF) has superior mechanical properties, and so, their mechanical properties enable them to be used as fillers in composites. Carbon nanofiber reinforced composites offer enhanced stiffness, high strength and low electrical resistivity. In addition, aligned nanofiber composites provide enhanced mechanical properties than the composites containing non-aligned nanofibers. Ma *et al.* reported the morphology and mechanical properties of polyethylene terphthalate (PET) resins compounded with CNF.<sup>48</sup> The compressive and torsional properties of the composites increased up to 50% compared to the normal PET, while its tensile modulus showed only moderate improvement.<sup>48</sup>

### **1.3.6. Cosmetics**

Electrospun nanofibers have been utilized with various additives as a cosmetic skin caremask for skin cleansing, skin healing, therapeutical and medical treatments.<sup>49</sup> The nanofibrous skin mask has advantage of high surface area to volume ratio which facilitates better utilization and also speeds up the transfer rate of the additives to the skin. In addition, the nanofibrous cosmetic skin mask can be introduced gently and painlessly and also directly to the three-dimensional topography of the skin to provide healing or care treatment to the skin.<sup>50</sup> Skin-revitalizing factors can be impregnated into nanofiber masks for skin health and renewal.<sup>39</sup>

## **1.4. Summary**

Electrospinning is a simple, versatile, and cost-effective technology which generates non-woven nanofibers with high surface area to volume ratio, porosity and tunable porosity. Because of these properties, nanofibers seem to be a promising candidate for various applications. Solution and processing parameters such as viscosity, molecular weight, concentration of the polymer, applied voltage, tip to collector distance, and conductivity. Significantly affect the nanofiber morphology and by manipulation of these parameters one can get desired properties for specific application. Electrospun nanofibers are increasingly being used in a variety of applications such as, tissue engineering scaffolds, wound healing, drug delivery, sensors, protective clothing, cosmetics, and filtration applications. Despite of several advantages and success of electrospinning there are some critical limitations in this process such as small pore size and lack of proper cellular infiltration inside the fibers. Several attempts in these directions are being made to improve the design and cellular migration through multilayering, inclusion of heprasil and blending with polymers with different degradation behavior.

## 1.5. Research Objectives

With this background and the technological and scientific value of nanofibers as motivations, the preparation of functional nanofibrous materials with specific characteristics is both desirable and technologically important. In this study, the polymeric nanofiber composites were developed using simultaneous electrospinning and electrospraying process, then applied to protective materials.

In chapter 2, two types of electrospun Nylon 66 nanofiber composites in which Ag-TiO<sub>2</sub> was located either in the interior or on the surface of the nanofiber using electrospinning and simultaneous electrospinning/electrospray (SEE) process, respectively. The performance of the obtained Ag-TiO<sub>2</sub>-embedded nanofiber composite (interior located Ag-TiO<sub>2</sub>: AT-*in*-NF) and Ag-TiO<sub>2</sub>-decorated nanofiber composite (surface located Ag-TiO<sub>2</sub>: AT-*sur*-NF) was compared by evaluating the decolorization of methylene blue (MB) stain and their antimicrobial ability. It was concluded that the positioning of nanomaterial additives is a crucial factor in the enhanced performance of such nanofiber composites, and provide a guide for designing and optimizing nanofiber composites with superior catalytic activities.

In chapter 3, a potential application of nanofibrous composite materials impregnated the MgO and POM adsorbents was exhibited as an inner layer for the permeable protective clothing against CWA. The nanofiber

composites, which were consisted of both polyamide 66 nanofiber and adsorbents (MgO and POM), were prepared using the SEE process. The nanofiber composites were compared to neat polyamide 66 nanofiber mat by evaluating the permeability of air, moisture and gas chemical warfare simulants. It was suggested that the high possibility of the application of the nanofiber composites to the inner layer of permeable protective clothing.

In chapter 4, it was reported that electrospun *meta*-aramid nanofibers with enhanced chemical stability and mechanical property using sequential post-treatment for removal of salt in the nanofiber and regeneration of crystalline structure. The aligned *meta*-aramid nanofibers with LiCl salt was prepared using electrospinning apparatus with drum-collector. The washing and heating sequential post-treated nanofiber mats showed improved chemicals stability. Furthermore, in order to estimate the possibility of their application to an outer layer for permeable protective clothing having the repellency against liquid chemical warfare simulants, the surface of *meta*-aramid nanofibers was modified via treatment using water and oil repellent. In chapter 5, lightweight nanofibrous assemblies with high protection ability against chemical warfare agents (CWAs) were developed using laminated outer and inner layers based on aromatic and aliphatic polyamide nanofiber composites with CWA adsorbents magnesium oxide and polyoxometalate. Thickness, weight density (weight per area), cool/warm feeling and

air/moisture permeability of the assembly were compared with the permeable protective clothing of Korea Army as a reference. The thickness and weight density were varied according to the number of stacking, and finally, the lightweight assemblies with high protectability against CWA can be developed. The assembly surpassed the reference in the cool feeling property, and provided good resistance to the penetration of chemical warfare agents in gas form, while still allowing significant water vapor transmission to promote evaporate cooling of the body. The development of the assembly suggests new approach to improving performance of a permeable protective materials, and provides a guide for designing and optimizing the permeable protective clothing.

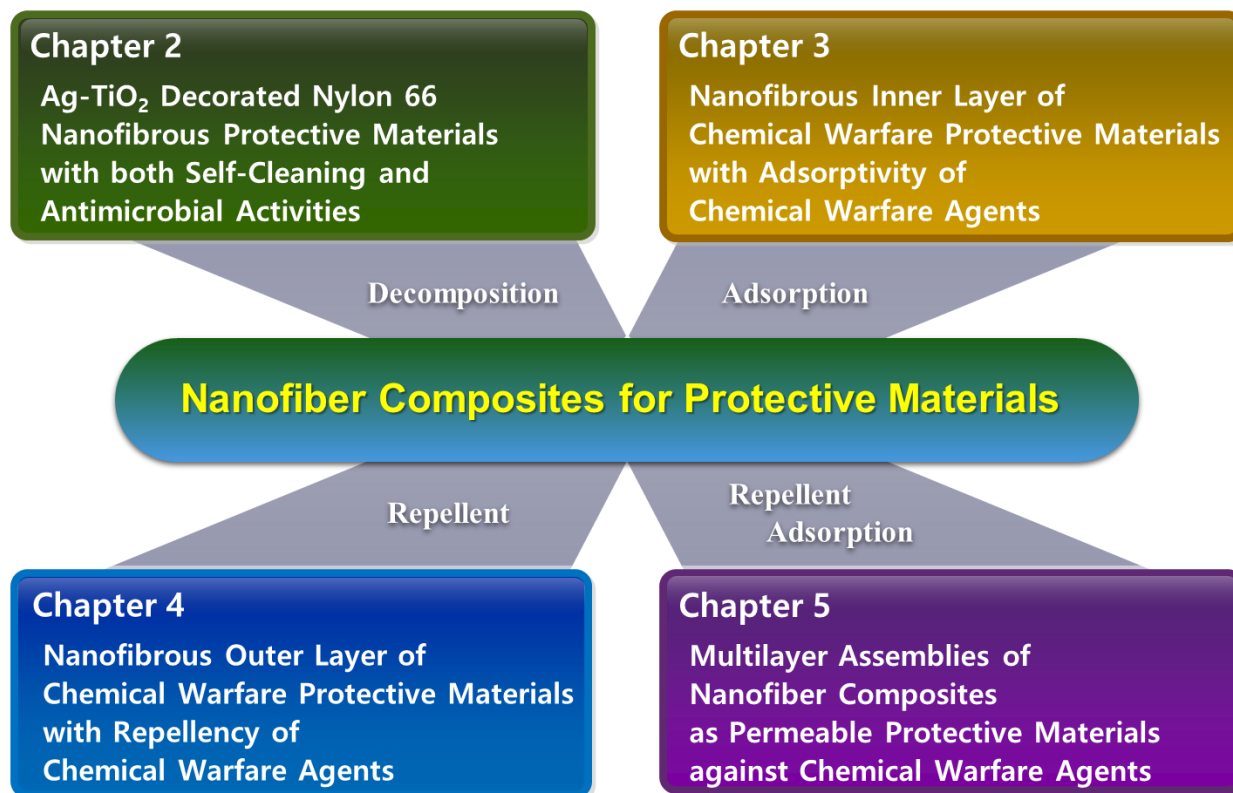


**Figure 1.8** Research Objectives: Development of nanofibrous protective materials.

## References

1. Zhou, F.-L.; Gong, R.-H. *Polymer International* **2008**, *57*, 837.
2. Xing, X.; Wang, Y.; Li, B. *Opt. Express* **2008**, *16*, 10815.
3. Tao, S. L.; Desai, T. A. *Nano Lett.* **2007**, *7*, 1463.
4. Zhang, S. *Nat. Biotechnol.* **2003**, *21*, 1171.
5. Ma, P. X.; Zhang, R. *J. Biomed. Mater. Res.* **1999**, *46*, 60.
6. Hassan, M. A.; Yeom, B. Y.; Wilkie, A.; Pourdeyhimi, B.; Khan, S. A. *J. Membr. Sci.* **2013**, *427*, 336.
7. Badrossamay, M. R.; McIlwee, H. A.; Goss, J. A.; Parker, K. K. *Nano lett.* **2010**, *10*, 2257.
8. Dzenis, Y. *Science* **2004**, *304*, 1917.
9. Li, D.; Xia Y. *Adv. Mater.* **2004**, *16*, 1151.
10. Teo, W. E.; Ramakrishna, S. *Nanotechnology* **2006**, *17*, 89.
11. *Fundamentals of fiber formation*; Ziabicki, A.; John Wiley and Sons: London, 1976.
12. Bhardwaj, N.; Kundu, S. C. *Biotechnol. Adv.* **2010**, *28*, 325.
13. Fong, H.; Chun, I.; Reneker, D. H. *Polymer* **1999**, *40*, 4585.
14. Zeng, J.; Xu, X.; Chen, X.; Liang, Q.; Bian, X.; Yang, L.; Jing, X. *J. Control. Release* **2003**, *92*, 227.
15. Mit-uppatham, C.; Nithitanakul, M.; Supaphol, P. *Macromol. Chem. Phys.* **2004**, *205*, 2327.
16. Taylor, G. *Proc. Roy. Soc.* **1964**, *A280*, 383.
17. Deizel, J. M.; Kleinmeyer, J.; Harris, D.; Beck Tan, N.C. *Polymer* **2001**, *42*, 261.
18. Demir, M.M.; Yilgor, I.; Yilgor, E. E. A.; Erman, B. *Polymer* **2002**, *43*, 3303.
19. Ero-Phillips, O.; Jenkins, M.; Stamboulis, A. *Polymer* **2012**, *4*, 1331.



20. He, J.-H.; Wu, Y.; Pan, N. *Int. J. Nonlinear Sci. Numer. Simul.* **2005**, *6*, 243.
21. Kessick, R.; Tepper, G. *Sens. Actuator B-Chem.* **2006**, *117*, 205.
22. Hohman, M. M.; Shin, M.; Rutledge, G.; Brenner, M. P. *Phys. Fluids* **2001**, *13*, 2201.
23. Hohman, M. M.; Shin, M.; Rutledge, G.; Brenner, M. P. *Phys. Fluids* **2001**, *13*, 2221.
24. Yuan, X. Y.; Zhang, Y. Y.; Dong, C. H.; Sheng, J. *Polym. Int.* **2004**, *53*, 1704.
25. Buchko, C. J.; Chen, L. C.; Shen, Y.; Martin, D. C. *Polymer* **1999**, *40*, 7397.
26. Deitzel, J. M.; Kleinmeyer, J.; Harris, D.; Tan, N. C. B. *Polymer* **2001**, *42*, 261.
27. Jarusuwannapoom, T.; Hongroijanawiwat, W.; Jitjaicham, S.; Wannatong, L.; Nithitanakul, M.; Pattamaprom, C.; Koombhongse, P.; Rangkupan, R.; Supaphol, P. *Eur. Polym. J.* **2005**, *41*, 409.
28. Zhao, S. L.; Wu, X. H.; Wang, L. G.; Huang, Y. *J. Appl. Polym. Sci.* **2004**, *91*, 242.
29. Ryu, S.-Y.; Kwak, S.-Y. *J. Nanosci. Nanotechnol.* **2013**, *13*, 4193.
30. Burger, C.; Hsiao, B. S.; Chu, B. *Annu. Rev. Mater. Res.* **2006**, *36*, 333.
31. Li, W. J.; Laurencin, C. T.; Caterson, E. J.; Tuan, R. S.; Ko, F. K. *J. Biomed. Mater. Res.* **2002**, *60*, 613.
32. He, W.; Horn, S. W.; Hussain, M. D. *Int. J. Pharm.* **2007**, *334*, 173.
33. Wayne, J. S.; McDowell, C. L.; Shields, K. J.; Tuan, R. S. *Tissue Eng.* **2005**, *11*, 953.
34. Rho, K. S.; Jeong, L.; Lee, G.; Seo, B. M.; Park, Y. J.; Hong, S. D. *Biomaterials* **2006**, *27*, 1452.
35. Venugopal, J.; Ramakrishna, S. *Tissue Eng.* **2005**, *11*, 847.
36. Chen, J. L.; Chu, B.; Hsiao, B. S. *J. Biomed. Mater. Res.* **2006**, *79A*, 307.

37. Geng, X.; Kwon, O. H.; Jang, J. *Biomaterials* **2005**, *26*, 5427.
38. Li, C.; Vepari, C.; Jin, H. J.; Kim, H. J.; Kaplan, D. L. *Biomaterials* **2006**, *27*, 3115.
39. Ramakrishna, S.; Fujihara, K.; Teo, W. E.; Yong, T.; Ma, Z.; Ramaseshan, R. *Mater. Today* **2006**, *9*, 40.
40. Tsaia, P. P.; Schreuder-Gibson, H.; Gibson, P. J. *Electrost.* **2002**, *54*, 333.
41. Subbiah, T.; Bhat, G. S.; Tock, R. W.; Parameswaran, S.; Ramkumar, S. S. *J. Appl. Polym. Sci.* **2005**, *96*, 557.
42. Ahn, Y. C.; Park, S. K.; Kim, G. T.; Hwang, Y. J.; Lee, C. G.; Shin, H. S. *Curr. Appl. Phys.* **2006**, *6*, 1030.
43. Jeong, E. H.; Yang, J. Youk, J. H. *Mater. Lett.* **2007**, *61*, 3991.
44. Zhang, L.; Menkhaus, T. J.; Fong, H. J. *Membr. Sci.* **2008**, *319*, 176.
45. Schreuder-Gibson, H. L.; Gibson, P.; Senecal, K.; Sennett, M.; Walker, J.; Yeomans, W. J. *Adv. Mater.* **2002**, *34*, 44.
46. Senecal, K. J.; Ziegler, D. P.; He, J.; Mosurkal, R.; Schreuder-Gibson, H.; Samuelson, L. A. *Mater. Res. Soc. Symp. Proc.* **2002**, *708*, 285.
47. Choi, S. W.; Jo, S. M.; Lee, W. S.; Kim, Y. R. *Adv. Mater.* **2003**, *15*, 2027.
48. Ma, H.; Zeng, J.; Realff, M. L.; Kumar, S.; Schiraldi, D. A. *Compos. Sci. Technol.* **2003**, *63*, 1617.
49. Smith, D.; Reneker, D.; McManus, A.; Schreuder-Gibson, H.; Mello, C.; Sennet, M. *PCT International Application No:PCT/US00/27776*, **2001**.
50. Huang, Z. M.; Zhang, Y. Z.; Kotaki, M.; Ramakrishna, S. *Compos. Sci. Technol.* **2003**, *63*, 2223.

## **Chapter 2**

# **Ag-TiO<sub>2</sub> Decorated Nylon 66 Nanofibrous Protective Materials with both Self-Cleaning and Antimicrobial Activities**

### **2.1 Introduction**

Great attention has been devoted to nanofibers over the past few decades owing to their unique features, such as a submicron diameter, light weight, controllable pore structure, and high surface area-to-volume ratio.<sup>1-3</sup> Thus the nanofibers have been widely studied in fields of filtration,<sup>4</sup> tissue engineering,<sup>5</sup> sensors,<sup>6</sup> electronic and photonic materials,<sup>7</sup> drug delivery,<sup>8</sup> and protective materials.<sup>9</sup> Among the numerous methods currently available to produce nanofibers, the ever-increasing utility of electrospinning as an enabling method for the successful realization of novel nanofibers continues to motivate the development of novel nanotechnology. In particular, the compositing of nanofibers with functional nanomaterials such as carbon materials,<sup>10,11</sup> noble metals,<sup>12</sup> or photocatalytic semiconductors<sup>13</sup> has been intensively studied as a method to further develop and enhance the functionality of electrospun polymeric nanofibers. Titanium dioxide (TiO<sub>2</sub>) is a representative semiconductor with outstanding electrical, optical, and photocatalytic

behaviors owing to its powerful photo-induced oxidation and reduction characteristics.<sup>14,15</sup> These properties make TiO<sub>2</sub> useful in environmental remediation processes such as water and air purification, the prevention of stains, and sterilization.<sup>16</sup> In particular, TiO<sub>2</sub> has attracted considerable attention in the field of solar cells for its superior photo-induced charge-carrier generation, band gap excitation, and charge equilibrium in the Fermi level.<sup>17</sup> However, the practical use of TiO<sub>2</sub> is extremely limited because its photocatalytic activity is very poor under natural light, *i.e.*, visible light, owing to its wide band gap (3.2 eV for anatase phase). Thus, varied approaches aimed at enhancing the visible light photocatalytic activity of TiO<sub>2</sub> have been intensively studied.<sup>18–20</sup> Among them, loading of Ag metal onto the TiO<sub>2</sub> surface (Ag-TiO<sub>2</sub>) has been reported as an effective approach capable of extending the light absorption of TiO<sub>2</sub> into the visible range and enhancing surface electron excitation through plasmon resonance.<sup>21,22</sup> Moreover, Ag-TiO<sub>2</sub> has powerful antibacterial properties.<sup>23</sup> Thus, hybridization of Ag-TiO<sub>2</sub> with electrospun nanofibers (Ag-TiO<sub>2</sub>/polymer nanofiber composite) is anticipated to provide considerably enhanced functionality through the synergistic combination of the unique optical, electrical, photocatalytic and antimicrobial properties of Ag-TiO<sub>2</sub> and the excellent specific surface area of the nanofibers.<sup>24–26</sup>

Herein, two types of electrospun Nylon 66 nanofiber composites containing

Ag-TiO<sub>2</sub> were prepared using electrospinning and simultaneous electrospinning/electrospraying (SEE) process. Ag-TiO<sub>2</sub> was located either in the interior or on the surface of the nanofiber matrix, respectively. The performance of the obtained Ag-TiO<sub>2</sub>-embedded nanofiber composite (interior located Ag-TiO<sub>2</sub>: AT-*in*-NF) and Ag-TiO<sub>2</sub>-decorated nanofiber composite (surface located Ag-TiO<sub>2</sub>: AT-*sur*-NF) was compared by evaluating the decolorization of methylene blue (MB) stain and their antimicrobial ability. AT-*sur*-NF, in which Ag-TiO<sub>2</sub> was exposed on the nanofiber surface, was found to have better photocatalytic and antimicrobial activities than AT-*in*-NF, in which Ag-TiO<sub>2</sub> was hidden inside these nanofibers. These findings suggest that the positioning of nanomaterial additives is a crucial factor in the enhanced performance of such nanofiber composites, and provide a guide for designing and optimizing nanofiber composites with superior catalytic activities.

## 2.2 Experiments

### 2.2.1 Preparation and characterization of Ag-TiO<sub>2</sub>

Silver-loaded titanium dioxide (Ag-TiO<sub>2</sub>) was prepared by loading Ag clusters onto the surface of TiO<sub>2</sub>. First, commercial TiO<sub>2</sub> nanoparticles, P25, containing 70% anatase and 30% rutile crystalline phases,<sup>27</sup> were irradiated with ultraviolet (UV) light ( $\lambda = 253.7$  nm, 15 W germicidal lamp, model G15T8; Sankyo Denki, Japan) for 1 h to induce surface hydrophilicity. 0.4 g (5.0 mmol) of the UV-treated TiO<sub>2</sub> was dispersed in 200 mL deionized water in a quartz bottle and adjusted to a pH value of 8.0–8.2 using aqueous ammonium hydroxide (NH<sub>4</sub>OH) solution, followed by ultrasonication for 1 h. Then, 2, 5, 10, or 15  $\mu$ mol of silver nitrate (AgNO<sub>3</sub>, ACS reagent,  $\geq 99.0\%$ ; Sigma Aldrich) was individually dissolved in the aqueous TiO<sub>2</sub> dispersion and stirred for 1 h in a cooling bath below 10 °C to achieve equilibrium adsorption. The dispersions were then irradiated with UV light ( $\lambda = 253.7$  nm) for 6 h at room temperature to photoreduce Ag clusters onto the surface of the TiO<sub>2</sub>. The resulting Ag-TiO<sub>2</sub> was centrifuged, washed with deionized water, and dried at room temperature for 24 h in a vacuum oven.

The presence of Ag on the surface of Ag-TiO<sub>2</sub> was confirmed by high resolution transmission electron microscopy (HR-TEM; JEM-3010; JEOL), field emission scanning electron microscopy (FE-SEM; SUPRA 55VP; Carl Zeiss),

energy-dispersive X-ray spectroscopy (EDS; XFlash 4000; Bruker AXS), and X-ray photoelectron spectroscopy with Mg/Al  $K_{\alpha}$  X-ray source and sweep mode analyzer electronics (XPS; SIGMA PROBE; ThermoVG). The Ag content of the Ag-TiO<sub>2</sub> was evaluated by XPS. To evaluate the photocatalytic activity of the Ag-TiO<sub>2</sub>, 100 mg of the Ag-TiO<sub>2</sub> was well dispersed in 100 mL aqueous solution containing 20 ppm of methylene blue (MB) and irradiated with visible light ( $\lambda = 380\text{--}480$  nm,  $\lambda_{\text{max}} = 420$  nm, 15 W Philips TL-D 15W/03 ISL fluorescent lamp) for 24 h at  $26 \pm 1$  °C. At regular intervals, 2 mL of the irradiated dispersion was collected and filtered using a hydrophilic syringe filter (HP020AN; Advantec). The change in the relative concentration of MB in the solution was determined by UV-visible spectroscopy. The antimicrobial activity of the Ag-TiO<sub>2</sub> was evaluated against *Staphylococcus aureus* (ATCC 6538, Gram-positive bacteria) and *Escherichia coli* (ATCC 25922, Gram-negative bacteria) using the shake flask method according to ASTM E 2149:2010 by the FITI Testing & Research Institute, Korea.

### **2.2.2 Preparation and characterization of Ag-TiO<sub>2</sub>-embedded and decorated nanofiber composites**

Ag-TiO<sub>2</sub>-embedded nanofiber composite (AT-*in*-NF) was fabricated by electrospinning as shown in Figure 2.1A and 1B. Briefly, 0.054 g Ag-TiO<sub>2</sub> was dispersed in 36 mL of formic acid ( $\geq 95\%$ ; Sigma-Aldrich) with 0.054 g of

benzyl trimethyl ammonium chloride ( $C_{10}H_{16}ClN$ , BTMAC, 98.0%; Tokyo Chemical Industry) as a salt and ultrasonicated with a bath-type ultrasonicator. Then, 5.4 g of Nylon 66 (poly(hexamethylene adipamide)) pellets (Sigma-Aldrich) were added to the Ag-TiO<sub>2</sub> dispersion and mildly shaken for 24 h at room temperature. The resulting solution was electrospun using the following conditions: 0.33-mm inner-diameter stainless steel spinneret, 18–20 kV at the spinneret, 9 cm tip-to-collector distance, −7 kV at the collector, collector rotation speed of 100 rpm, and solution flow rate of 0.5 mL/h for 1 day at  $22 \pm 1$  °C and  $50 \pm 5$  % relative humidity. The as-electrospun sample was soaked and washed with deionized water to completely remove the salt from the nanofibers.

Ag-TiO<sub>2</sub>-decorated nanofiber composite (AT-*sur*-NF) was fabricated by simultaneous electrospinning/electrospraying (SEE) process as shown in Figure 2.1C and 1D. This process was carried out using an electrospinning/electrospray apparatus (NanoNC, Korea) composed of a rotating drum collector, two positive DC voltage supplies, one negative DC voltage supply, and two syringe pumps comprising housings with syringe retainers. These syringe pumps were placed on opposite sides with respect to the collector. For the electrospinning, 5.4 g of Nylon 66 pellets were dissolved in 36 mL formic acid with 0.054 g of BTMAC as a salt and mildly shaken for 24 h at room temperature until the solution was transparent. The



electrospinning conditions were the same as those detailed above for AT-*in*-NF. For the electrospraying, 1 g of Ag-TiO<sub>2</sub> was dispersed in 100 mL methanol using a horn-type ultrasonicator at 250 W for 30 min. The Ag-TiO<sub>2</sub> dispersion was then electrosprayed using the following conditions: 0.51-mm inner diameter stainless steel spinneret, 12 kV at spinneret, 10 cm tip-to-collector distance, and solution flow rate of 2.5 mL/h for 1 day. The as-prepared sample was heat pressed at 100 °C and 1,000 psi for 2 min using a manual hydraulic press (Carver 3925; Carver Inc.) to adhere the Ag-TiO<sub>2</sub> on the surface of the nanofibers, and then thoroughly washed four times with deionized water/methanol solution to remove the salt and any unbound Ag-TiO<sub>2</sub> from the nanofibers. All washed samples were dried at room temperature for 1 day in air and a vacuum oven, and stored in a vacuum desiccator.

The morphologies of AT-*in*-NF and AT-*sur*-NF were evaluated by FE-SEM (JSM-6335F; JEOL and SUPRA 55VP; Carl Zeiss). The content of Ag-TiO<sub>2</sub> in the nanofiber composites was determined by thermogravimetric analysis (TGA; Q5000 IR, TA Instruments; ramp rate 10 °C/min, 40–600 °C, N<sub>2</sub> atmosphere). The photo-induced self-cleaning behaviors of the nanofiber composites (4×4 cm<sup>2</sup>) were investigated by evaluating their decolorization of a MB stain under visible light irradiation ( $\lambda = 380\text{--}480\text{ nm}$ ,  $\lambda_{\text{max}} = 420\text{ nm}$ ) for 12 h at  $26 \pm 1\text{ }^{\circ}\text{C}$ . Images of the irradiated samples were obtained using a flatbed scanner (CanoScan LiDE 700F), and the color strength of the remaining

MB on the samples were determined using a spectrophotometer (X-rite 8000 Series) interfaced with a personal computer. The antimicrobial activity of the nanofiber composites was quantified against *S. aureus* (ATCC 6538, Gram-positive bacteria) and *Klebsiella pneumoniae* (ATCC 4352, Gram-negative bacteria) according to AATCC 100:2012 by the FITI Testing & Research Institute, Korea.

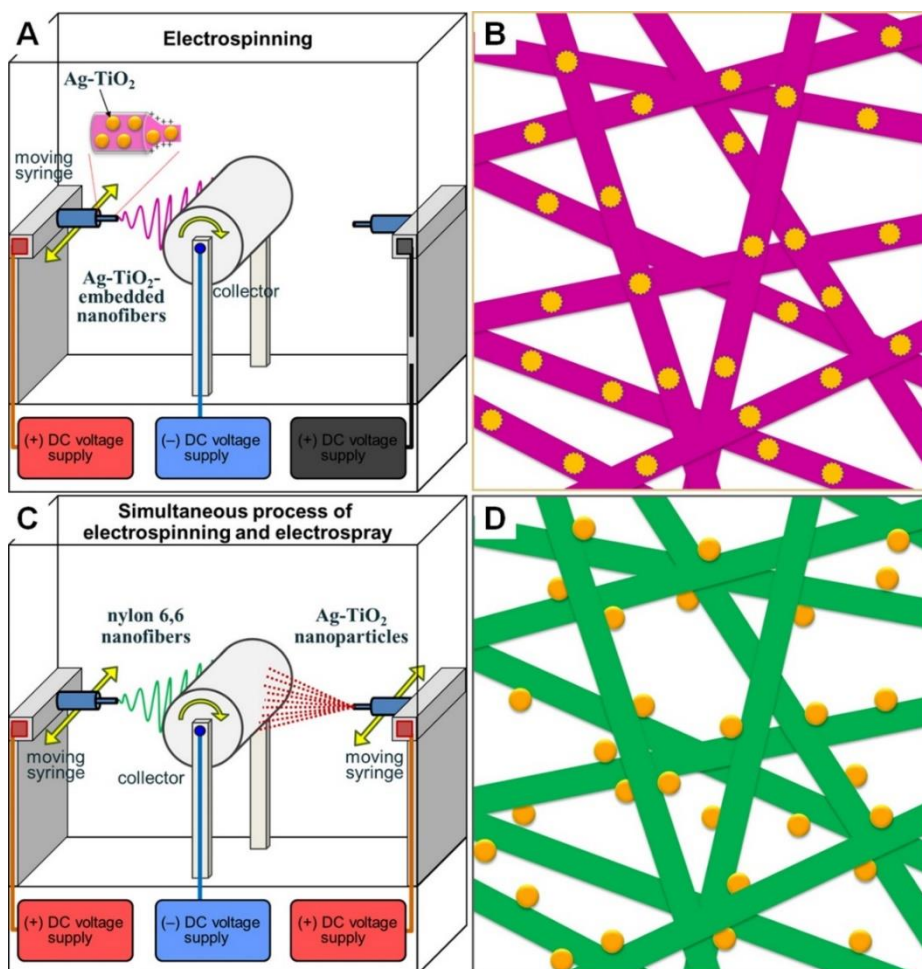


**Figure 2.1.** Schematic representation of (A) electrospinning process used to fabricate (B) the Ag-TiO<sub>2</sub>-embedded nanofiber composite (AT-*in*-NF); and (C) simultaneous electrospinning/electrospraying (SEE) process used to fabricate (D) the Ag-TiO<sub>2</sub>-decorated nanofiber composite (AT-*sur*-NF).

## 2.3 Results and Discussion

### 2.3.1 Synthesis and characterization of Ag-TiO<sub>2</sub>

Ag-TiO<sub>2</sub> had different amounts of Ag by controlling the ratio of Ag precursor to TiO<sub>2</sub>. Prior to Ag deposition, the aqueous TiO<sub>2</sub> dispersion was irradiated with a UV light lamp ( $\lambda = 253.7$  nm, 15 W) for 1 h to generate high hydrophilicity on the TiO<sub>2</sub> surfaces.<sup>28</sup> The aqueous dispersion was then adjusted to pH 8.0–8.2 to ensure effective interaction of Ag<sup>+</sup> ion with the negatively charged TiO<sub>2</sub> surface, because the isoelectric point (IEP) of TiO<sub>2</sub> is around pH 6.0–6.4.<sup>29,30</sup> The photoreduction of Ag<sup>+</sup> ion on the surface of TiO<sub>2</sub> is entirely possible from a thermodynamic point of view. At the beginning of homogeneous nucleation, small clusters of atoms appear in the liquid. In this case, the Gibbs free energy change ( $\Delta G$ ) for homogeneous nucleation in the liquid is

$$\Delta G_{\text{homo}} = -\left(\frac{16\pi}{3}\right)\left(\frac{\sigma^3}{\Delta g^2}\right).$$

where  $\sigma$  is the solid/liquid interface energy, and  $\Delta g$  is the Gibbs free energy change per unit volume. The clusters that overcome this nucleation barrier grow in the liquid, and become large grains. In contrast, when heterogeneous nucleation occurs on a solid substrate, a wetting angle ( $\theta$ ) is formed between each growing nucleus and the surface of the solid, so the Gibbs free energy

change ( $\Delta G$ ) on the surface is

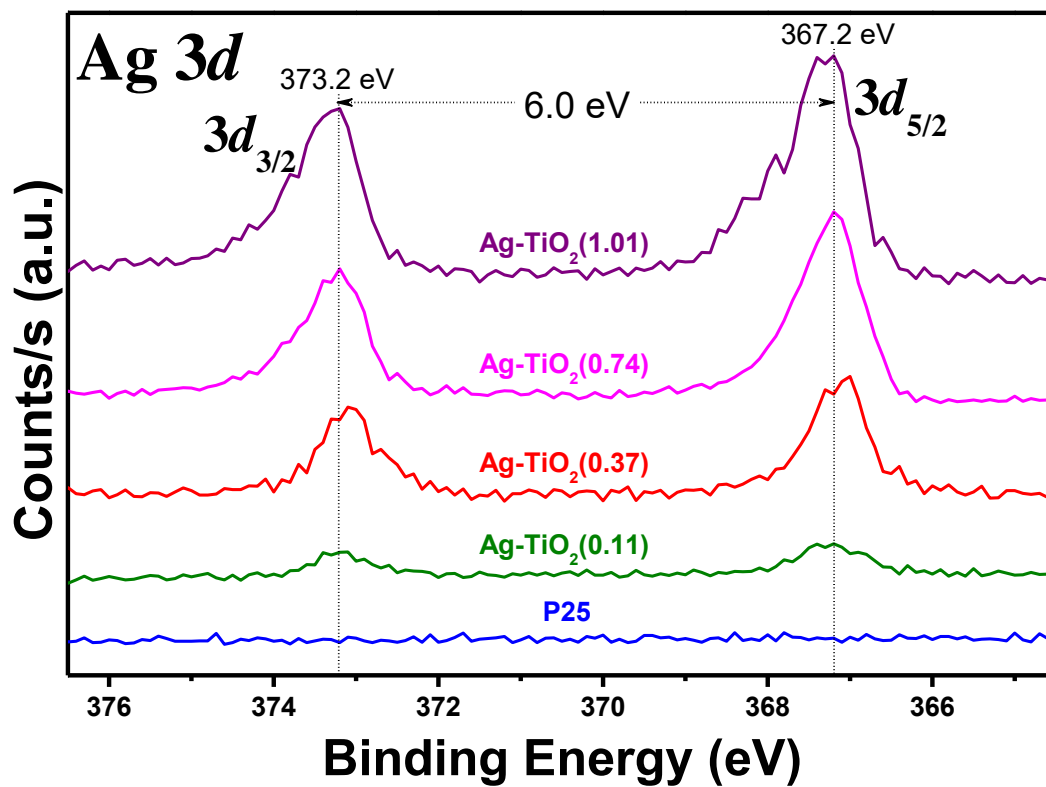
$$\Delta G_{\text{hetero}} = -\left(\frac{16\pi}{3}\right)\left(\frac{\sigma^3}{\Delta g^2}\right)S(\theta), \quad 0 < S(\theta) < 1$$

$$\text{and} \quad S(\theta) = (2 + \cos\theta) (1 - \cos\theta)^2 / 4,$$

where  $S(\theta)$  is the wetting angle factor.<sup>31,32</sup> Considering both cases, the nucleation barrier for the heterogeneous nucleation of Ag clusters on the surface of a substrate is lower than that for its homogeneous nucleation in liquid.<sup>32,33</sup> As a result, the formation of Ag clusters on TiO<sub>2</sub> is more thermodynamically favorable.

As shown in the X-ray photoelectron spectroscopy (XPS) results (Figure 2.2), a small amount of Ag element were found to be present in the synthesized Ag-TiO<sub>2</sub>. In particular, a splitting of 6.0 eV for the Ag 3d<sub>3/2</sub> and Ag 3d<sub>5/2</sub> peaks was observed for all of the Ag-TiO<sub>2</sub> samples, and the peak intensity increased with the amount of Ag precursor added, which indicated that a varied amount of metallic Ag was introduced to the TiO<sub>2</sub>.<sup>34</sup> The atom concentrations of Ag and Ti in the samples were determined by comparing the ratio of the integrated Ag 3d and Ti 2p peak-areas in the XPS spectra. The amount of Ag in Ag-TiO<sub>2</sub> increased with the amount of Ag precursor added, and that the atomic percent ratios of Ag/Ti were 0.11, 0.37, 0.74, and 1.01, for the samples prepared with 2, 5, 10, and 15  $\mu\text{mol}$  of AgNO<sub>3</sub>, respectively. The growth of metallic

Ag on the surface of the TiO<sub>2</sub> was also verified by high resolution transmission electron microscopy (HR-TEM) and field emission scanning electron microscopy/energy-dispersive X-ray spectroscopy (FE-SEM/EDS). As shown in Figure 2.3A–E, many small particles (solid arrow) with an average size of less than 5 nm were highly dispersed on the surface of the TiO<sub>2</sub>. The fast Fourier transform image of one of these small particles showed a d-spacing (0.23 nm) corresponding to the (111) plane of metallic Ag, as in the inset of Figure 2.3B. In addition, Ag-TiO<sub>2</sub> showed rough surface morphology while a smooth surface was observed for P25 (Figure 2.3F). EDS mapping images (see inset of Figure 2.3C, green spots for Ag atoms) revealed that this rough morphology of the Ag-TiO<sub>2</sub> was attributed to the growth of the metallic Ag on the surface of the TiO<sub>2</sub>. The thermodynamic consideration above and the combined XPS, HR-TEM, and FE-SEM/EDS results clearly support the conclusion that metallic Ag clusters grew on the surface of the TiO<sub>2</sub> and that Ag-TiO<sub>2</sub> samples with varied Ag/Ti ratio of  $0.11 \pm 1.01$  were successfully synthesized. The codes and appearance of the samples are presented in Table 2.1.





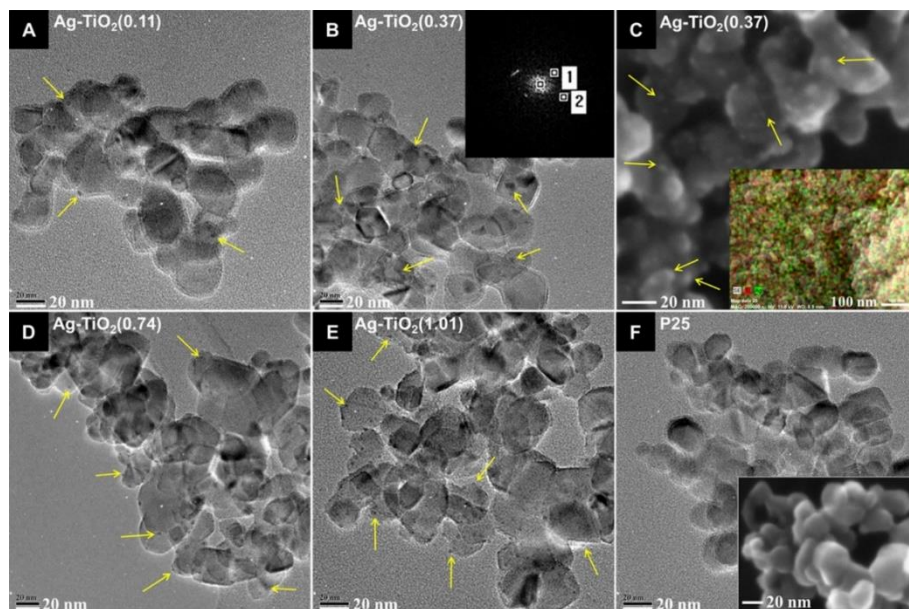



**Figure 2.2.** Ag 3d XPS spectra of Ag-TiO<sub>2</sub> and P25. Values in round brackets indicate the atomic percent ratio of Ag/Ti.



**Figure 2.3.** Morphologies of P25 and Ag-TiO<sub>2</sub> with various Ag content: HR-TEM and FE-SEM images of (A) Ag-TiO<sub>2</sub>(0.11), (B) Ag-TiO<sub>2</sub>(0.37), (C) Ag-TiO<sub>2</sub>(0.37), (D) Ag-TiO<sub>2</sub>(0.74), (E) Ag-TiO<sub>2</sub>(1.01), and (F) P25. Values in round brackets indicate the atomic % ratio of Ag/Ti. (B, inset) Fast Fourier transform (FFT) pattern exhibiting 0.34-nm and 0.23-nm d-spacings corresponding to the (101) plane of standard bulk anatase TiO<sub>2</sub> and the (111) plane of metallic Ag, respectively. (C, inset) EDS mapping image; green and red dots indicate Ag and Ti elements, respectively.

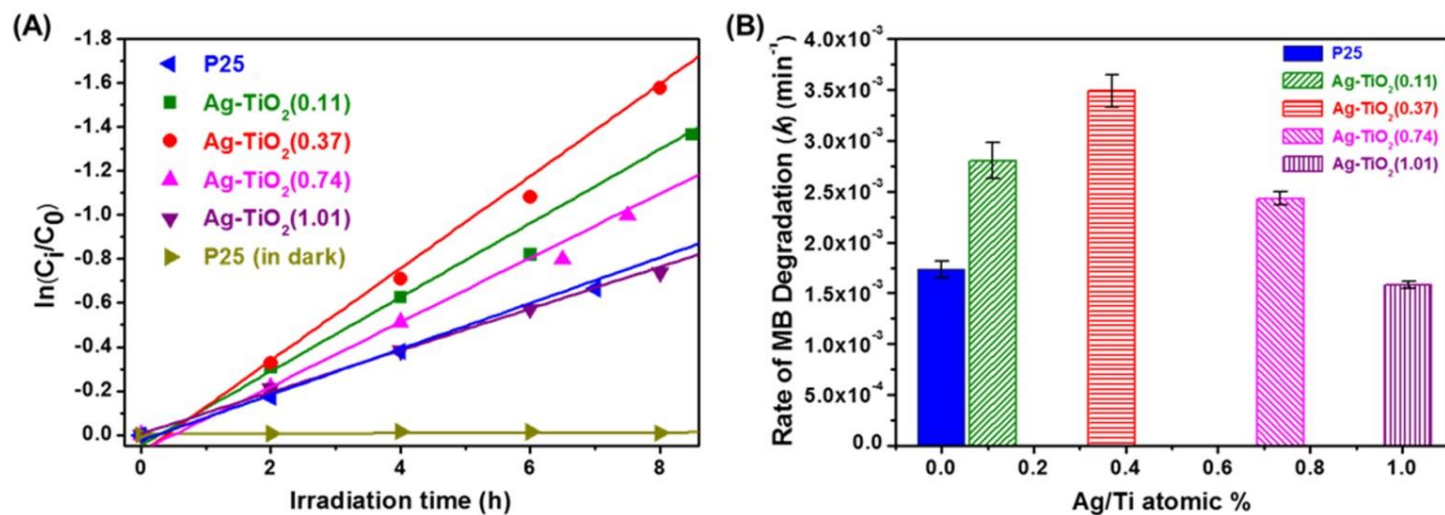


**Table 2.1.** Sample code and appearance of P25 and Ag-TiO<sub>2</sub> nanoparticles with various Ag contents

Sample code	P25	Ag-TiO <sub>2</sub> (0.11)	Ag-TiO <sub>2</sub> (0.37)	Ag-TiO <sub>2</sub> (0.74)	Ag-TiO <sub>2</sub> (1.01)
Image					
Ag/Ti atomic % by XPS	N/A	0.11	0.37	0.74	1.01

The effect of the Ag clusters on the visible light photocatalytic activity of the Ag-TiO<sub>2</sub> was investigated by monitoring the time-dependent photodegradation of methylene blue (MB) in an aqueous Ag-TiO<sub>2</sub> dispersion under visible light irradiation for 24 h at 26 ± 1 °C. The UV-visible spectral absorbance and relative MB concentration ( $C_i/C_0$ ), obtained using UV-visible spectroscopy and the Beer-Lambert law, of the test solution gradually decreased upon visible light irradiation.  $C_i$  is the concentration (mg L<sup>-1</sup>) in the  $i$ th sample, while  $C_0$  is the initial concentration (mg L<sup>-1</sup>). This indicated that MB was photodegraded over the catalysts under the visible light. Moreover, linear fits of  $\ln(C_i/C_0)$  vs. irradiation time indicate that the kinetics of the photocatalytic degradation of the MB can be described using a first-order equation (Figure 2.4A):  $\ln(C_i/C_0) = k_1 \times t$ , where  $k_1$  is the rate constant of the first-order photodegradation, and  $t$  is the visible light irradiation time (min). The rate constants ( $k_1$ ) of MB photodegradation obtained for the different samples are given in Figure 2.4B. Compared with that of P25, the Ag-TiO<sub>2</sub> samples with Ag/Ti atomic % ratios of 0.11, 0.37, and 0.74 exhibited higher  $k_1$  values, indicating faster MB photodegradation rates than P25. Particularly, the Ag-TiO<sub>2</sub> sample with the Ag/Ti atomic % ratio of 0.37 showed the highest  $k_1$  values, which indicated the best visible photocatalytic activity. In contrast, the Ag-TiO<sub>2</sub> sample with 1.01 Ag/Ti atomic % ratio showed lower visible photocatalytic activity than that of P25. This reduced photocatalytic activity can be attributed to a decrease in the

electron density of  $\text{TiO}_2$  and the overloaded Ag acting as a hole trap. Typically, it is known that the enhanced visible light photocatalytic activity of Ag- $\text{TiO}_2$  is caused by the absorption of visible light by metallic Ag species through surface plasmon resonance (SPR).<sup>35</sup> The electrons photogenerated from the Ag clusters by SPR transfer to the conduction band of  $\text{TiO}_2$ . However, in the case of Ag overloading above the optimum content, the increased numbers of Ag clusters attract more electrons, and thereby the decrease in the electron density of  $\text{TiO}_2$ . Such decrease in the electron density of the  $\text{TiO}_2$  surface results in a low photocatalytic activity of the Ag- $\text{TiO}_2$ . In addition, large amounts of Ag clusters on  $\text{TiO}_2$  surface increase the probability of the capture of the holes generated in the  $\text{TiO}_2$ , decreasing the probability of holes reacting with adsorbed species at the Ag- $\text{TiO}_2$  surface<sup>36</sup> and resulting in low photocatalytic activity.

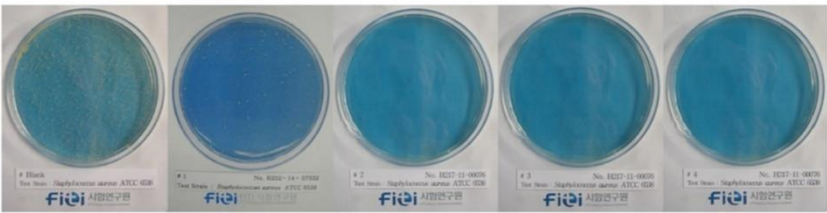



**Figure 2.4.** (A) Pseudo-first-order photodegradation of methylene blue (MB) under visible light irradiation ( $\lambda = 380\text{--}480$  nm) over P25 and Ag-TiO<sub>2</sub>. The slope of the lines corresponds to the rate constant for the photodegradation of MB. (B) Rate constants for MB photodegradation over P25 and Ag-TiO<sub>2</sub> under visible light irradiation, estimated to be about  $1.73 \times 10^{-3}$ ,  $2.80 \times 10^{-3}$ ,  $3.49 \times 10^{-3}$ ,  $2.43 \times 10^{-3}$ , and  $1.58 \times 10^{-3} \text{ min}^{-1}$ , respectively. Values in round brackets indicate the atomic % ratio of Ag/Ti in the samples.

In addition to the photodegradation test, the antimicrobial effect of the Ag-TiO<sub>2</sub> with Ag/Ti atomic % was evaluated using two representative microorganisms, *S. aureus* (ATCC 6538, Gram-positive bacteria) and *E. coli* (ATCC 25922, Gram-negative bacteria). As shown in Figure 2.5, the Ag-TiO<sub>2</sub> samples effectively inhibited the bacterial growth while P25 exhibited a lack of antimicrobial activity against *S. aureus* and *E. coli*. The enhanced antimicrobial activity observed for Ag-TiO<sub>2</sub> was attributed to the disruption of bacterial cells via either leaching of Ag<sup>+</sup> ion or direct contact between microorganisms and Ag on the surface of the Ag-TiO<sub>2</sub>. The combined results of photodegradation and antimicrobial activity tests revealed that the optimization of quantity and distribution of Ag clusters was needed for the optimization of the photocatalytic performance of Ag-TiO<sub>2</sub>, and therefore the Ag-TiO<sub>2</sub> sample containing a 0.37 Ag/Ti atomic % ratio was chosen as the best additive for the nanofiber composites because of its higher visible light photocatalytic activity and excellent antimicrobial activity.

### **2.3.2. Characteristics of Ag-TiO<sub>2</sub>-embedded and decorated nanofiber composites**

Two types of electrospun Nylon 66 nanofiber composites containing Ag-TiO<sub>2</sub> were prepared using electrospinning and simultaneous electrospinning/electrospraying (SEE) process. Ag-TiO<sub>2</sub> was located either in

Bacteria		Blank	P25	Ag-TiO <sub>2</sub> (0.11)	Ag-TiO <sub>2</sub> (0.37)	Ag-TiO <sub>2</sub> (0.74)
<i>S. aureus</i> (ATCC 6538) (CFU/mL)	0 h	$1.5 \times 10^4$	$2.4 \times 10^5$	$1.5 \times 10^4$	$1.5 \times 10^4$	$1.5 \times 10^4$
	24 h	$1.8 \times 10^7$	$3.0 \times 10^5$	< 10	< 10	< 10
	% Reduction		0	99.9	99.9	99.9
	Image					
<i>E. coli</i> (ATCC 25922) (CFU/mL)	0 h	$1.6 \times 10^4$	$2.0 \times 10^5$	$1.6 \times 10^4$	$1.6 \times 10^4$	$1.6 \times 10^4$
	24 h	$9.0 \times 10^7$	$1.6 \times 10^4$	< 10	< 10	< 10
	% Reduction		86.7	99.9	99.9	99.9
	Image					

**Figure 2.5.** Antimicrobial activities of Ag-TiO<sub>2</sub> photocatalysts against *S. aureus* (Gram-positive bacteria) and *E. coli* (Gram-negative bacteria). Values in round brackets indicate the atomic ratio (%) of Ag/Ti in the samples.

the interior or on the surface of the nanofiber matrix, respectively. The effect of Ag-TiO<sub>2</sub> position on the performance of the nanofiber composites was then investigated. As shown in Figure 2.6A-C, the pristine nanofibers and Ag-TiO<sub>2</sub>-embedded nanofiber composite (AT-*in*-NF) had quite similar morphology with an average diameter of  $163 \pm 21$  nm, a smooth surface, and a continuous shape without defects such as beads. In the case of AT-*in*-NF, the presence of Ag-TiO<sub>2</sub> in the nanofibers was verified by charge contrast imaging at high acceleration voltage, which indicated that Ag-TiO<sub>2</sub> was well embedded in the interior of nanofiber by the electrospinning of the polymer/Ag-TiO<sub>2</sub> mixture (Figure 2.6D). In the case of the Ag-TiO<sub>2</sub>-decorated nanofiber composite (AT-*sur*-NF), the electrosprayed Ag-TiO<sub>2</sub> was well dispersed on the nanofiber surface without the formation of large aggregates. Figure 2.6F shows that the Ag-TiO<sub>2</sub> particles were fixed more tightly to the surface of nanofibers after the heat-pressing treatment compared with those of the as-prepared AT-*sur*-NF (Figure 2.6E).

The thermogravimetric analysis (TGA) results (Figure 2.7) showed that all of the nanofibrous samples had a significant weight loss at 430 °C and revealed that both nanofiber composites (AT-*in*-NF and AT-*sur*-NF) had almost same Ag-TiO<sub>2</sub> content. Meanwhile, the differential thermogravimetry curves indicated that the nanofiber composites began to thermally decompose slightly earlier than the pristine nanofibers.

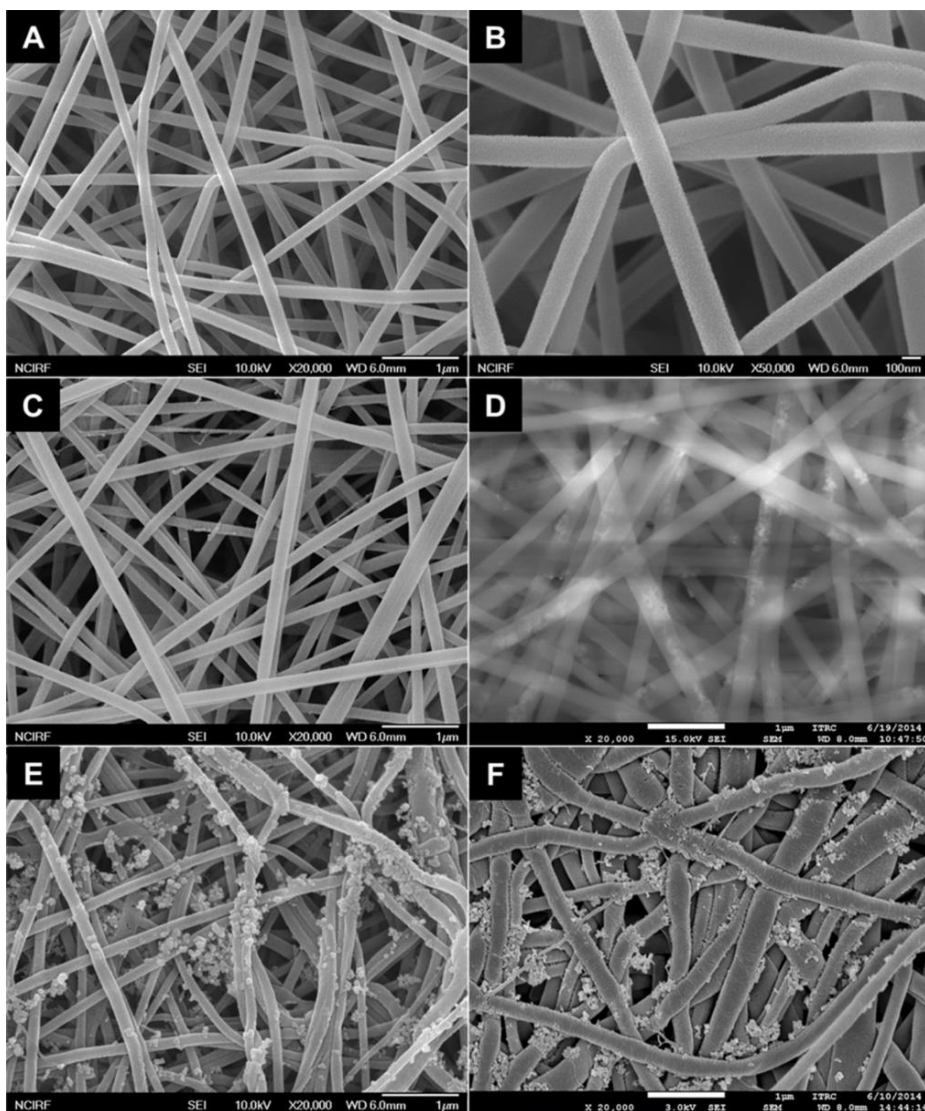


**Figure 2.6.** Morphology of (A and B) the pristine nanofiber, (C) the Ag-TiO<sub>2</sub>-embedded nanofiber composite (AT-*in*-NF), (D) AT-*in*-NF observed with higher acceleration voltage to check the presence of Ag-TiO<sub>2</sub> in the interior of nanofibers, (E) as-prepared Ag-TiO<sub>2</sub>-decorated nanofiber composite (AT-*sur*-NF), and (F) heat-pressed AT-*sur*-NF.



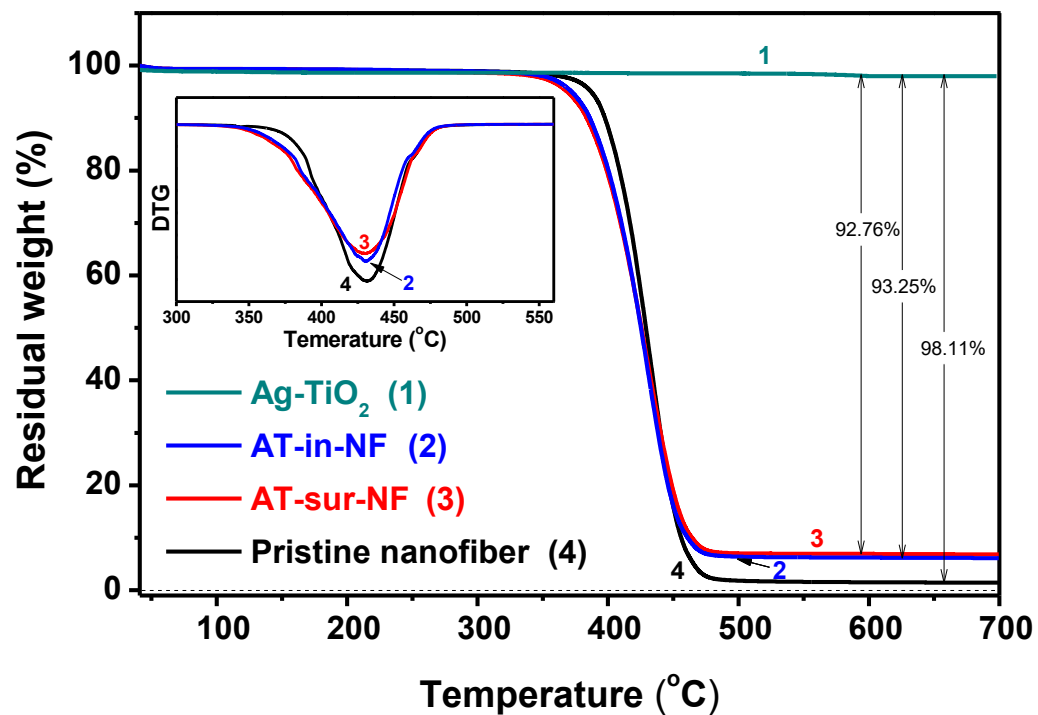


**Figure 2.7.** Residual weight and derivative weight loss (inset) versus temperature (heating rate of 10 °C/min) of Ag-TiO<sub>2</sub>, pristine nanofiber, Ag-TiO<sub>2</sub>-embedded nanofiber composite (AT-*in*-NF), and Ag-TiO<sub>2</sub>-decorated nanofiber composite (AT-*sur*-NF).

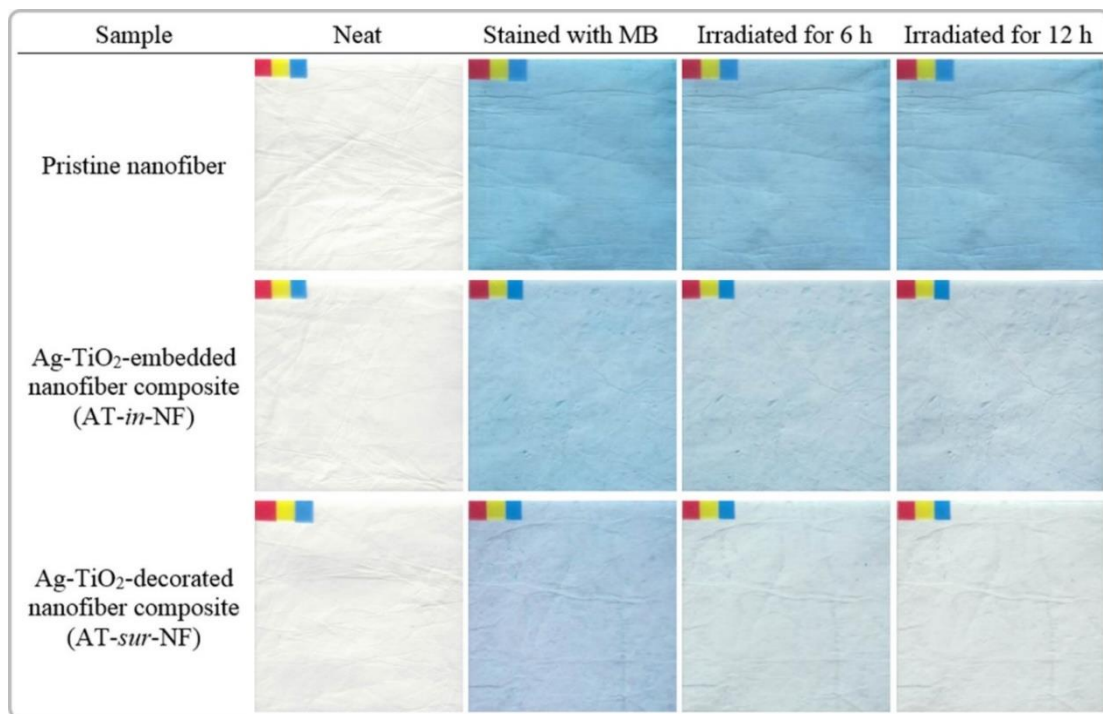
### 2.3.3. Photocatalytic and antimicrobial activities of Ag-TiO<sub>2</sub>-embedded and decorated nanofiber composites

The photo-induced self-cleaning ability of the nanofiber composites was evaluated by testing their photodegradation of a MB stain under visible light irradiation. The decolorization of MB on all samples as a function of irradiation time was qualitatively assessed. As shown in Figure 2.8, the color of the stained nanofiber composites gradually faded, while no significant change in the blue color was observed for the pristine nanofiber despite the irradiation. In the case of AT-*in*-NF, the blue color still remained even after 6 h irradiation. However, the blue color nearly disappeared when AT-*sur*-NF was irradiated for 6 h. This distinct difference in color change indicates that AT-*sur*-NF had a more efficient, photo-induced self-cleaning ability than AT-*in*-NF. The degree of the photo-induced self-cleaning was quantitatively evaluated by measuring color strength ( $f_k$ ), which is a visually weighted function of  $K/S$  values, using a spectrophotometer. The color strength ( $f_k$ ) is

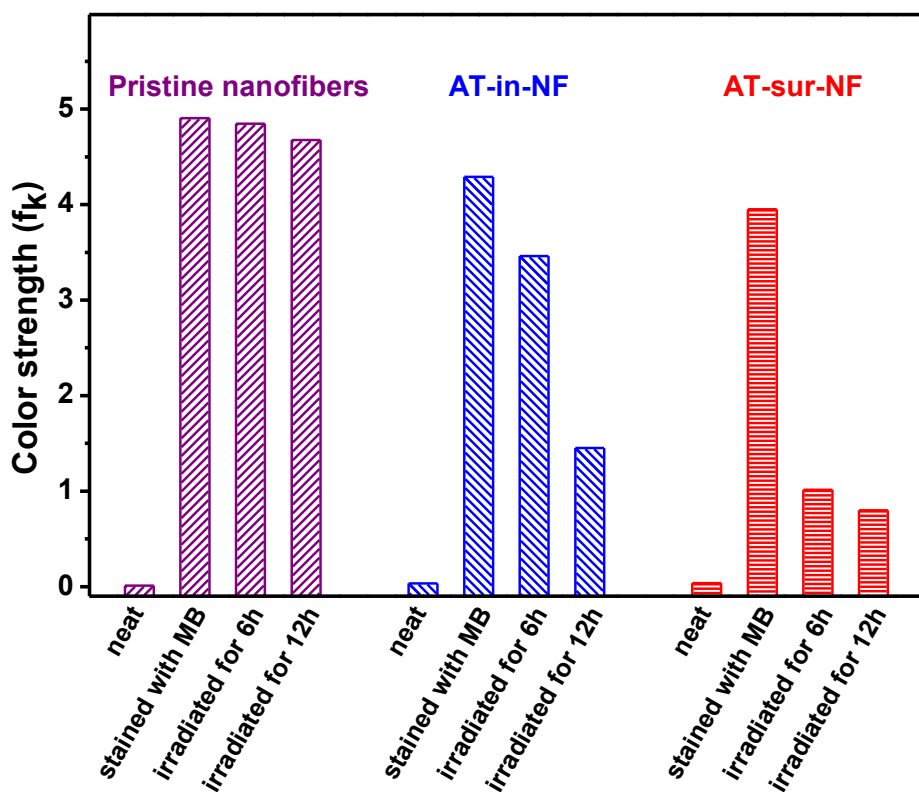
$$f_k = \sum_{\lambda=400}^{700} \left( \frac{K}{S} \right)_{\lambda} (\bar{x}_{10,\lambda} + \bar{y}_{10,\lambda} + \bar{z}_{10,\lambda})$$

where  $K$  is the sorption coefficient,  $S$  is the scattering coefficient,  $x_{10,\lambda}$ ,  $y_{10,\lambda}$ , and  $z_{10,\lambda}$  are the color matching functions for the standard observer (10°) from 400 to 700 nm wavelength (ISO 7724/1-1984).<sup>37,38</sup> As shown in Figure 2.9,

compared with the pristine nanofibers, the  $f_k$  value for the nanofiber composites decreased with the irradiation time, and the  $f_k$  value of AT-*sur*-NF in particular decreased markedly after 6 h irradiation. This result revealed that AT-*sur*-NF had better photo-induced self-cleaning ability than AT-*in*-NF. The AT-*in*-NF and AT-*sur*-NF were prepared to have similar Ag-TiO<sub>2</sub> content (Figure 2.7). On the basis of qualitative and quantitative evaluations, therefore, the discrepancy of the degree of photodegradation between the nanofiber composites can be considered to entirely result from the positioning of the Ag-TiO<sub>2</sub>, *i.e.*, in other words, the positioning of Ag-TiO<sub>2</sub> on the nanofiber surface plays an important role in improving the photocatalytic efficiency. The superior photocatalytic performance of AT-*sur*-NF can be explained by a difference in interactions between MB molecules and the reactive species, *e.g.*, hydroxyl radicals, produced from the Ag-TiO<sub>2</sub>. In the case of AT-*sur*-NF, hydroxyl radicals could easily make contact with MB owing to the exposure of Ag-TiO<sub>2</sub>, whereas AT-*in*-NF had a low probability of contact between MB and hydroxyl radicals generated inside the nanofibers. Thus, the interaction between MB and hydroxyl radicals occurred efficiently in AT-*sur*-NF, which led to the rapid color change and dramatic decrease in the value of  $f_k$ .



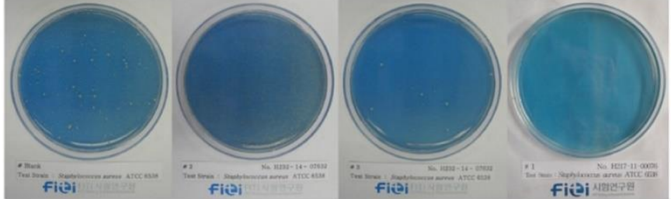
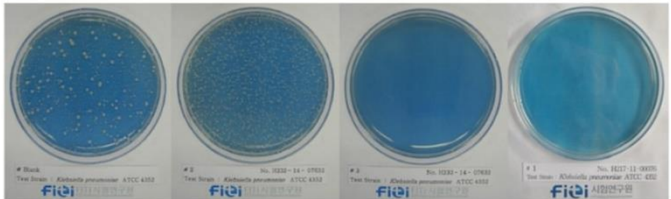
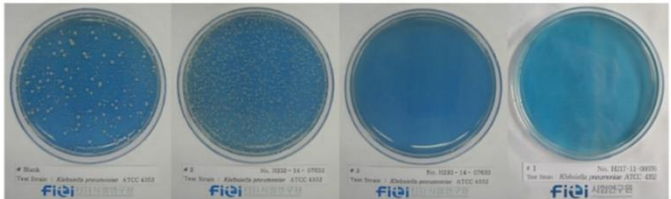
**Figure 2.8.** Visible light photocatalytic decolorization of methylene blue over pristine nanofiber, Ag-TiO<sub>2</sub>-embedded nanofiber composite (AT-*in*-NF), and Ag-TiO<sub>2</sub>-decorated nanofiber composite (AT-*sur*-NF). Red, yellow, and blue stickers are placed on the top left of the figures for color comparison.



**Figure 2.9.** Dependence of color strength ( $f_k$ ) of untreated and stained samples with methylene blue (MB) on visible light irradiation ( $\lambda = 380\text{--}480\text{ nm}$ ): (left) pristine nanofiber, (center) Ag-TiO<sub>2</sub>-embedded nanofiber composite (AT-*in*-NF), and (right) Ag-TiO<sub>2</sub>-decorated nanofiber composite (AT-*sur*-NF).

The effect of the Ag-TiO<sub>2</sub> position on the antimicrobial activity of the nanofiber composites was examined using *S. aureus* (ATCC 6538, Gram-positive bacteria) and *K. pneumoniae* (ATCC 4352, Gram-negative bacteria) according to AATCC 100:2012. The results presented in Figure 2.10 show that the pristine nanofibers were attacked by the bacteria mass whereas the nanofiber composites inhibited the bacterial growth by over 99.9%, with the exception of the antimicrobial activity of AT-*in*-NF against *S. aureus* (< 95%). Generally, the antimicrobial activity of Ag-TiO<sub>2</sub> is thought to be induced by either leaching of Ag<sup>+</sup> ion or direct contact between microorganisms and Ag. It is known that leached Ag<sup>+</sup> ion shows weaker antimicrobial activity against Gram-positive bacteria such as *S. aureus* owing to electrostatic repulsion. In the case of AT-*in*-NF, the antimicrobial effect was likely mainly brought about by the leaching of Ag<sup>+</sup> ion because it was impossible for the microorganism to directly contact the Ag-TiO<sub>2</sub> inside the nanofiber. Moreover, the Ag<sup>+</sup> ion leaching efficiency of AT-*in*-NF may have been depressed owing to disturbance by the nanofibers. Thus, the disadvantaged position of Ag-TiO<sub>2</sub> in the nanofibers may have reduced the antimicrobial activity of AT-*in*-NF. Conversely, the Ag-TiO<sub>2</sub> in AT-*sur*-NF was able to both come in contact with the microorganism and freely leach Ag<sup>+</sup> ion (or Ag). This can lead to an excellent antimicrobial activity irrespective of the charge of the microorganism, thereby resulting in its better antimicrobial activity than that of AT-*in*-NF. Consequently, the strong

antimicrobial activity of AT-*sur*-NF compared with that of AT-*in*-NF can be attributed to the exclusive deposition of Ag-TiO<sub>2</sub> on the nanofiber surface.

Bacteria		Blank	Pristine nanofiber	Ag-TiO <sub>2</sub> -embedded nanofiber composite (AT- <i>in</i> -NF)	Ag-TiO <sub>2</sub> -decorated nanofiber composite (AT- <i>sur</i> -NF)
<i>S. aureus</i> (ATCC 6538) (CFU/mL)	0 h	$1.0 \times 10^5$	$1.0 \times 10^5$	$1.0 \times 10^5$	$2.5 \times 10^5$
	18 h	$1.0 \times 10^8$	$2.0 \times 10^8$	$5.0 \times 10^3$	< 100
	% Reduction		0	95.0	> 99.9
	Image				
					
<i>K. pneumoniae</i> (ATCC 4352) (CFU/mL)	0 h	$1.3 \times 10^5$	$1.3 \times 10^5$	$1.3 \times 10^5$	$1.5 \times 10^5$
	18 h	$1.0 \times 10^8$	$1.5 \times 10^8$	< 100	< 100
	% Reduction		0	> 99.9	> 99.9
	Image				

**Figure 2.10.** Antimicrobial activities of pristine nanofiber, Ag-TiO<sub>2</sub>-embedded nanofiber composite (AT-*in*-NF), and Ag-TiO<sub>2</sub>-decorated nanofiber composite (AT-*sur*-NF) against *S. aureus* (Gram-positive bacteria) and *K. pneumoniae* (Gram-negative bacteria).



## 2.4. Summary

This study described the position effect of Ag-TiO<sub>2</sub> on the photocatalytic and antimicrobial activities of the nanofiber composites under visible light condition. To achieve this, the visible light active Ag-TiO<sub>2</sub> was synthesized and then introduced to the nanofiber using sole electrospinning and simultaneous electrospinning/electrospraying (SEE) process, resulting in Ag-TiO<sub>2</sub>-embedded nanofiber (AT-*in*-NF) and Ag-TiO<sub>2</sub>-decorated nanofiber (AT-*sur*-NF) composites, respectively. Interestingly, AT-*sur*-NF with Ag-TiO<sub>2</sub> exposed on the nanofiber surface had both better photocatalytic and antimicrobial activities than AT-*in*-NF with Ag-TiO<sub>2</sub> located inside the nanofiber, although the Ag-TiO<sub>2</sub> content in the two types of nanofiber composite was controlled to be the same. These findings revealed that the position of Ag-TiO<sub>2</sub> plays an important role in the performance of nanofiber composites. Hence, AT-*sur*-NF can be usefully applied as a protective material against various contaminants such as organic pollutants, harmful particulates, bacteria, and viruses. Furthermore, these results will enable the design and production of nanofiber composites with superior performance.

## References

1. Reneker, D.H. and Chun, I., *Nanotechnology*, **1996**, 7, 216.
2. Li, D.; Xia Y. *Adv. Mater.* **2004**, 16, 1151.
3. Cai, Y.; Wang, Q.; Wei, W.; You, Q.; Huang, F.; Song, L.; Hu, Y.; Gao, W. *Int. J. Polym. Anal. Charact.* **2010**, 15, 110.
4. Barhate, R. S.; Ramakrishna, S. *J. Membr. Sci.* **2007**, 296, 1.
5. Li, W. J.; Laurencin, C. T.; Caterson, E. J.; Tuan, R.S.; Ko, F. K. *J. Biomed. Mater. Res. A* **2002**, 60, 613.
6. Virji, S.; Huang, J.; Kaner, R. B.; Weiller, B. H. *Nano Lett.* **2004**, 4, 491.
7. Bao, Q.; Zhang, H.; Yang, J.; Wang, S.; Tang, D. Y.; Jose, R.; Ramakrishna, S.; Lim, C. T.; Loh, K. P. *Adv. Funct. Mater.* **2010**, 20, 782.
8. Yoo, H. S.; Kim, T. G.; Park, T. G. *Adv. Drug Deliv. Rev.* **2009**, 61, 1033.
9. Ramakrishna, S.; Fujihara, K.; Teo, W. E.; Yong, T.; Ma, Z.; Ramaseshan, R. *Mater. Today* **2006**, 9, 40.
10. Weng, B.; Xu, F.; Salinas, A.; Lozano, K. *Carbon* **2014**, 75, 217.
11. Ko, F.; Gogotsi, Y.; Ali, A.; Naguib, N.; Ye, H.; Yang, G.; Li, C.; Willis, P. *Adv. Mater.* **2003**, 15, 1161.
12. Wang, Y.; Yang, Q.; Shan, G.; Wang, C.; Du, J.; Wang, S.; Li, Y.; Chen, X.; Jing, X.; Wei, Y. *Mater. Lett.* **2005**, 59, 3046.
13. Sundarrajan, S.; Ramakrishna, S. *J. Mater. Sci.* **2007**, 42, 8400.
14. Chen, X.; Mao, S. S. *Chem. Rev.* **2007**, 107, 2891.
15. Eiden-Assmann, S.; Widoniak, J.; Maret, G. *Chem. Mater.* **2004**, 16, 6.
16. Tachikawa, T.; Fujitsuka, M.; Majima, T. *J. Phys. Chem. C* **2007**, 111, 5259.
17. Grätzel, M. *Prog. Photovoltaics* **2000**, 8, 171.
18. Asahi, R.; Morikawa, T.; Ohwaki, T.; Aoki, K.; Taga, Y. *Science* **2001**, 293, 269.
19. Chen, D.; Zhang, H.; Hu, S.; Li, J. *J. Phys. Chem. C* **2008**, 112, 117.

20. Zhang, H.; Wang, G.; Chen, D.; Lv, X.; Li, J. *Chem. Mater.* **2008**, *20*, 6543.
21. Hirakawa, T.; Kamat, P. V. *Langmuir* **2004**, *20*, 5645.
22. Awazu, K.; Fujimaki, M.; Rockstuhl, C.; Tominaga, J.; Murakami, H.; Ohki, Y.; Yoshida, N.; Watanabe, T. *J. Am. Chem. Soc.* **2008**, *130*, 1676.
23. Hu, C.; Lan, Y.; Qu, J.; Hu, X.; Wang, A. *J. Phys. Chem. B* **2006**, *110*, 4066.
24. Ansari, M. O.; Khan, M. M.; Ansari, S. A.; Lee, J.; Cho, M. H. *RSC Adv.* **2014**, *4*, 23713.
25. Kim, C. H.; Kim, B. H.; Yang, K. S. *Synth. Met.* **2011**, *161*, 1068.
26. Amarjargal, A.; Tijing, L. D.; Ruelo, M. T. G.; Lee, D. H. *Mater. Chem. Phys.* **2012**, *135*, 277.
27. Kirchnerova, J.; Herrera Cohen, M.-L.; Guy, C.; Klvana, D. *Appl. Catal. A* **2005**, *282*, 321.
28. Ryu, S.-Y.; Kim, D. S.; Jeon J.-D.; Kwak, S.-Y. *J. Phys. Chem. C* **2010**, *114*, 17440.
29. Long, T.C.; Saleh, N.; Tilton, R. D.; Lowry, G. V.; Veronesi, B. *Environ. Sci. Technol.* **2006**, *40*, 4346.
30. Bourikas, K.; Hiemstra, T.; Van Riemsdijk, W. H. *Langmuir* **2001**, *17*, 749.
31. *Fundamentals of Solidification*; Kurz, W.; Fisher, D. J.; Trans Tech Publications Ltd: Switzerland, 1998.
32. *Phase Transformations in Metals and Alloys*; Porter, D. A.; Easterling, K. E.; Sherif, M. Y.; CRC Press: Boca Raton, FL, 2009.
33. Jung, I. H.; Bae, K. K.; Song, K. C.; Yang, M. S.; Ihm, S. K. *J. Therm. Spray. Technol.* **2004**, *13*, 544.
34. Sanjinés, R.; Tang, H.; Berger, H.; Gozzo, F.; Margaritondo, G.; Lévy, F. *J. Appl. Phys.* **1994**, *75*, 2945.
35. You, X.; Chen, F.; Zhang, J.; Anpo, M. *Catal. Lett.* **2005**, *102*, 247.
36. Scalfani, A. *J. Photochem. Photobio. A-Chem.* **1991**, *59*, 181.

37. Baumann, W.; Groebel, B. T.; Kraye, M.; Oesch, H. P.; Brossman, R.; Kleinemeier, N.; Leaver, A. T. *J. Soc. Dye. Colour* **1987**, *103*, 100.
38. Koh, J.; Cho, D. H. *Fiber. Polym.* **2004**, *5*, 134.

## **Chapter 3**

# **Nanofibrous Inner Layer of Chemical Warfare Protective Materials with Adsorptivity of Chemical Warfare Agents**

### **3.1 Introduction**

Chemical warfare agents (CWA) have been exploited in the tactical warfare as the form of incendiary mixtures, smokes, or irritant, burning, poisonous, or asphyxiating gases.<sup>1</sup> CWAs has been classified according to their target organs or tissues: nerve agents, vesicant agents, choking agents, blood agents, incapacitants, lacrimators and vomiting agents.<sup>2</sup> Especially many CWA are dermally active, and so, a number of studies have presented about materials for protection against CWA.<sup>3-5</sup> Furthermore, there are various types of defense equipments to protect the body from CWA: detector, respirator, protective clothing (garment), decontaminants and medical countermeasures.<sup>6</sup> The protective clothing is roughly classified into two types: impermeable and permeable cases as shown in Figure 3.1. An impermeable protective clothing offers powerful protection against CWA, but it is unfit for the long-term working due to the cumbersomeness and uncomfortability.

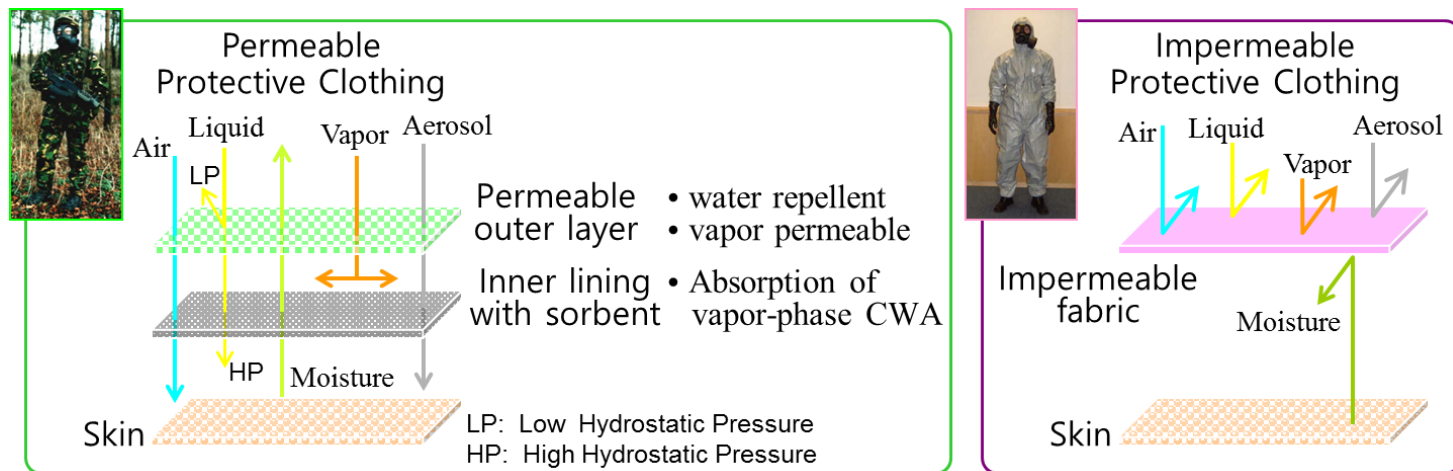


Figure 3.1. Schematic representations of the chemical warfare protective clothing.

In contrary, a permeable protective clothing is composed with outer and inner layers having breathability. The outer layer has been developed to repel the liquid CWA which is trying to invade in the protective clothing. In addition, the inner layer is consisted of nonwoven fabric or porous foam impregnated with adsorbents, such as activated carbon to chemisorb the gas CWA entering through the outer layer. The activated carbon materials used in that is impregnated with nanoparticles of silver, tin, zinc and molybdenum and the complex triethylene diamine. A popular example of the permeable protective overgarment would be the Joint Service Lightweight Integrated Suit Technology (JSLIST) overgarment, which has been used in the US Army.<sup>7</sup> This suit offers complete protection against CWA, but, it is also associated with disadvantages such as moisture retention and heavy weight (2.63 kg per overgarment) resulting in discomfort. These disadvantages prevent the user from using that suit for a long time more than 6–8 h. Therefore, there is a need for a more comfortable material, which possesses the lightness and high moisture permeability.

A number of studies have presented about new protective clothing materials, which are much more adsorptive, light and comfortable. As the incorporated filler in the permeable protective clothing, catalysts and adsorbents with detoxification activity such as MgO,<sup>8,9</sup> MnO<sub>2</sub>,<sup>10</sup> ZnO,<sup>11,12</sup> TiO<sub>2</sub>,<sup>13</sup> ZnTiO<sub>3</sub>,<sup>14</sup> M/TiO<sub>2</sub>/SiO<sub>2</sub> (M = Fe, Mn, and V),<sup>15</sup> WO<sub>3</sub>/titanate,<sup>16</sup> N-doped TiO<sub>2</sub>,<sup>17</sup>

Au/TiO<sub>2</sub>,<sup>18</sup> and polyoxometalate (POM)<sup>19</sup> have been investigated actively. Among them, MgO are widely studies as effective catalyst against the nerve agent such as Sarin (GD) of CWA because it is highly active to decompose nerve agent very effectively.<sup>20</sup> MgO can physisorb CWA on the surface of MgO through the formation of hydrogen-bonding, ion-dipole and dipole-dipole interactions.<sup>21</sup> In addition, POM has been under consideration mainly as reactive adsorbent for the decontamination of the blister agent such as sulfur mustard (HD) of CWA.<sup>22</sup>

The disadvantage of the currently used permeable protective clothing can be also improved by replacing with light-weight materials and structure such as nanofiber. Nanofiber show an improved properties in comparison to the conventional fibers due to its dimensions and unique features as follows: high surface-to-volume ratio, small fiber-to-fiber distance, high porosity, large specific surface area, small pore size, and high controllability. These unique characteristics plus the functionalities from the materials themselves impart nanofibers with a number of novel properties for advanced applications.

Herein, a potential application of nanofibrous composite materials impregnated the MgO and POM adsorbents was demonstrated as an inner layer for the permeable protective clothing against CWA. In order to select the adsorbents to be incorporated in the nanofiber composites for nanofibrous inner layer, the absorptivity of 2-chloroethyl ethyl sulfide (2-CEES) and dimethyl methyl



phosphonate (DMMP) as simulants of CWA on the 7 types of commercial MgO and 3 types of POM. Then, the nanofiber composites, which consisted of both polyamide 66 nanofiber and adsorbents (MgO and POM), were prepared using the simultaneous electrospinning and electrospraying (SEE) process. The nanofiber composites were compared to neat polyamide 66 nanofiber mat by evaluating the permeability of air, moisture and gas simulant for CWA. The nanofiber composite was found to have superior water vapor transmittance and protectability against CWA simulants. The incorporation of the MgO and POM is an important factor in the enhanced protectability. In addition, the nanofibrous material provides a solution to overcome the problem of moisture retention for the currently applied protective clothing of Korea Army. These findings suggest the high possibility of the application of the nanofiber composites to the inner layer of permeable protective clothing.

## 3.2 Experiments

### 3.2.1 Adsorptivity of chemical warfare agent simulants on MgO and POM particles

2-chloroethyl ethyl sulfide (2-CEES; 98% GC purity, Sigma-Aldrich) and dimethyl methyl phosphonate (DMMP, 97% GC purity, Sigma-Aldrich) were chosen as chemical warfare agent (CWA) simulants of mustard (HD) and Sarin (GB), respectively. All of the materials were used as received without further purification. Commercial magnesium oxide (MgO) (light and heavy grade), ammonium (para) tungstate hydrate  $((\text{NH}_4)_{10}(\text{H}_2\text{W}_{12}\text{O}_{42}) \cdot 4\text{H}_2\text{O})$ , and ammonium phosphomolybdate hydrate  $((\text{NH}_4)_3\text{PMo}_{12}\text{O}_{40} \cdot n\text{H}_2\text{O})$  as adsorbents of the CWA simulants were purchased from various manufactures, and the detail description was listed in Table 3.1. All samples were stored ambient condition before an adsorption test. The adsorption of the simulants on the adsorbents were measured according to the ASTM D5160-95 method.<sup>23</sup> The 500 mg of adsorbents were fixed on a cylindrical sample chamber with 10 mm radius, and the adsorption temperature was controlled to 25 °C. The simulants solution (1 % V/V in ethanol) was purged by dry N<sub>2</sub> gas, so that the adsorbate vapor was generated continuously, and the vapor was passed through the adsorbents at a flow rate 50 ccm for 40 min. The passed-out gas was trapped in the Tenax-TA tube, and desorption of the simulants trapped in the Tenax-TA

tube was conducted using thermal desorption gas chromatograph mass spectrometry (TDS-GC-MS, GC: 6890N, Agilent; MSD: 5975, Agilent; TDS: TDS2, Gerstel). As adsorbents showing best performance, one type of MgO and POM were selected, respectively. And then, they were introduced onto the polymeric nanofiber for inner and outer layer of protective materials against CWA using the simultaneous electrospinning and electrospray (SEE) process.

### **3.2.2 Nanofibrous inner layer for adsorptive protection against chemical warfare simulants**

Poly(hexamethylene adipamide) (Nylon 66, aliphatic polyamide, Sigma-Aldrich), formic acid ( $\geq 95\%$ , Sigma-Aldrich) and benzyl trimethyl ammonium chloride (BTMAC,  $\geq 99.0\%$ , Tokyo Chemical Industry) were used as received without further purification. The nanofiber composite for inner layer, consisted with polyamide 66 nanofiber (PANF) and the selected adsorbent (MgO or POM), was prepared using the simultaneous electrospinning/electrospraying (SEE) process as in Figure 2.1C. For the electrospinning of polyamide nanofibers (PANF), 5.4 g of the Nylon 66 pellets were dissolved in 36 mL of formic acid solution with 0.54 g of BTMAC as a salt and mildly shaken for 24 h at room temperature until the solution was clearly transparent. The resulting solution was electrospun using the following conditions: 0.33-mm inner-diameter stainless steel spinneret, 18–20

kV at the spinneret, -5 kV at the collector, 9 cm tip-to-collector distance, collector rotation speed of 100 rpm, and solution flow rate of 1.0 mL/h for 10 h at  $22 \pm 1$  °C and  $50 \pm 5$  % relative humidity. At the same time, for the electrospray to introduce the adsorbents on the surface of PANF, 1 g of the adsorbents was dispersed in 100 mL methanol using a horn-type ultrasonicator (VCX-750, Sonics & Materials, CT, USA) for 30 min. The dispersion was then electrosprayed using the following conditions: 0.51-mm inner diameter stainless steel spinneret, 12 kV at spinneret, 10 cm tip-to-collector distance, and solution flow rate of 10.0 mL/h for 10 h. The as-prepared sample was annealed at 80 °C for 30 min in a processing oven (UF 110, Memmert, Germany) to adhere the adsorbents on the surface of the nanofibers, and finally, the nanofiber composites ([I]MgO/PANF and [I]POM/PANF) for inner layers with protectability against gas CWA were prepared. The nanofiber composites were washed four times with deionized water/methanol solution to remove the salt and any unbound adsorbents from the nanofibers. All washed samples were dried at room temperature for 1 day in air and a vacuum oven, and stored in a vacuum desiccator.

The morphology of the nanofiber composites was evaluated by FE-SEM (JSM-6335F; JEOL and SUPRA 55VP; Carl Zeiss). The content of the adsorbents (MgO and POM) in the composites was determined by thermogravimetric analysis (TGA; Q5000 IR, TA Instruments; ramp rate 10 °C/min, 40–600 °C,

N<sub>2</sub> atmosphere). The flow pore diameter and distribution of the nanofiber mats were measured using a capillary flow porometer (CFP-1500AEL; Porous Material Inc., USA) using SilWick silicone fluid (Porous Materials Inc.) with a surface tension of 19.1 dynes/cm as the wetting agent for porometry measurements. And air gas (0–100 psi) used as a working gas (N<sub>2</sub>). The pore size and distribution were calculated by the software from Porous Media Inc. using the following equations:

$$d = C\gamma/p$$

where  $d$  is maximum pore diameter;  $C$  is constant (0.415 when  $p$  is in psi);  $\gamma$  is the surface tension of wetting liquid;  $p$  is the differential pressure.

$$Q = (\text{wet flow}_h / \text{dry flow}_h - \text{wet flow}_l / \text{dry flow}_l) \times 100$$

$$D = (Q - Q_L) / (d_L - d)$$

where  $Q$  is flow percentage of nanofiber mat;  $h$  is higher pressure limit;  $l$  is lower pressure limit;  $D$  is pore size distribution;  $d$  is maximum pore diameter;  $L$  is previous value.

Air permeability of the nanofiber mats was measured using an ASTM D737 standard method, and the schematic representation of the experimental system are shown in Figure 3.2A. The water vapor transmission rate (WVTR) of the nanofiber mats was evaluated using an ASTM E96 standard method as shown in Figure 3.2B. An open cup containing water was sealed with the nanofiber mat in such a manner that the cup mouth defined the area of the nanofiber mats

exposed to the vapor pressure in the cup. The assembly was placed in a chamber at  $40 \pm 1$  °C with 40 %RH. And then, the weight was recorded after 24 hours. These procedure repeated five times, and the results averaged.

The permeation of gas CWA simulants (2-CEES and DMMP) through the nanofiber mats was determined by the permeation experiment of the direct contact and dynamic diffusion types according to modified ASTM F739 method as exhibited in Figure 3.3. In order to produce the gas of CWA simulants, the 1 mL of 2-CEES ( $< 3.4$  mmHg of vapor pressure at 25 °C and  $16,570 \text{ mg/m}^3$  of volatility at 20 °C) was added to 199 of ethanol, and 10 mL of DMMP (1 mmHg of vapor pressure at 25 °C and  $347 \text{ mg/m}^3$  of volatility at 20 °C) was added to 190 mL of ethanol. Then each 200 mL of CWA simulants/ethanol solution was put in a bubbler and located in a water bath at a temperature of  $74 \pm 1$  °C. This action was taken to ensure that the simulants gas in tubing was formed effectively and was maintained at the same temperature. In the case of a direct contact type experiment,  $\text{N}_2$  gas, which was regulated using a flow meter ((Mass Flow Controller, MKP, MPR-3000s) with a flow rate of 50 cc/min (50 mL/min), delivered gas CWA simulants to the Nylon 66 nanofiber mats for 20 min. Then the simulants gas (1,000 cc) passed through the mats ( $4.9 \text{ cm}^2$  of area and  $91 \text{ }\mu\text{m}$  of thickness) and were collected by the TENAX-TA tube. The captured gas was evaluated by

thermal desorption gas chromatography with mass spectrometer (TD-GC-MS). The associated equipments were connected with Teflon and Tygon tubing. In the case of a dynamic diffusion type experiment, there are two lines, the upstream and the downstream lines, as in Figure 3.2B. The simulant gas was passed over the upper surface of nanofiber mat along the upstream line with a flow rate of 50 cc/min. At the same time, N<sub>2</sub> carrier gas with a flow rate of 50 cc/min traveled along the downstream line and delivered the simulant gas, which was passed through the nanofiber mat (25.5 cm<sup>2</sup> of area and 91 μm of thickness) from the upstream line, to the TENAX-TA tube for 40 min. The captured gas (2,000 cc) was evaluated by thermal desorption gas chromatography with mass spectrometer (TD-GC-MS).

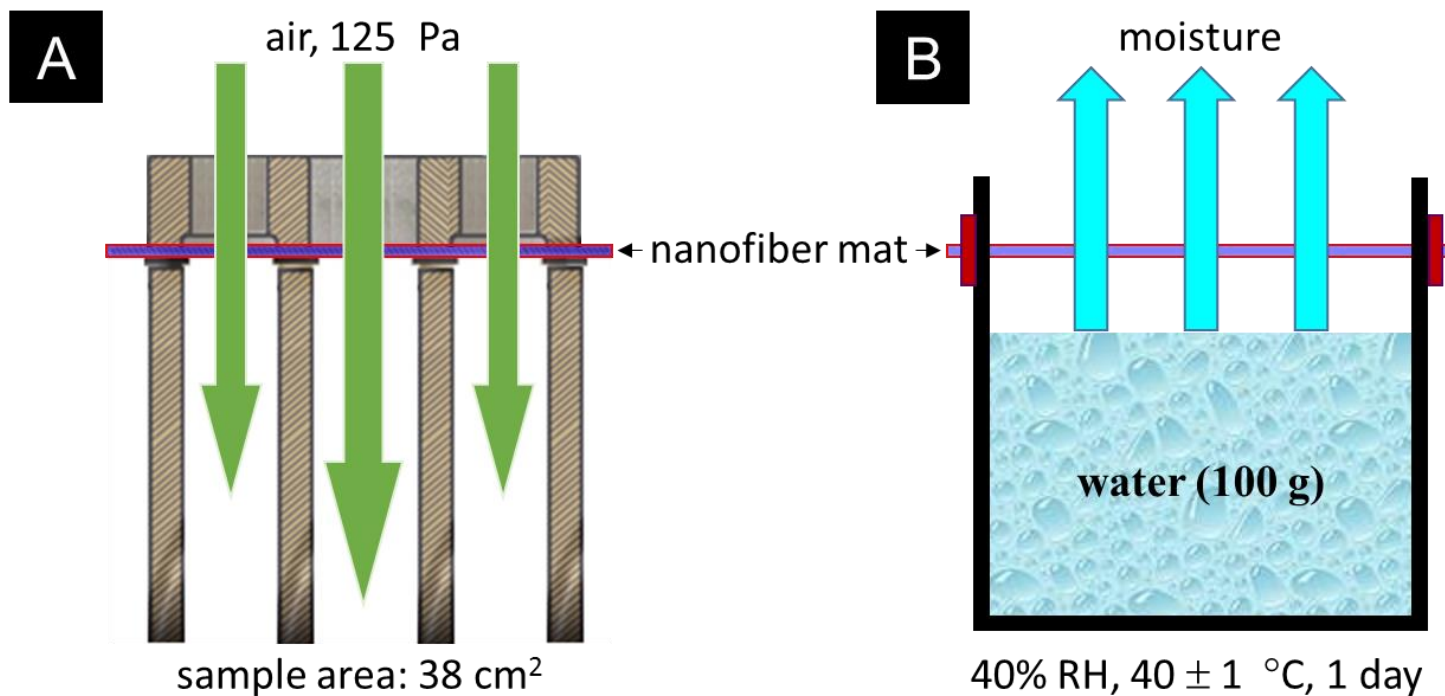


**Figure 3.2.** Schematic representations of experimental system for (A) air permeability (ASTM D737) and (B) water vapor permeability (ASTM E96).



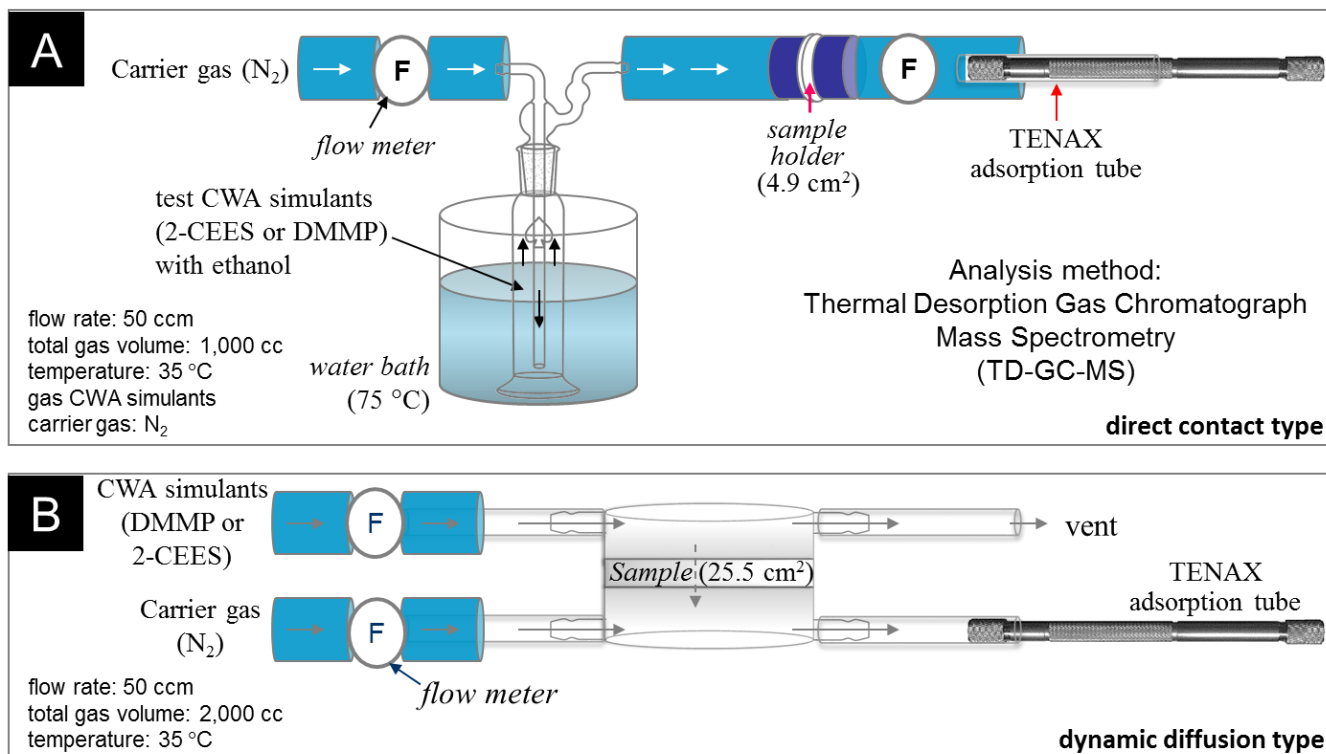


**Figure 3.3.** Schematic representations of experimental system to investigate the resistance of the nanofiber composites to permeation by gas CWA simulants: (A) direct contact type and (B) dynamic diffusion type.

### 3.3 Results and Discussion

#### 3.3.1 Adsorptivity of chemical warfare agent simulants on MgO and POM particles

In order to select the adsorbents to be incorporated in the nanofiber composites for nanofibrous inner layer of protective materials against gas CWA, the adsorptivity of 2-chloroethyl ethyl sulfide (2-CEES) and dimethyl methyl phosphonate (DMMP) on the 7 types of commercial magnesium oxide (MgO, light and heavy grade) and 3 types of polyoxometalate (POM) was investigated according to the ASTM D5160-95 method. As shown in Table 3.1, MgO candidates showed low adsorptivity of 2-CEES (lower than 0.32  $\mu\text{g/g}$ ) at room temperature, but showed moderate adsorptivity of DMMP (0.47–0.93  $\mu\text{g/g}$ ). In contrast, POM species, ammonium (*para*)tungstate hydrate and ammonium phosphomolybdate hydrate, showed relatively higher adsorptivity of 2-CEES (0.57–0.72  $\mu\text{g/g}$ ) and moderated adsorptivity of DMMP (0.72–0.87  $\mu\text{g/g}$ ). In addition, it was checked that the processability of the MgO and POM particles for electrospray, only ammonium (*para*)tungstate hydrate could not dispersed in the solvent, such as methanol, for electrospray. Other candidates well dispersed in methanol, so they could be incorporated in nanofiber composites using electrospray process. Also, the high adsorption efficiency against CWA simulants and electrosprayability about the various MgO and POM candidates

were considered. Finally, MgO, fine white powder of –325 mesh by Sigma-Aldrich, and ammonium phosphomolybdate hydrate, fine yellow powder produced by Kanto were selected the adsorbents to incorporate in the nanofibrous protective materials against CWA.

**Table 3.1.** Chemical warfare agent simulants (2-CEES and DMMP) adsorptivity of MgO and POM particles

Magnesium oxide (MgO)	<b>–325 mesh</b>	< 50 nm	Light	Heavy	Light	Heavy	Light
Maker	<b>Sigma Aldrich</b>		Daejung		Junsei		Wako
2-CEES absorptivity (µg/g) (%)	<b>0.22</b> <b>(28.8)</b>	0.18 (23.1)	0.30 (38.2)	0.32 (41.7)	0.24 (31.2)	0.13 (17.5)	0.26 (33.3)
DMMP absorptivity (µg/g) (%)	<b>0.93</b> <b>(78.3)</b>	0.82 (68.5)	0.64 (53.4)	0.61 (51.2)	0.78 (65.6)	0.47 (39.3)	0.54 (45.6)
Suitability of electrospray	<b>yes</b>	yes	yes	yes	yes	yes	yes

Polyoxometalate (POM)	Ammonium (para)tungstate hydrate (NH <sub>4</sub> ) <sub>10</sub> (H <sub>2</sub> W <sub>12</sub> O <sub>42</sub> )·4H <sub>2</sub> O	Ammonium phosphomolybdate hydrate (NH <sub>4</sub> ) <sub>3</sub> PMo <sub>12</sub> O <sub>40</sub> ·nH <sub>2</sub> O	
Maker	Sigma Aldrich	Daejung	Kanto
2-CEES absorptivity (µg/g) (%)	0.61 (79.8)	0.57 (74.0)	<b>0.72</b> <b>(93.7)</b>
DMMP absorptivity (µg/g) (%)	0.72 (60.7)	0.79 (66.4)	<b>0.87</b> <b>(73.0)</b>
Suitability of electrospray	no	yes	<b>yes</b>

### **3.3.2 Nanofibrous inner layer for adsorptive protection against chemical warfare simulants**

Prior to preparation of the nanofiber composites, the optimum electrospinning conditions of polyamide nanofibers (PANF) were determined. The concentration of solution affects the evaporation of solvent during electrospinning. Applied voltage and tip-to-collector distance affect the strength of electric field that stretches the polymer jet into nanofiber. Also the tip-to-collector distance influences the stretching duration and traveling distance of the polymer jet. Flow rate of the solution is closely connected with the volume of solution applied to the Taylor cone, and it influences the nanofiber morphology. The optimum conditions of electrospinning were selected based on considerations such as the following: (i) the morphology of the nanofiber observed by field-emission scanning electron microscopy (FE-SEM); (ii) the shape and stability of the Taylor cone confirmed visually during electrospinning; and (iii) the applicability to the SEE process. It was decided that the optimum electrospinning conditions of nanofibers with no defect as follows: 15 % (w/v) solution concentration; 15-25 kV of positive DC voltage; -5 kV of negative DC voltage; 9 cm of TCD; and 1.0 mL/h of flow rate. At the same time, the adsorbents were incorporated onto the nanofiber surface with fine dispersion as follows: using methanol solvent; -5 kV of negative DC voltage; 12 kV of positive DC voltage; 10 cm of tip-to-collector distance; and

10 mL/h of flow rate. In the case of electrospray for the MgO and POM, the optimum conditions were selected based on considerations with fine dispersion of the adsorbents onto the nanofiber surface as follows: using methanol solvent; 12 kV of positive DC voltage; -5 kV of negative DC voltage; 10 cm of tip-to-collector distance; and 1.5 mL/h of flow rate. The as-prepared MgO/PANF and POM/PANF nanofiber composites were annealed at 80 °C for 30 min so as to adhere the adsorbents on the nanofiber surface, and then thoroughly washed to remove the salt and any unbound adsorbents from the nanofibers. Finally, the nanofiber composites for inner layer of protective materials ([I]MgO/PANF and [I]POM/PANF) were stored in a vacuum desiccator.

The morphology of the nanofibers was observed by FE-SEM: The pristine PANF showed the disordered nature, a continuous shape without defects such as beads, and a smooth surface with uniform diameter of  $163 \pm 21$  nm (data not shown), however, the nanofiber composites displayed the electrosprayed adsorbents (MgO and POM) on and between the nanofibers without the formation of large aggregates as in Figure 3.4. The uniform morphology and the disordering array of nanofibers was preserved in spite of incorporating the adsorbents by electrospray. The content of the adsorbents onto the PANF by control of electrospinning and electrospray conditions such as concentration and flow rate. In order to determine the thermal property of nanofiber composites and the content of adsorbents, thermal gravimetric analysis (TGA)

was conducted in nitrogen at a heating rate of 10 °C/min. As shown in Figure 3.5, neat PANF showed the  $T_{d10}$  around 370 °C and dramatic weight loss around 400 °C. Also the nanofiber composites ([I]MgO/PANF and [I]POM/PANF, which have the adsorbents of 18.1 and 16.4 wt%, respectively) showed similar thermal degradation behavior compared to the neat PANF. It indicates that the adsorbents located on the surface of nanofibers were little affected the thermal behavior of nanofibers.

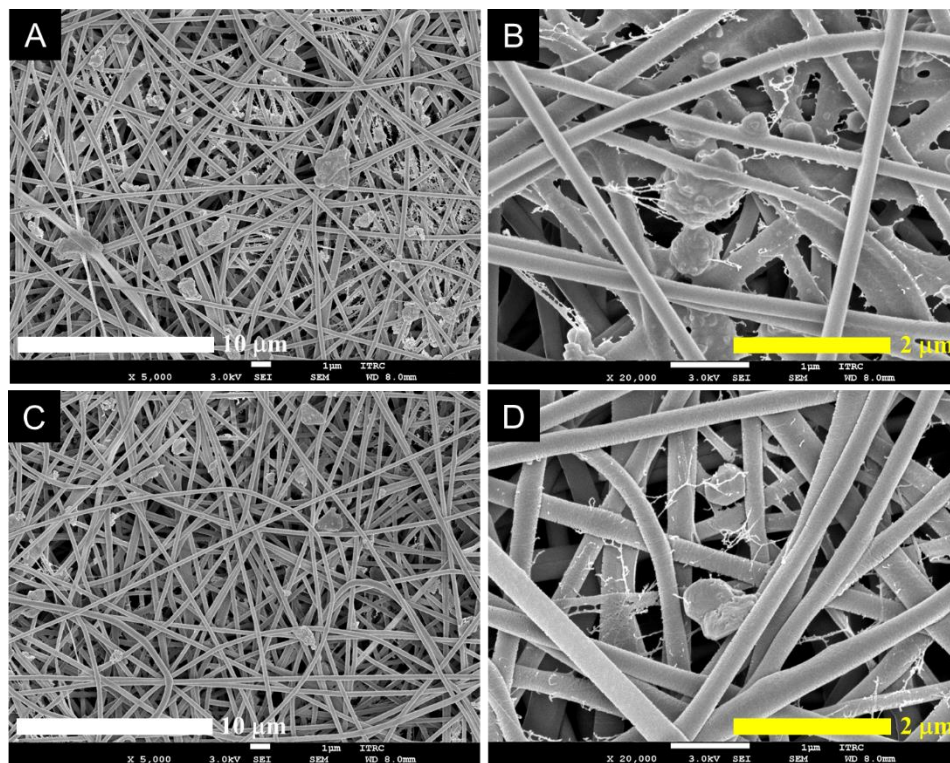


**Figure 3.4.** Morphology of (A and B) the [I]MgO/PANF and (C and D) the [I]POM/PANF nanofiber composites for outer layers of nanofibrous protective materials.



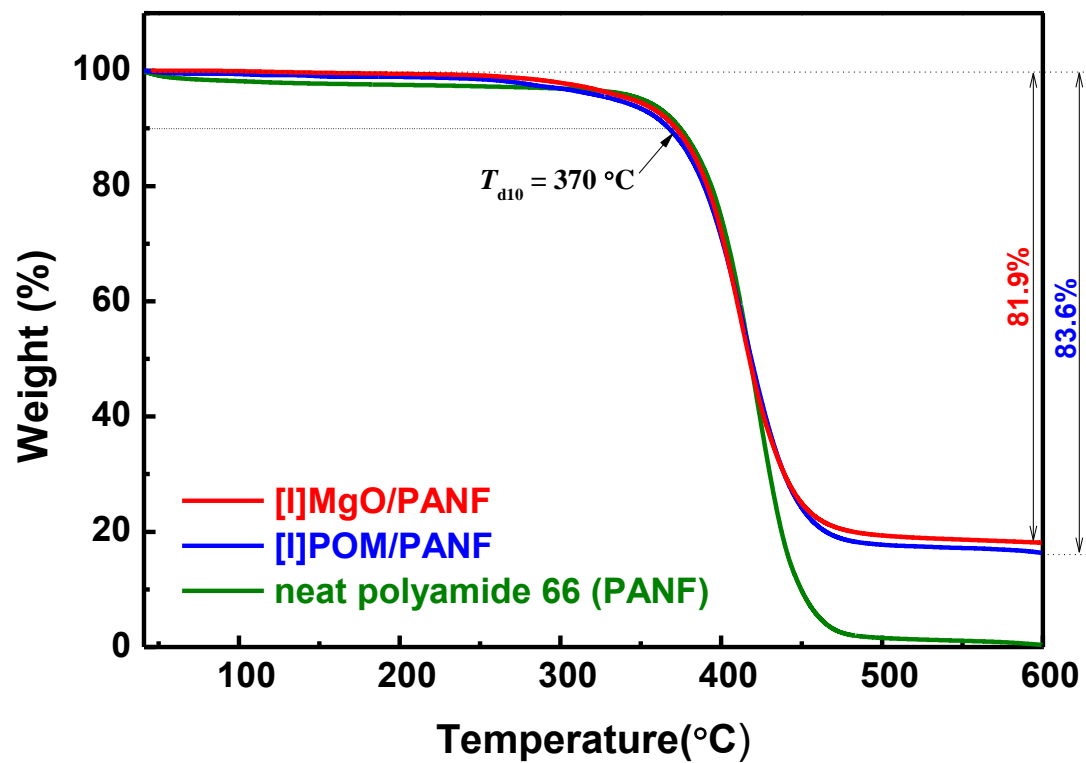


**Figure 3.5.** Thermal degradation behavior (TGA) of the neat polyamide nanofiber (PANF) and nanofiber composites ([I]MgO/PANF and [I]POM/PANF).

Tensile test was conducted to determine the mechanical properties of the nanofiber composites. As shown in Table 3.2, the surface-incorporated adsorbents did little affect to the mechanical properties, such as the Young's modulus, tensile stress and tensile strain. Unlike the ordinary composite with contained fillers inside nanofibers, the adsorbents located on the surface of nanofibers did not contribute to the enhancement of mechanical properties. In contrary, the adsorbents, which were held on the nanofiber surface, had an effect on the flow pore diameter and pore size distribute of the nanofiber mats. The flow pore diameter was characterized by liquid extrusion flow porometry (capillary flow porometry). During examination of capillary flow porometer, the pores of nanofiber mats were spontaneously filled with a wetting liquid and the liquid was extruded from pores by a non-reacting gas, such as N<sub>2</sub>. It can be shown that the differential pressure is related to pore diameter,<sup>24,25</sup> and it is illustrated in Figure 3.5 schematically.

$$D = 4\gamma\cos\theta/p$$

where  $D$  is flow pore diameter,  $\gamma$  is surface tension of wetting liquid,  $\theta$  is the contact angle of the wetting liquid and  $p$  is differential pressure. The pores of the nanofiber mat were filled with a wetting liquid, the liquid was emptied by a pressurized N<sub>2</sub> gas permitting gas to flow through the empty pores. The differential pressure required to empty a pore of diameter  $D$  is given by the equation.<sup>26,27</sup> The largest pore was emptied at the lowest pressure and initiated

N<sub>2</sub> flow. With increasing pressure smaller pores were emptied and N<sub>2</sub> flow increases. Then, the differential pressures and gas flow rates through the dry and wet nanofiber mats were measured. In the dry case, the flow rate increases with increase in pressure. However, in the wet case, initially there was no N<sub>2</sub> flow because all the pores are filled with the liquid. At a certain pressure the N<sub>2</sub> gas empties the largest pore (bubble point, see the ① mark in Figure 3.6) and gas flow starts through the wet nanofiber mat. With further increase in pressure smaller pores are emptied and the flow rate increases until all the pores are empty and the flow rate through the wet nanofiber mat is the same as that through the dry sample. It indicates the smallest pore (see the ② mark in Figure 3.6). The half-dry curve in this figure is computed from the dry curve to yield fifty-percent of flow through dry sample at the same pressure. The dry and wet curves yield the bubble point, the mean flow pore diameter, flow distribution and pore fraction distribution of through pores. Using this capillary flow porometry, the flow pore characteristics of neat PANF and the nanofiber composite ([I]MgO/PANF) was observed. All things considered, the adsorbents, which were held on the nanofiber surface, had an effect on the decrease of the mean flow pore diameter compared to the neat PANF (from 0.150  $\mu\text{m}$  to 0.139  $\mu\text{m}$ ). Also, the pore volume was decreased (see Figure 3.6C and 3.6D). These reduced flow pore diameter influenced the decrease of air permeability as shown in Table 3.3. However, in the case of water vapor

transmission rate, the nanofiber composites ([I]MgO/PANF and [I]POM/PANF) showed similar water vapor permeability compared to the neat PANF, and also they exhibited the superior moisture permeability compared to the inner layer of permeable protective clothing of Korea Army ( $3,623 \pm 79 \text{ g/m}^2/\text{day}$ ), which employed hydrophobic activated carbon adsorbents. These results indicate that the decrease of flow pore diameter can more influence the air-permeability than the water vapor permeability of the nanofiber composites. Also, the nanofiber composites are expected to being able to improve the problem of moisture retention for the currently applied protective clothing for Korea Army.

**Table 3.2.** Mechanical properties of pristine polyamide 66 nanofiber (PANF) and nanofiber composites ([I]MgO/PANF and [I]POM/PANF)

	Modulus (N/mm <sup>2</sup> )	Tensile stress at yield (MPa)	Tensile strain at yield (%)	Tensile stress at break (MPa)	Tensile strain at break (%)
PANF	209.51 ± 13.73	5.23 ± 0.20	2.45 ± 0.18	25.47 ± 1.07	42.10 ± 1.74
[I]MgO/PANF	253.07 ± 21.42	6.52 ± 0.04	2.09 ± 0.25	24.62 ± 1.95	36.09 ± 1.86
[I]POM/PANF	228.94 ± 19.54	4.64 ± 0.01	2.10 ± 0.01	18.86 ± 0.97	41.79 ± 1.54

Universal Testing Machine, strain-rate: 5 mm/min under ambient condition.

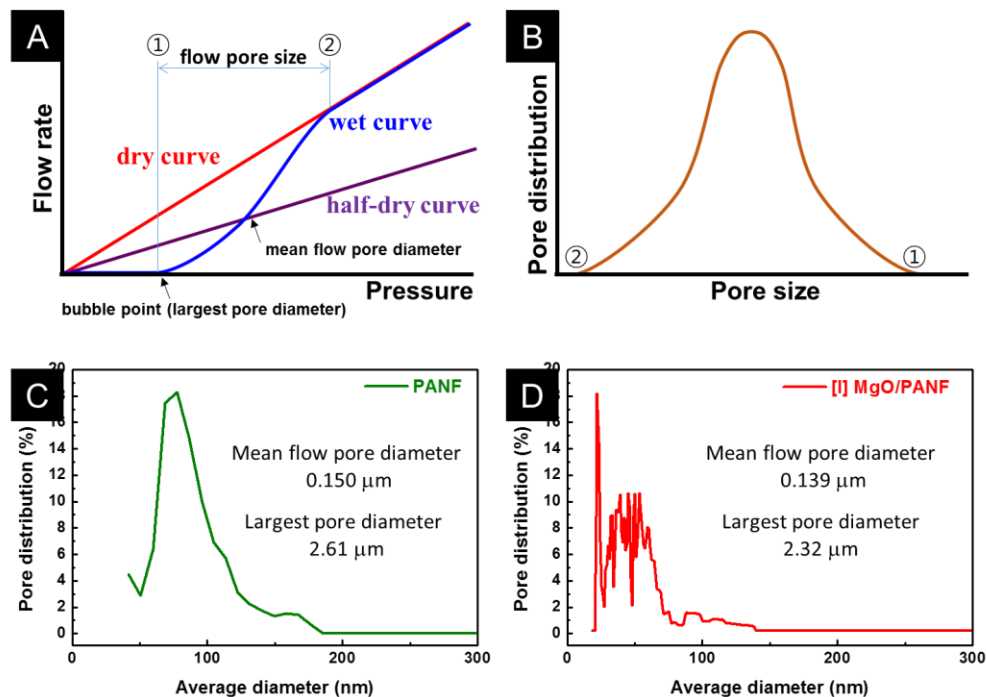


**Figure 3.6.** Theoretical profiles of flow pore characteristics measured by capillary flow porometry: (A) dry and wet curves indicating range of flow pore size and (B) pore size distribution. Practical profiles of flow pore characteristics of the nanofiber mats: (C) neat polyamide 66 nanofiber (PANF) and (D) [I]MgO/PANF.

**Table 3.3.** Air permeability and water vapor transmittance rate of the nanofiber mats

	Neat PANF	[I]MgO/PANF	[I]POM/PANF
Air permeability* (cfm)	$0.740 \pm 0.008$	$0.706 \pm 0.004$	$0.661 \pm 0.020$
Water vapor transmission rate** (g/m <sup>2</sup> /day)	$4,863 \pm 101$	$4,575 \pm 35$	$4,722 \pm 52$

\* ASTM D737, test pressure 125 Pa, test area 38 cm<sup>2</sup>

\*\* ASTM E96, 40% RH, 40 ± 1 °C

In order to investigate the resistance of the nanofiber composites to permeation by gas chemical warfare agent (CWA), the two types of permeation test was conducted using the simulants (2-CEES and DMMP). Table 3.4 shows the results of permeation test for relative amount of the penetrated simulants through the neat PANF and nanofiber composites. [I]MgO/PANF and [I]POM/PANF showed a little bit of better performance compared to PANF, but it was ineffective to protect from the CWA. Only 1 sheet of the nanofiber composite (91  $\mu\text{m}$  thickness) was ineffective to absorb the passing simulant gas. On closer scrutiny, in the case of direct contact type experiment, the simulants gas passed directly through the nanofiber mat, and so the captured amount of simulants was larger compared to the dynamic diffusion type regardless of low amount of the passed simulant gas (1,000 cc vs. 2,000 cc). In addition, 2-CEES showed higher penetration amount into the nanofiber mats compared to DMMP, it was attributed to higher volatility of 2-CEES. In conclusion, only 1 layer (thickness of 91  $\mu\text{m}$ ) of the nanofiber composite was ineffective and difficult to protect from the CWA. So it was planned that the several inner layers of the nanofiber composites were applied to achieve an acceptable protective ability against chemical warfare simulants. The protective ability of a pile of the layers will discuss in chapter 5.



**Table 3.4.** Permeation test of the simulant of chemical warfare agents through the nanofiber mats

Direct contact type *				
CWA simulants	blank	Neat PANF	[I]MgO/PANF	[I]POM/PANF
2-CEES ( $\mu\text{g}/\text{m}^3$ )	40.14 / 100%	25.88 / 64.5%	12.97 / 32.3%	10.65 / 26.5%
DMMP ( $\mu\text{g}/\text{m}^3$ )	62.76 / 100%	17.96 / 28.6%	5.76 / 9.2%	4.99 / 7.8%

Dynamic diffusion type **				
CWA simulants	blank	Neat PANF	[I]MgO/PANF	[I]POM/PANF
2-CEES ( $\mu\text{g}/\text{m}^3$ )	30.96 / 100%	6.56 / 21.2%	2.56 / 8.3%	2.02 / 6.5%
DMMP ( $\mu\text{g}/\text{m}^3$ )	37.76 / 100%	6.68 / 17.7%	4.80 / 12.7%	2.64 / 7.0%

\* flow rate: 50 ccm, total gas volume: 1,000 cc, temperature: 36 °C, carrier gas: N<sub>2</sub>

\*\* flow rate: 50 ccm, total gas volume: 2,000 cc, temperature: 25 °C, carrier gas: N<sub>2</sub>

### **3.4 Summary**

This study described the development of the nanofiber composite containing adsorbents for inner layer of permeable protective clothing against chemical warfare agents (CWA). To achieve this, polyamide nanofibers (PANF) was prepared using electrospinning and put MgO/POM down on the nanofiber surface using electrospinning at the same time (simultaneous electrospinning/electrospraying process). The adsorbents, which were held on the nanofiber surface, had an effect on the decrease of the mean flow pore diameter compared to the neat PANF. In addition, the nanofiber composites exhibited the superior moisture permeability compared to the inner layer of permeable protective clothing of Korea Army. These findings reveals that the nanofiber composites are expected to being able to improve the problem of moisture retention. In the case of the CWA permeability, the nanofiber composites showed a better protectability than that of neat polyamide nanofiber mat, but the use of just one sheet was inadequate to protect from the CWA.

## References

1. *NATO Handbook on the Medical Aspects of NBC Defensive Operations*; Department of the Army; Washington, DC: HQ, DA; AMedP-6, Part 3; **1996**, 1-1. Field Manual 8-9.
2. Szinicz, L. *Toxicology* **2005**, 214, 167.
3. Dickson, E. F. G. *J. Toxicol. Env. Health Part A* **2008**, 71, 1382.
4. Gao, P.; King, W. P.; Shaffer, R. J. *Occup. Environ. Hyg.* **2007**, 4, 562.
5. Pal, T.; Griffin, G. D.; Miller, G. H.; Watson, A. P.; Daugherty, M. L.; Vodinh, T. *J. Hazard. Mater.* **1993**, 33, 123.
6. Liu, D. K.; Wannemacher, R. W.; Snider, T. H.; Hayes, T. L. *J. Appl. Toxicol.* **1999**, 17, S41.
7. *Military Textiles*; Wilusz, E. Ed.; Woodhead Publishing Limited: England, **2008**.
8. Sundarrajan, S.; Ramakrishna, S. *J. Mater. Sci.* **2007**, 42, 8400.
9. Wagner, G. W.; Bartram, P. W.; Koper, O.; Klabunde, K. J. *J. Phys. Chem. B* **1999**, 103, 3225.
10. Mahato, T. H.; Prasad, G. K.; Singh, B.; Batra, K.; Ganesan, K. *Microporous Mesoporous Mat.* **2010**, 132, 15.
11. Mahato, T. H.; Prasad, G. K.; Singh, B.; Acharya, J.; Srivastava, A. R.; Vijayaraghavan R. *J. Hazard. Mater.* **2009**, 165, 928.
12. Prasad, G.K.; Mahato, T.H.; Singh, B.; Ganesan, K.; Pandey, P. and Sekhar, K. *J. Hazard. Mater.* **2007**, 149, 460.
13. Panayotov, D. A.; Morris, J. R. *J. Phys. Chem. C* **2009**, 113, 15684.
14. Ramaseshan, R.; Ramakrishna, S. *J. Am. Ceram. Soc.* **2007**, 90, 1836.
15. Neațu, Ș; Pârvulescu, V.I.; Epure, G.; Petrea, N.; Șomoghi, V.; Ricchiardi, G.; Bordiga, S.; Zecchina, A. *Appl. Catal. B-Environ.* **2009**, 91, 546.

16. Grandcolas, M.; Sinault, L.; Mosset, F.; Louvet, A.; Keller, N.; Kellera, V. *Appl. Catal. A-Gen.* **2011**, *391*, 455.
17. Cojocaru, B.; Neațu, Ș.; Pârvulescu, V. I.; Șomoghi, V.; Petrea, N.; Epure, G.; Alvaro, M.; Garcia, H. *ChemSusChem* **2009**, *2*, 427.
18. Neațu, Ș.; Cojocaru, B.; Pârvulescu, V. I.; Șomoghi, V.; Alvaro, M.; Garcia, H. *J. Mater. Chem.* **2010**, *20*, 4050.
19. Smith, B. M. *Chem. Soc. Rev.* **2008**, *37*, 470.
20. Koper, O.; Lucas, E.; Klabunde, K. J. *J. Appl. Toxicol.* **1999**, *19*, S59.
21. Ferguson-McPherson, M. K.; Low, E. R.; Esker, A. R.; Morris, J. R. *Langmuir* **2005**, *21*, 11226
22. Okun, N. M.; Tarr, J. C.; Hilleshiem, D. A.; Zhang, L.; Hardcastle K. I.; Hill, C. L. *J. Mol. Catal. A-Chem.*, **2006**, *246*, 11.
23. *ASTM D5160-95, Standard Guide for Gas-Phase Adsorption Testing of Activated Carbon*; American Society for Testing and Materials; ASTM International: West Conshohocken, PA, 2008.
24. *A Novel Technique for Pore Structure Characterization without the Use of Any Toxic Material*; Nondestructive Characterization of Materials XI; Jena, A.; Gupta, K.; Eds.; Springer: New York, USA, 2002, 813-821.
25. Jena, A.; Gupta, K. *Int. Nonwovens J.* **2003**, 45.
26. Jena, A.; Gupta, K. *Fluid/Part. Sep. J.* **2002**, *14*, 227.
27. Jena, A.; Gupta, K. *J. Power Sources* **1999**, *80*, 46.

## **Chapter 4**

# **Nanofibrous Outer Layer of Chemical Warfare Protective Materials with Repellency of Chemical Warfare Agents**

### **4.1 Introduction**

The outer layer of the permeable protective clothing against chemical warfare agents (CWA) has been developed to repel the liquid CWA which is trying to invade in the protective clothing. The outer layer has been required to have a high repellency against liquid CWA, mechanical property, chemical stability, air/moisture permeability and light weight. Among the various nanomaterials, the nanofiber should be a good candidate of the outer layer for the protective clothing materials because of the characteristics such as high porosity, high surface area, high permeability, low basis weight, and small fiber diameter.<sup>1</sup> Development of lightweight protective clothing composed of electrospun nanofibers for chemical and biological warfare protection was reported.<sup>2-4</sup> Electrospun nanofibers were applied to the chemical and biological warfare agent protective clothing. Various methods of modifying nanofiber surfaces to enhance their protectability and decontamination capability of warfare agents have been studied currently based on chemical surface modification and

attachment of reactive groups on the surface of nanofibers. In addition, functionalized nanofibers for protection from chemical warfare simulants are developed and evaluated based on the hydrolysis study.<sup>4</sup>

The aromatic polyamides, Aramids, are a class of strong, heat-resistant, and chemical stable polymer having repeating units containing phenyl rings linked together by amide groups. Phenyl rings prevent the rotating and twisting of polymer chains around their chemical bonds. Because amide groups form intermolecular hydrogen bonds networks, aramid has superior properties such as extremely high strength and high resistance to chemicals, heat and physical abrasion.<sup>5</sup> The best known aramids are *para*-aramid, such as poly(*p*-phenylene terephthalamide) (PPTA, Kevlar® and Twaron®), and *meta*-aramid, such as poly(*m*-phenylene isophthalamide) (PMIA, Nomex® and TeijinConex®).<sup>6</sup> *Para*-aramid has been made into a bulletproof materials because of excellent mechanical and thermal properties, but, their poor solubility and fusibility result in low processability and limit the formation of various nanostructures. In contrary, *meta*-aramid can soluble in organic solvent, such as *N,N*-dimethyl acetamide (DMAc), *N,N*-dimethyl formamide (DMF), *N,N*-dimethyl sulfoxide (DMSO), *N*-methyl-2-pyrrolidone (NMP), with certain salts such as LiCl and CaCl<sub>2</sub>.<sup>7</sup> Thus *meta*-aramid have high potential for efficient formation of various nanostructures.

Recently, the *meta*-aramids, such as Nomex, have been fabricated into

nanofibers by the electrospinning, which has emerged as a novel technique for producing uniform nanofibers due to its versatility, easy process, simple apparatus, and possibility of using various types of polymers in the melt or solution state. These *meta*-aramid nanofibers have been intensively studied as filtration media, protective materials and nanofibrous substrates for various applications. Lin *et al.* investigated the *meta*-aramid nanofibrous membranes for water purification.<sup>8</sup> Shin *et al.* reported the electrospun *meta*-aramid nanofibers as a composite filter for water/oil separation.<sup>9</sup> However, compared with commercial *meta*-aramid fibers, the mechanical properties of electrospun *meta*-aramid nanofibers could be insufficient because the polymer chains did not have a well-developed molecular orientation.

It was found that the electrospun *meta*-aramid nanofibers were extremely vulnerable to dipolar aprotic solvent like DMAc, DMF and DMSO. The main problem of their low chemical stability is the difficulty with which it can be applied. In order to develop the crystalline structure to compete with commercial *meta*-aramid fibers, there have been various post-treatments, such as washing, heat, and electromagnetic wave irradiation treatments. Yao *et al.* annealed electrospun *meta*-aramid nanofibers under 150, 200 and 250 °C for several days, but the heat treatment did not have the apparent effect.<sup>10</sup> Oh *et al.* reported that the removal of salts in *meta*-aramid nanofibers brought out the increasing of mechanical strength for the nanofibers, and unfortunately, the

results for control of crystalline structure were not discussed.<sup>11</sup> Kim *et al.* showed that the crystalline structure of salt removed *meta*-aramid nanofibers was regenerated by microwave irradiation under wet condition.<sup>12</sup>

Herein, electrospun *meta*-aramid nanofiber mats with enhanced chemical stability and mechanical property was developed using sequential post-treatment for removal of salt in the nanofiber and regeneration of crystalline structure. The aligned *meta*-aramid nanofiber mats with LiCl salt was prepared using electrospinning apparatus with drum-collector. The salt-removed nanofiber mat showed a glass transition temperature ( $T_g$ ) at 272 °C, which was not observed in the pristine electrospun nanofiber mat, and these results mean that existence of salt between *meta*-aramid chains interrupted the rearrangement of the chains. The washing and heating sequential post-treated nanofiber mats above  $T_g$  for 20 min showed improved chemicals stability, which was confirmed by survival of the heat-treated nanofiber mats in DMAc. In addition, the sequential post-treatment brought about the reappearance of characteristic diffracting peaks for (110) and (002) planes and the regeneration of hydrogen bonding between *meta*-aramid chains. These structural change derived from the post-treatment led to increase the Young's modulus of *meta*-aramid nanofiber mats. Furthermore, in order to estimate the possibility of their application to an outer layer for permeable protective clothing having the repellency against liquid CWA, the surface-modified *meta*-aramid nanofiber



mats were provided via treatment using water and oil repellent. Finally the nanofiber mats showed superhydrophobic and high oleophobic nature at the same time.

## 4.2 Experiments

### 4.2.1 Materials

Poly(*meta*-phenylene isophthalamide) (*meta*-Aramid; Nomex®) fiber was purchased from DuPont. *N,N*-dimethylacetamide (DMAc; anhydrous; 99.8%), lithium chloride (LiCl; ACS reagent;  $\geq 99\%$ ), and ethanol (ACS reagent; anhydrous; 99.8%) were purchased from Sigma-Aldrich. The *meta*-aramid and LiCl were dried at 120 °C for 24 h in a vacuum oven before use. Unidyne TG-5601 (water-based emulsion; 20–30% fluoroalkyl acrylate copolymer, 5% poly(oxyethylene) alkyl (C12–14) ether, 1–10% tripropylene glycol, 55–65% water and 5% others; weak cation; as water and oil repellent I) was purchased from Daikin. 1*H*,1*H*,2*H*,2*H*-perfluorooctyl trichlorosilane (97%; fluorinated alkyl silane, FAS; as water and oil repellent II) was purchased from Sigma-Aldrich. Toluene (anhydrous; 99.8%), Commercial magnesium oxide (MgO; –325 mesh, Sigma-Aldrich) and ammonium phosphomolybdate hydrate ((NH<sub>4</sub>)<sub>3</sub>PMo<sub>12</sub>O<sub>40</sub>·*n*H<sub>2</sub>O; a kind of polyoxometalate; Kanto) were chosen as adsorbents of the CWA simulants and the detail description was listed in Table 3.1 in chapter 3. All samples were stored ambient condition before an adsorption test. 2-chloroethyl ethyl sulfide (2-CEES; 98% GC purity, Sigma-Aldrich) and dimethyl methyl phosphonate (DMMP, 97% GC purity, Sigma-Aldrich) were chosen as CWA simulants of mustard (HD) and Sarin (GB),

respectively. All of the materials were used as received without further purification.

#### **4.2.2 Optimization of preparation condition for *meta*-aramid nanofiber mat with improved chemical stability and mechanical property**

In order to prepare the electrospun Nomex nanofiber, the electrospinning solution was prepared as follows: 8.0 g of *meta*-aramid fiber was dissolved in 50 mL of DMAc solution containing 3.2 g of LiCl as a salt (4:10 weight ratio of LiCl/*meta*-aramid) at 50 °C for 24 h in an oven shaker (BF-30SI, BioFree, Korea). The pristine *meta*-aramid nanofiber mat (*m*ANF) was prepared by electrospinning: the solution was filled in a syringe having a stainless-steel needle with an internal diameter of 0.33 mm, the solution was transferred at a flow rate of 0.2 mL/h for 50 h. The needle tip of syringe was directly charged by 20–25 kV positive voltage. The syringe was placed horizontally from Al-foil covered drum collector rotating at 100 rpm. The collector was charged with –5 kV negative voltage. The tip-to-collector distance was 15 cm. The electrospinning process was conducted at  $23 \pm 1$  °C and  $50 \pm 4$  RH% condition. The experimental scheme to optimize the preparation condition of the Nomex nanofiber mat with improved chemical stability and mechanical property is

shown in Figure 4.1. In order to improve the chemical stability and mechanical property of Nomex nanofiber mats, the LiCl salt being in the Nomex was removed by washing treatment. The Nomex, fixed in a stainless frame, was soaked into the deionized water and mildly shaken for 30 min. This procedure was repeated three times. The washed Nomex nanofiber (*W-mANF*) was dried under ambient condition for 12 h and in vacuum oven for 12 h. The surface morphology of *mANF* and *W-mANF* was observed by field emission scanning electron microscopy (FE-SEM, JSM-6335F; JEOL). The removal of salt in the nanofibers was determined using energy-dispersive X-ray spectroscopy (EDS, XFlash 4000; Bruker AXS). Thermal behavior of *mANF* and *W-mANF* was observed using simultaneous differential thermal analysis/thermal gravimetric analysis (DTA/TGA) analyzer (SDT 2960; TA Instruments, heating rate 10 °C/min, temperature range from 40 to 700 °C, N<sub>2</sub> atmosphere) and differential scanning calorimetry (DSC, Q1000; TA Instruments, heating rate 10 °C/min, temperature range from 30 to 375 °C). The *W-mANF* was heat-treated at 250 and 300 °C for 20 min in a processing oven (UF 110, Memmert, Germany) so as to enhance chemical stability and mechanical property of *meta*-aramid nanofiber mats (HT250-*W-mANF* and HT300-*W-mANF*). In addition, *mANF* (an unwashed sample) was heat-treated at 300 °C for 20 min in the processing oven (HT300-un*W-mANF*). The chemical structure of nanofiber mats was observed using attenuated total

reflection/Fourier transform infrared (ATR/FT-IR, Nicolet iS5 with iD5 ZnSe ATR accessory, Thermo Scientific) spectroscopic system at room temperature (RT) over a range of 4000–650  $\text{cm}^{-1}$ . The crystalline structure of the nanofiber mats was investigated by wide angle X-ray Diffractometer (WXR, New D8 Advance, Bruker) with  $\text{Cu } K_{\alpha}$  radiation ( $\lambda = 1.541 \text{ \AA}$ ) at RT, a voltage of 40 kV, a current of 40 mA and a Bragg angles ( $2\theta$ ) from 10 to  $50^{\circ}$  with scan rate of  $2^{\circ}/\text{min}$ . The improved chemical stability was confirmed by checking whether the nanofiber mats survived in DMAc for 24 h. The mechanical property of the nanofiber mats was measured with a universal testing machine (UTM, Model 5567; INSTRON). Specimens were prepared with the form of standard dog-bone shapes with 3.00 mm width and 0.10–0.20 mm thickness according to ASTM D638 Type V. The specimens were tested in an aligned direction and a perpendicular direction to the alignment of nanofiber mats at a crosshead speed of 1 mm/min.

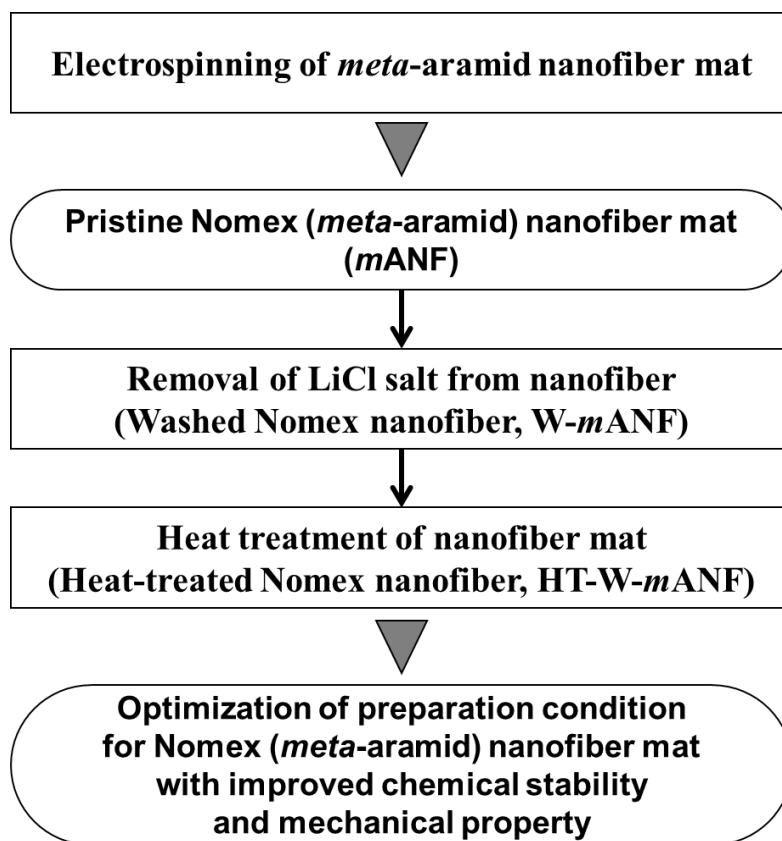


**Figure 4.1.** Experimental scheme of preparing the Nomex (*meta*-aramid) nanofiber mat with improved chemical stability and mechanical property.

#### **4.2.3 Nanofibrous outer layer for repellent protection against chemical warfare agent simulants**

The nanofiber composite for outer layer, consisted with Nomex nanofiber and the selected adsorbent (MgO or POM), was prepared using simultaneous electrospinning/electrospraying (SEE) process (Figure 2.1C and Figure 4.2). The SEE apparatus was constructed with a rotating drum collector, two positive DC voltage supplies, one negative DC voltage supply, and two syringe pumps comprising housings with syringe retainers. These syringe pumps were placed on opposite sides with respect to the collector. In order to prepare the electrospinning solution, 8 g of commercial Nomex fiber was dissolved in 50 mL of DMAc solution containing 1.6 g of LiCl as a salt (2:10 weight ratio of LiCl/Nomex) at 50 °C for 24 h in an oven shaker (BF-30SI, BioFree, Korea). The pristine *meta*-aramid nanofiber (*m*ANF) was prepared by electrospinning: the solution was filled in a syringe having a stainless-steel needle with an internal diameter of 0.33 mm, the solution was transferred at a flow rate of 0.15 mL/h for 68 h. The needle tip of syringe was directly charged by 20–25 kV positive voltage. The syringe was placed horizontally from Al-foil covered drum collector rotating at 100 rpm. The collector was charged with –5 kV negative voltage, and the tip-to-collector distance was 15 cm. The electrospinning process was conducted at  $23 \pm 1$  °C and  $45 \pm 5$  RH% condition.

At the same time, for the electrospray to introduce the adsorbents on the surface of *m*ANF, 1 g of the adsorbents (MgO or POM) was dispersed in 100 mL methanol using a horn-type ultrasonicator (VCX-750, Sonics & Materials, CT, USA) for 30 min. The dispersion was then electrosprayed using the following conditions: 0.51-mm inner diameter stainless steel spinneret, 12 kV at spinneret, 10 cm tip-to-collector distance, and solution flow rate of 1.5 mL/h for 68 h. The as-prepared MgO/*m*ANF and POM/*m*ANF composites were fixed in a stainless frame, respectively. The composites were soaked into the deionized water and mildly shaken for 1 h to remove the LiCl salt in the Nomex nanofibers and to wash out any unbound adsorbents from the nanofibers, and then heat-treated at 300 °C (above glass transition temperature of neat *m*ANF) for 10 min under air condition in a processing oven (UF 110, Memmert, Germany) for enhancement of chemical stability and mechanical property. The heat-treated nanofiber mats were surface-modified by two kinds of repellents, which were the fluorinated water and oil repellent, for high repellency against liquid CWA. The repellent I was Unidyne TG-5601, which was water-based emulsion containing 20–30% fluoroalkyl acrylate copolymer. The heat-treated nanofiber composite was immersed into a glass container with 200 mL of the repellent I solution for 10 min, and then dried and stabilized for 10 min in air. The repellent II was 1*H*,1*H*,2*H*,2*H*-perfluorooctyl trichlorosilane, a kind of fluorinated alkyl silane (FAS). The heat-treated nanofiber composite was



fixed in a stainless frame, and then it was immersed into a glass container with 50 mL of anhydrous toluene, and 50  $\mu$ L of 1*H*,1*H*,2*H*,2*H*-perfluorooctyl trichlorosilane (FAS) was added immediately to the solvent for surface silanization of the nanofiber mat (0.1 % V/V FAS/toluene). The glass container, which was closed to the air during the reaction, was slowly shaken at RT for 1 h. After the reaction, the as-silanized nanofiber mat was rinsed three times with toluene to remove the physically adsorbed FAS molecules on the nanofiber, and rinsed three times with ethanol to remove the remained toluene and FAS on the nanofiber. Then, the nanofiber was stabilized for 10 min at RT in an ambient condition, and finally followed by heat-treatment for 20 min at 120 °C in the processing oven. This procedure was repeated five times. Finally, the nanofiber composites for outer layer ([O]MgO/*m*ANF and [O]POM/*m*ANF), which were still wet, were transferred into the processing oven and heat treated at 180 °C for 3 min.

The surface morphology of [O]MgO/*m*ANF and [O]POM/*m*ANF was observed by field emission scanning electron microscopy (FE-SEM, JSM-6335F; JEOL). The removal of salt in the nanofibers was determined using energy-dispersive X-ray spectroscopy (EDS, XFlash 4000; Bruker AXS). The content of the adsorbents (MgO and POM) and thermal behavior of the composites was observed using simultaneous differential thermal analysis/thermal gravimetric

analysis (DTA/TGA) analyzer (SDT 2960; TA Instruments, heating rate 10 °C/min, temperature range from 40 to 700 °C, N<sub>2</sub> atmosphere. The repellency of the CWA simulants was determined by measurement of the static water and oil contact angles (WCA and OCA), which were observed using contact angle measurement (Theta Lite; Attension; KSV Instruments) with manually controlled HAMILTON syringe. Apparent contact angle of water and simulant drops were measured under air at  $25 \pm 1$  °C. The droplet with  $3.0 \pm 0.2$  µl was controlled by checking the droplet size, and formed on the surface of the nanofiber mats. Average WCA and OCA results, which were measured on five different positions were for each specimen, were reported with standard deviations of  $\pm 2^\circ$ .

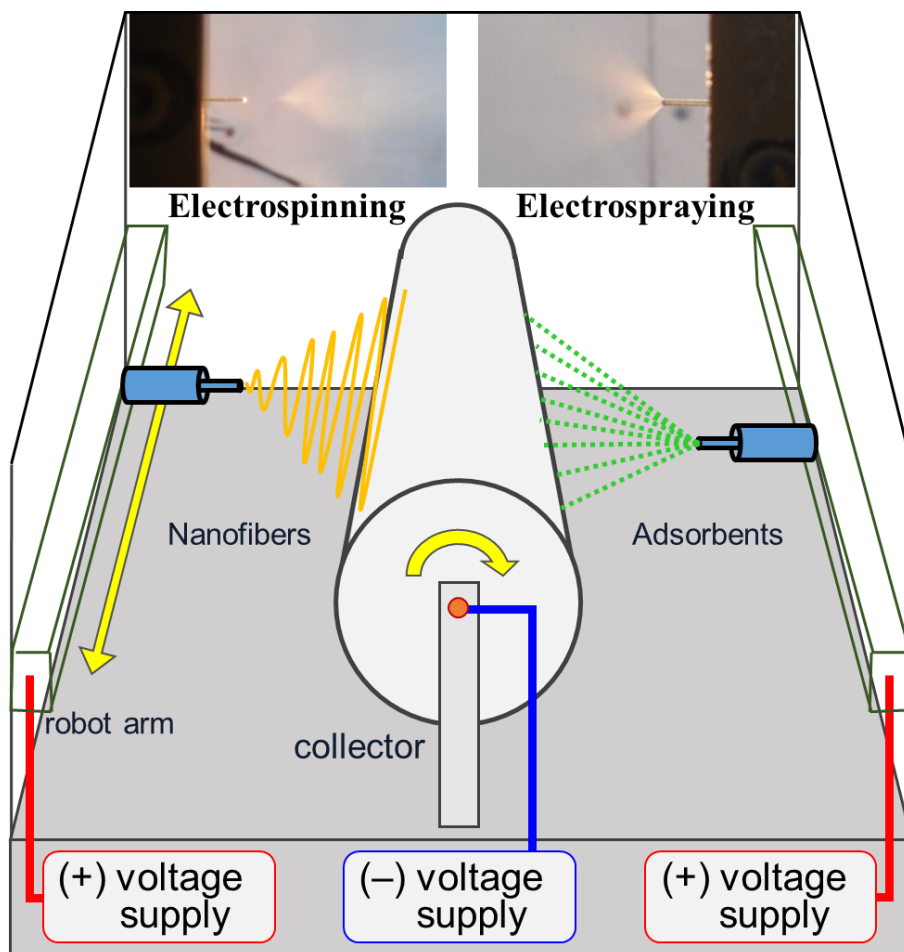


**Figure 4.2.** Schematic representation of the simultaneous electrospinning and electrospraying (SEE) process.

## 4.3 Results and Discussion

### 4.3.1 Optimization of preparation conditions for *meta*-aramid nanofiber mat with improved chemical stability and mechanical property

The *meta*-aramid (Nomex) solution for electrospinning was prepared using DMAc/LiCl solution system. The mechanism of dissolving Nomex in DMAc/LiCl solution is presented in Figure 4.3. The  $[\text{Li-DMAc}]^+$  complex ions were formed between DMAc and LiCl while the  $\text{Cl}^-$  ions were left freely. And then, the hydrogen bonds between *meta*-aramid chains can be broken by the free  $\text{Cl}^-$  ions, which interacts with the hydrogen on amide group. Therefore Nomex fiber can be dissolved in the solution. A suitable amount of LiCl for the dissolution of Nomex fiber was about 20–40 wt% compare to the fiber. The *meta*-aramid nanofiber mat (*mANF*) was efficiently prepared by electrospinning apparatus using drum-type collector. As shown in Figure 4.4A, the diameters of nanofibers were in the range *ca.* 200–300 nm, and the nanofibers had rough and uneven surface. In addition, the directional nature of nanofibers along the rotational direction of collector was observed. The analysis of the chemical composition of the nanofibers indicated that there was a considerable amount of Cl element in/on the nanofibers (Figure 4.4B). Li element was not detected because Be window of EDS detector absorbs low-

energy X-rays for light element. It was certain that the presence of the  $\text{Cl}^-$  in the nanofiber mat would have a negative impact on the chemical and physical properties of the nanofibers. Thus, the  $\text{Cl}^-$  being in the *m*ANF was removed by repetitive washing treatment with deionized water. As shown in Figure 4.4C, the washed *meta*-aramid nanofiber mat, which is called hereafter W-*m*ANF, retained a smooth surface with 200–300 nm in diameter. Furthermore, using element analysis, the Cl element in the *m*ANF was clearly removed during repetitive washing treatment (Figure 4.4D). The removal of  $\text{Cl}^-$  can affect the chemical and physical properties of the nanofibers. Thus, first of all, the thermal property of nanofiber mats was investigated.

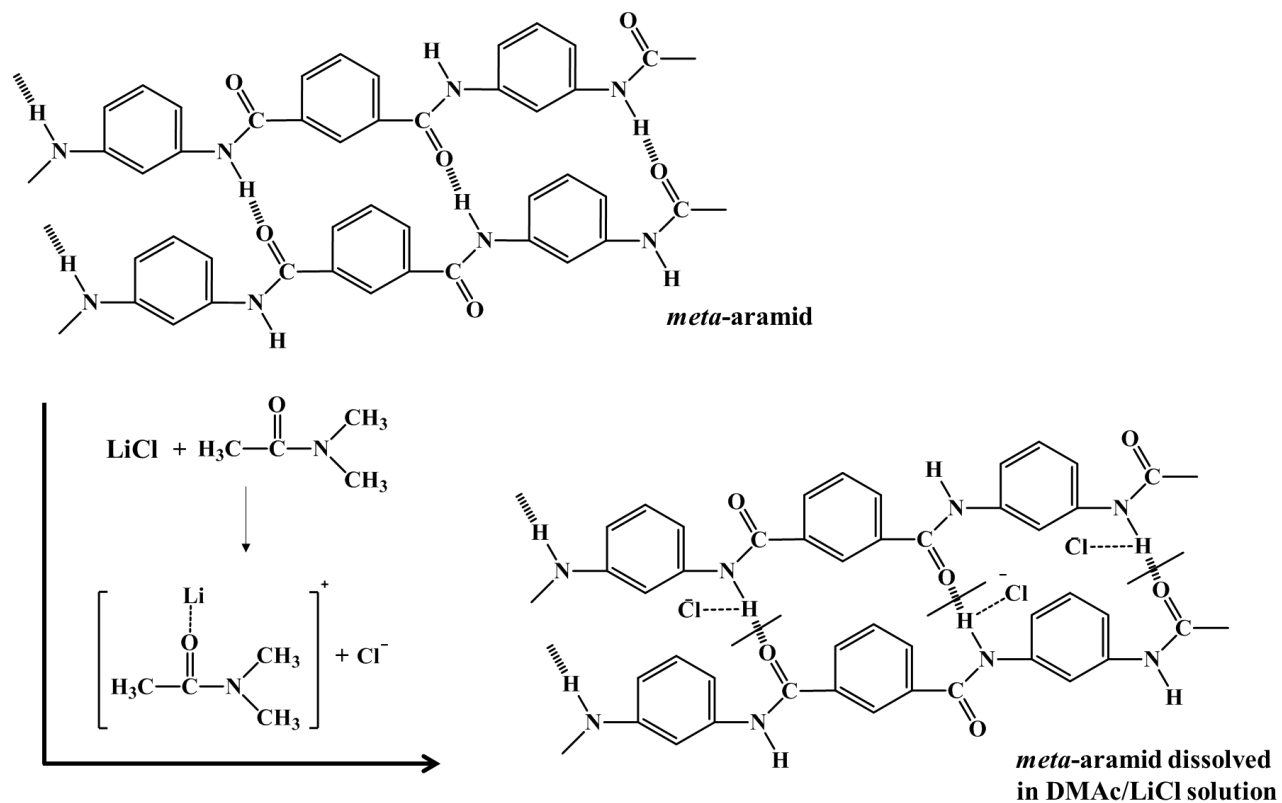


**Figure 4.3.** Dissolution mechanism of *meta*-aramid in DMAc/LiCl solution.

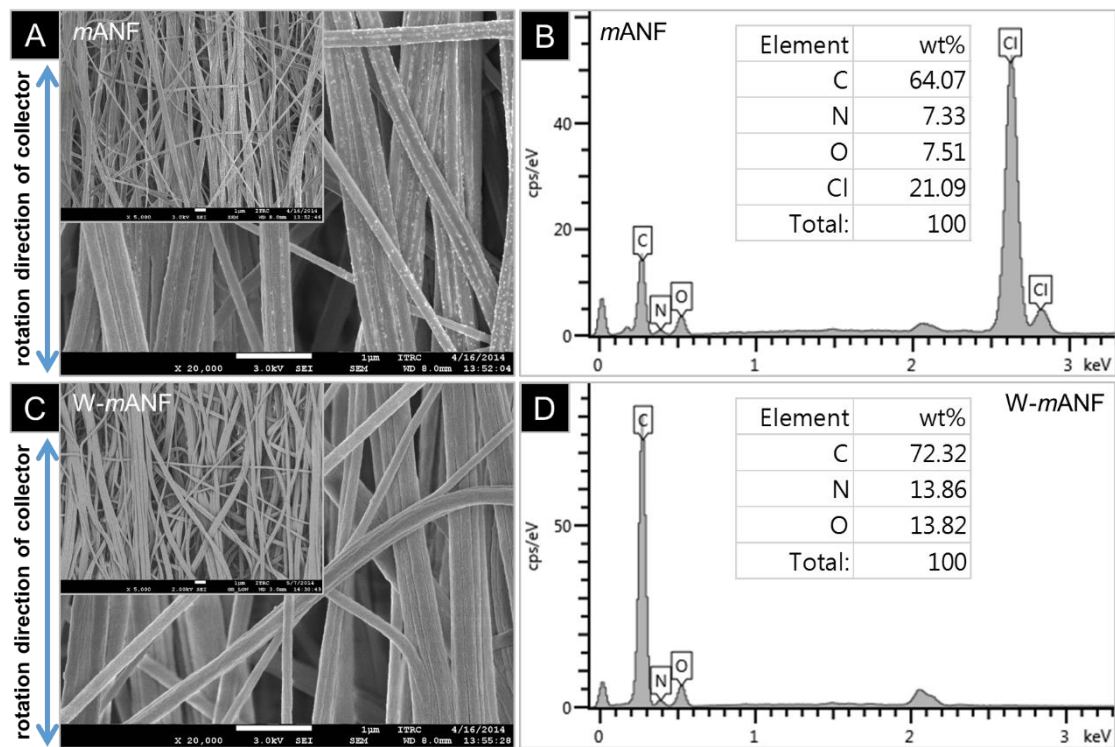


**Figure 4.4.** Morphology and elemental analysis of pristine *meta*-aramid nanofiber (mANF) (A and B) and washed mANF (LiCl removed) (W-mANF) (C and D).

TGA curves obtained during pyrolysis of *m*ANF and W-*m*ANF under N<sub>2</sub> atmosphere with a heating rate of 10 °C/min are shown in Figure 4.5A. There are two steps of weight loss in the temperature ranges approximately 40–100 and 400–650 °C. The first weight loss observed in the curve of W-*m*ANF, which spans from 40 to about 100 °C, is ascribable to the release of adsorbed moisture. This result is similar to that of the previous study about thermal degradation of Nomex fibers.<sup>13</sup> However, the *m*ANF presented the dramatic weight loss near 100 °C, which indicated that a considerable amount of moisture and Cl<sup>−</sup> had an escape from the *m*ANF in this temperature range. Another weight loss of *m*ANF and W-*m*ANF begins at approximately 400 °C and the amide bonds, which hold the aromatic units together, heterolytically break down between 400 and 550 °C. And then the hemolytic breaking of the amide bonds occurred until 600–650 °C.<sup>14,15</sup> To the exclusion of dramatic weight loss in the temperature ranges 40–100 °C, *m*ANF showed similar thermal stability compare to those of W-*m*ANF.

In order to confirm the influence of remained Cl on the thermal property of the nanofiber mats, additional thermal analysis was carried out using DSC, as shown in Figure 4.5B. In the first scan, endothermic bands of *m*ANF and W-*m*ANF were observed around 106 and 71 °C, respectively, and these results suggest that the remained Cl element and moisture interacted with Cl would



absorb heat. Especially, *m*ANF having a considerable amount of Cl element showed a huge endothermic peak at highest transition temperature. In the second scan, the transition of *meta*-aramid chain was found in W-*m*ANF around 272 °C, which was considered the glass transition temperature ( $T_g$ ) of *meta*-aramid chain. The arrangement of polymer segments are possible to occur through processes of *meta*-aramid dissolution in DMAc/LiCl solution and solidification during electrospinning. In the case of *m*ANF, the glass transition behavior was not observed because the remained Cl between *meta*-aramid chains interrupted the re-arrangement of the chains during heating. However, the segmental motion of *meta*-aramid chains for W-*m*ANF can be occurred due to the removal of Cl element by washing treatment. Later, the setting of heat treatment temperature for *meta*-aramid nanofiber mats was based on the DSC results.

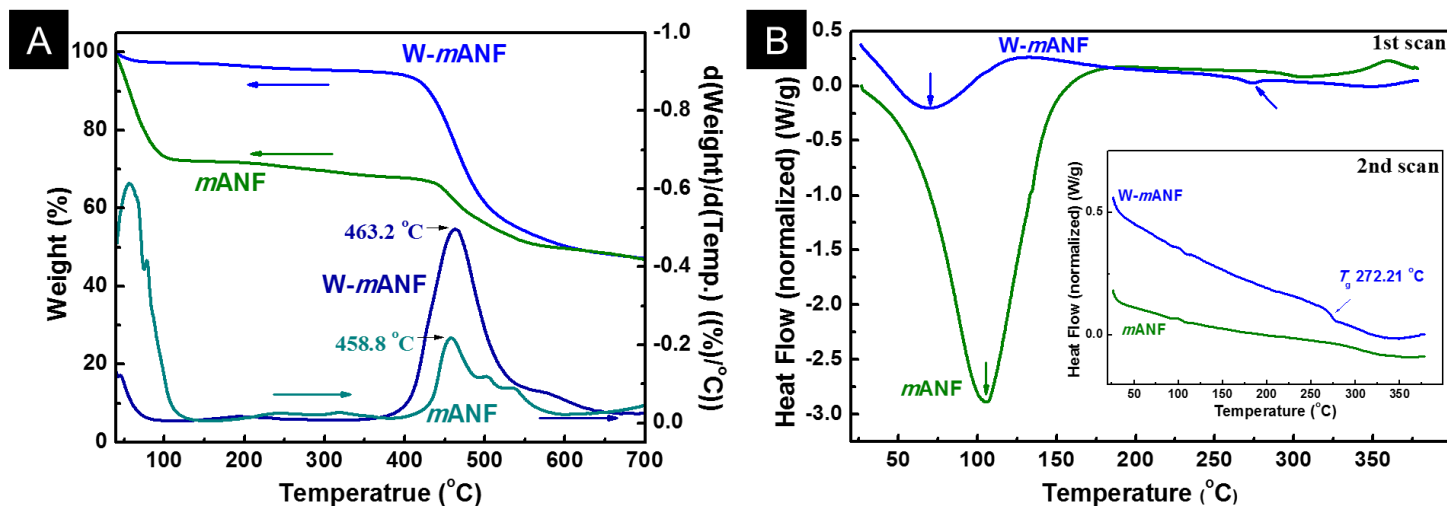


**Figure 4.5.** Thermal property of the nanofiber mats. (A) DTA/TGA curves of pristine *meta*-aramid nanofiber (*mANF*) and washed *mANF* (*W-mANF*). (B) First and second (insert) scans DSC curves of *mANF*, and *W-mANF*.

To enhance the chemical stability and mechanical property of *meta*-aramid (Nomex) nanofibers, *m*ANF and W-*m*ANF were heat-treated in air at 300 °C for 20 min (HT300-unW-*m*ANF and HT300-W-*m*ANF, respectively). ATR FT-IR spectra were observed so as to determine the change of chemical structure for the nanofiber mats. As shown in Figure 4.6A, the *meta*-aramid nanofiber mats (*m*ANF, W-*m*ANF, HT300-unW-*m*ANF, and HT300-W-*m*ANF) displayed almost identical chemical structure with commercial Nomex® fiber (Figure 4.7), which can be confirmed with the peaks for N–H stretching at 3307 cm<sup>-1</sup>, aromatic C–H stretching at 3068 cm<sup>-1</sup>, C=O···H stretching (amide I) at 1647 cm<sup>-1</sup>, aromatic C–C skeleton vibration or C=C vibration at 1604 cm<sup>-1</sup>, N–H bending (amide II) at 1528 cm<sup>-1</sup>, and C–N vibration at 1243 cm<sup>-1</sup>.<sup>12,13,16</sup> In the case of *m*ANF, the N–H stretching of *meta*-aramid and the O–H stretching of water were seen in the overlapping peak spanning from 2900 to 3700 cm<sup>-1</sup>. However, the peak for water dramatically decreased in the case of W-*m*ANF having no Cl element by washing treatment, and the peaks became extinct during heat treatment (HT300-unW-*m*ANF and HT300-W-*m*ANF). In addition, the change of secondary bonding, such as hydrogen bonding, can be determined by comparison of peak intensities between the C=O···H stretching band (amide I, 1647 cm<sup>-1</sup>) and the aromatic C–C skeleton or C=C vibration band (1604 cm<sup>-1</sup>). The latter can be constant because the aromatic group is stable and there was no chemical change during electrospinning. The peak

intensity ratios for comparison is shown in Figure 4.6B. The ratios of the *m*ANF and W-*m*ANF were decreased compared to that of Nomex® fiber. This indicates that when the *meta*-aramid dissolved in DMAc/LiCl solution were electrospun, hydrogen bonding between amide groups was not formed sufficiently. The only heat treatment above  $T_g$  (HT300-unW-*m*ANF) was not good enough to regenerate hydrogen bonding. The remained Cl between *meta*-aramid chains interrupted the arrangement of the chains and formation of hydrogen bonding during heating. In contrary, in the case of HT300-W-*m*ANF, the hydrogen bonding was formed sufficiently like Nomex® fiber. It was possible to rearrange the *meta*-aramid chains during heat treatment due to the absent of Cl element between *meta*-aramid chains.

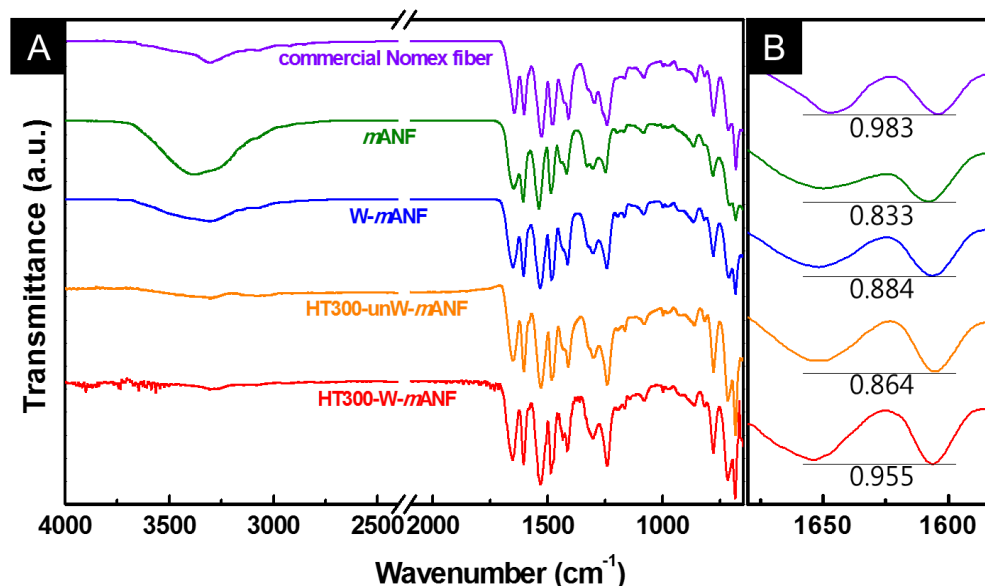


**Figure 4.6.** (A and B) Chemical structure of commercial Nomex® fiber, pristine *meta*-aramid nanofiber mat (*m*ANF), washed *m*ANF (W-*m*ANF), heat treated *m*ANF (unwashed) at 300 °C for 20 min (HT300-unW-*m*ANF), and heat treated W-*m*ANF at 300 °C for 20 min (HT300-W-*m*ANF) observed by ATR FT-IR. The insert number in Figure 5b is the transmittance peak intensity ratio of the C=O...H stretching band (amide I, 1647 cm<sup>-1</sup>) verse the aromatic C–C skeleton or C=C vibration band (1604 cm<sup>-1</sup>) and the increasing value means the regeneration of hydrogen bonding.

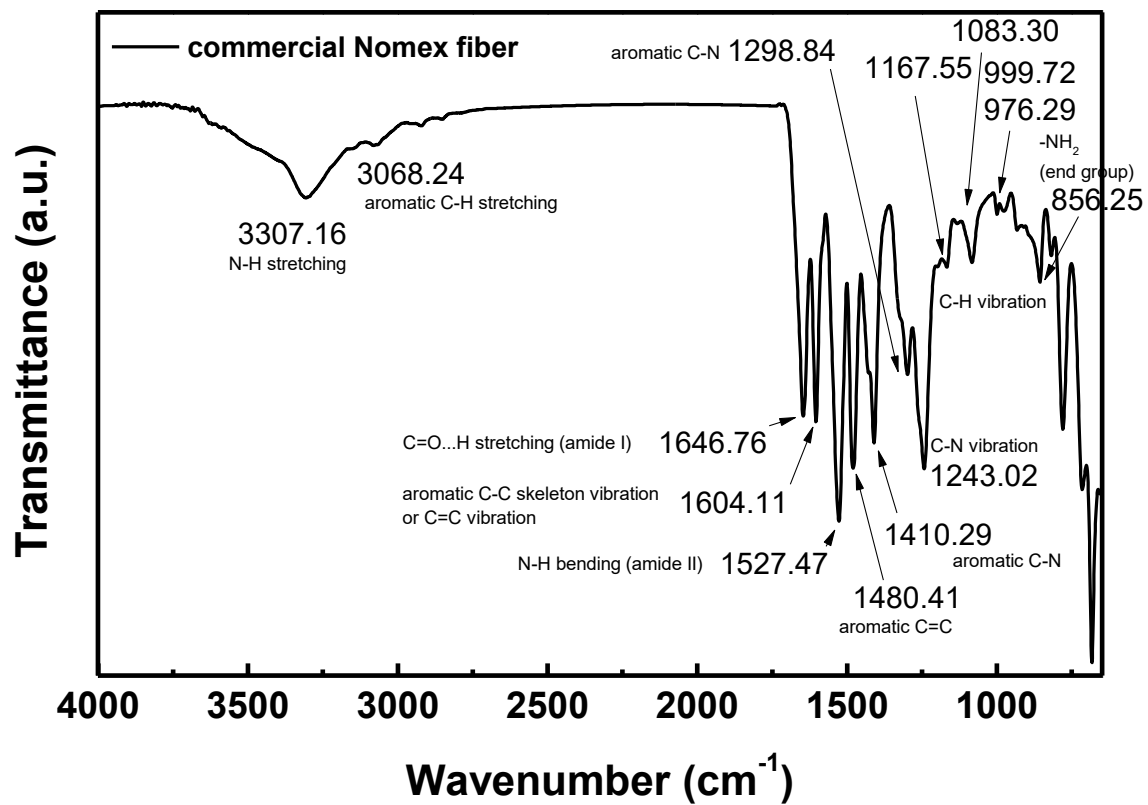


**Figure 4.7.** Chemical structure of commercial Nomex fiber observed by ATR FT-IR.

These variations of hydrogen bonding can affect the crystalline structure of *meta*-aramid, and thus, in order to evaluate the effect of the post treatments (washing and heating) on the crystalline nature of *meta*-aramid nanofibers, the crystalline structure was ascertained by WXR (Figure 4.8). The Nomex® fiber had characteristic crystalline peaks, which were assigned (110), (200), (002) and (202) planes of the crystalline phase.<sup>17,18</sup> The characteristic peaks for *m*ANF were not observed, which means that the breaking of crystalline structure of the Nomex® fiber during the dissolution in DMAc/LiCl solution and solidification during electrospinning. W-*m*ANF displayed the slightly increased (200) plane, and this pattern did not increase despite heat treatment of W-*m*ANF at 250 °C for 60 min (HT250-W-*m*ANF) (heating below  $T_g$ ). In addition, the only heat treatment above  $T_g$  (HT300-unW-*m*ANF) induced a slender increase of crystalline structure ((110) and (002, 202) planes). It was insufficient to develop the crystalline structure, because the remained Cl between *meta*-aramid chains interrupted the crystallization of the chains. However, in the case of HT300-W-*m*ANF, the characteristic peaks of (110), (200), and (002) and (202) family planes were observed clearly. The sequential post-treatment with the removal of Cl element between the *meta*-aramid chains and the crystallization via heat treatment above  $T_g$  is the most effective processing to recrystallize the *meta*-aramid nanofibers. The

recrystallization of *meta*-aramid nanofibers was closely related with the improvement of the chemical stability of *meta*-aramid nanofibers.

In order to determine the enhanced chemical stability of the nanofiber mats, it was examined whether the nanofiber mats survived in DMAc. As shown in Figure 4.9B, the *m*ANF, W-*m*ANF, and HT250-W-*m*ANF, which had non-recrystallized structure, were scarcely dissolved in DMAc when they contacted the solvent, whereas the HT300-unW-*m*ANF and HT300-W-*m*ANF were kept in shape. The HT300-unW-*m*ANF was deformed as time went by, and finally lost the original form after 24 h. However, the HT300-W-*m*ANF, which had well developed crystalline structure, maintained its shape despite being soaked in the solvent, as shown in Figure 4.9D. These results show that the chemical stability of *meta*-aramid nanofibers can be easily improved by the growth of crystalline structure using the sequential post-treatment.



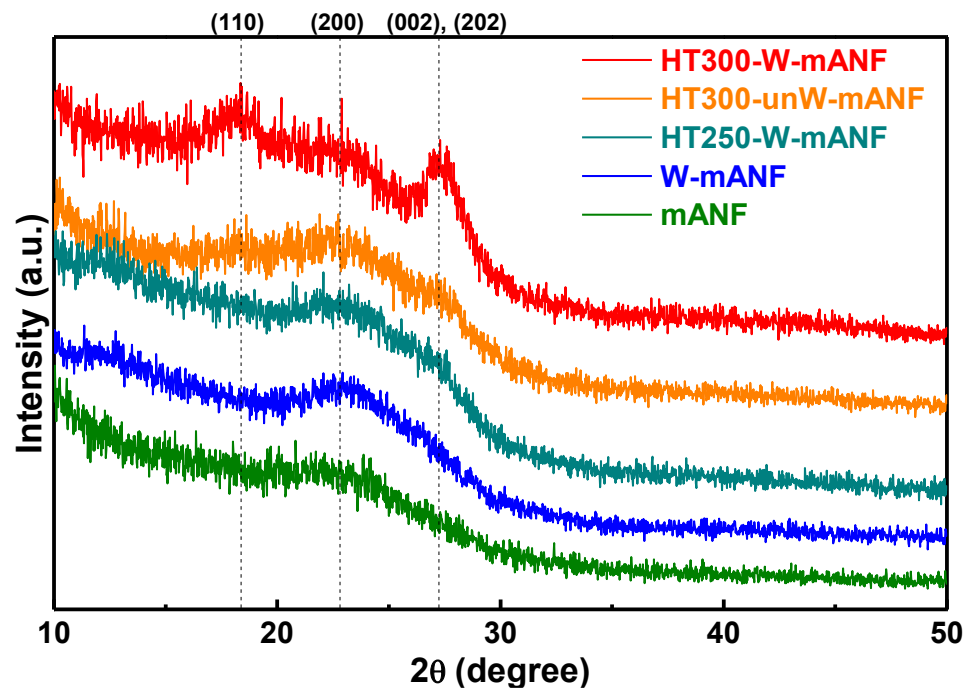


**Figure 4.8.** Crystalline structure of pristine *meta*-aramid nanofiber (*m*ANF), washed *m*ANF (W-*m*ANF), heat treated W-*m*ANF at 250 °C for 20 min (HT250-W-*m*ANF), heat treated unwashed-*m*ANF at 300 °C for 20 min (HT300-unW-*m*ANF), and heat treated W-*m*ANF at 300 °C for 20 min (HT300-W-*m*ANF).

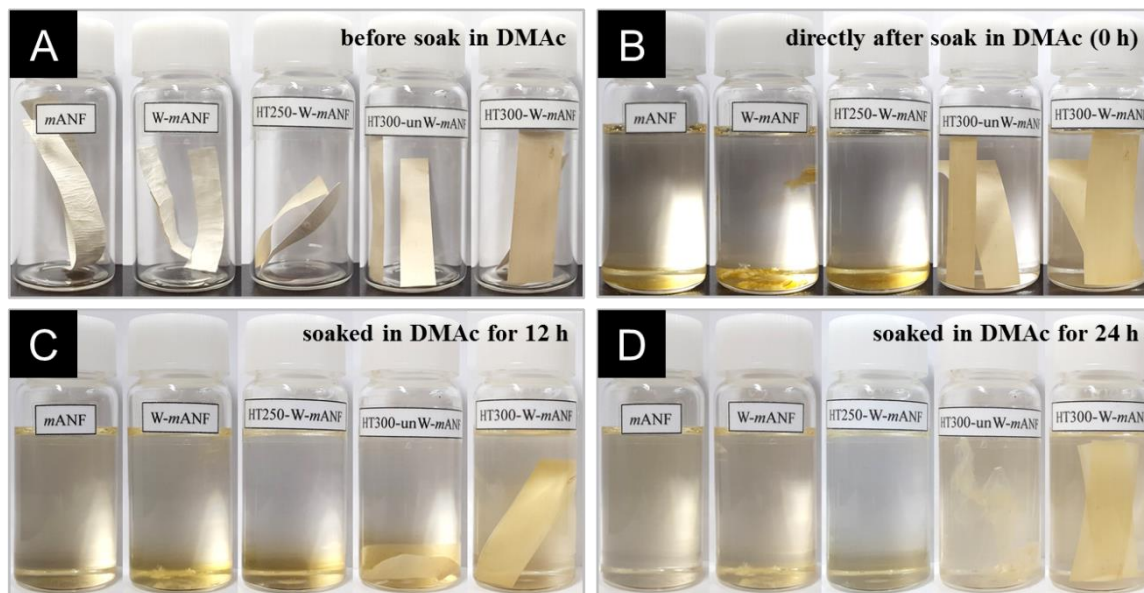


**Figure 4.9.** (A) The appearance of pristine *meta*-aramid nanofiber (*mANF*), washed *mANF* (*W-mANF*), heat treated *W-mANF* at 250 °C for 20 min (*HT250-W-mANF*), heat treated unwashed-*mANF* at 300 °C for 20 min (*HT300-unW-mANF*), and heat treated *W-mANF* at 300 °C for 20 min (*HT300-W-mANF*) before being soaked in DMAc. (B, C, and D) Observation of chemical stability for *mANF*), *W-mANF*, *HT250-W-mANF*, *HT300-unW-mANF*, and *HT300-W-mANF* soaked in DMAc for 0, 12, and 24 h, respectively.

The tensile-test was examined with the nanofiber mats in longitudinal and transverse direction of the rotating drum collector so as to investigate the mechanical property, such as the Young's modulus. As shown in Figure 4.10, all nanofiber mats displayed the higher Young's modulus in the longitudinal direction than that in the transverse direction. It indicates that the directional nature of nanofibers have a great effect on the mechanical property of nanofiber mats. In addition, the mechanical property of the nanofiber mats in the longitudinal direction was enhanced via the washing treatment and the heat treatment. Especially the heat treatment of Cl-removed nanofiber mat (W-*m*ANF) at 300 °C (above  $T_g$ ) had the greater influence on improving the mechanical property. In the case of HT300-unW-*m*ANF (Cl-remained nanofiber mat), the mechanical property did not increased enough compared to the HT300-W-*m*ANF despite the heat treatment above  $T_g$ . These results can be associated with the regeneration of crystalline structure (see Figure 4.8), which brings on the improvement of chemical stability. The regeneration of crystalline structure for *meta*-aramid is prerequisite so as to improve the mechanical property of *meta*-aramid nanofiber mats effectively.

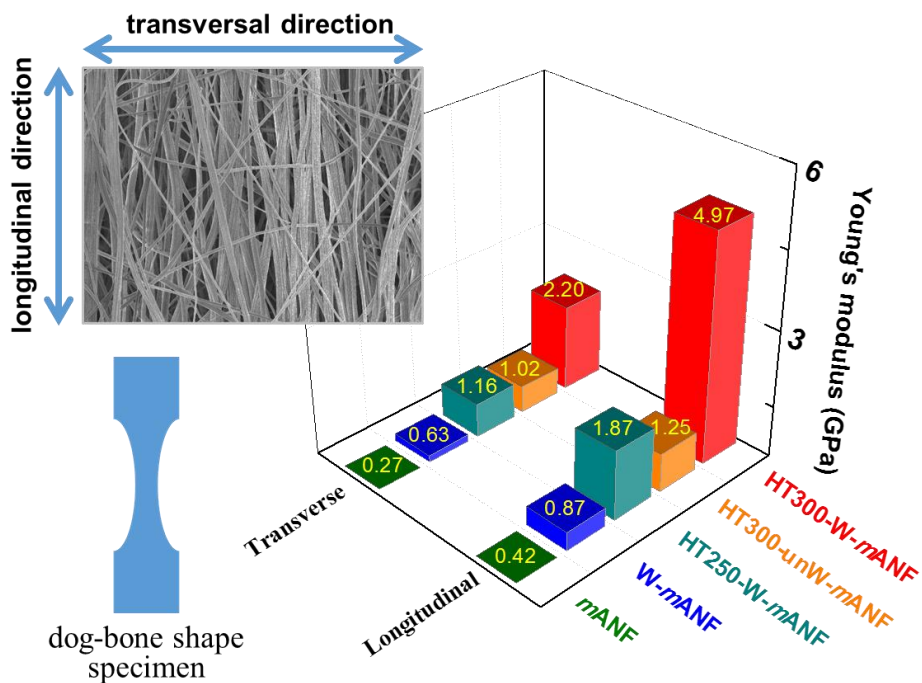


**Figure 4.10.** Young's Modulus of pristine *meta*-aramid nanofiber (*mANF*), washed *mANF* (*W-mANF*), heat treated *W-mANF* at 250 °C for 20 min (*HT250-W-mANF*), heat treated unwashed-*mANF* at 300 °C for 20 min (*HT300-unW-mANF*), and heat treated *W-mANF* at 300 °C for 20 min (*HT300-W-mANF*) in the longitudinal and transversal direction.

### **4.3.2 Nanofibrous outer layer for repellent protection against chemical warfare agent simulants**

The selected adsorbents (MgO and POM, see chapter 3) were put onto the surface of *meta*-aramid nanofibers (*mANF*) using the simultaneous electrospinning and electrospraying (SEE) process to effectively deposit the adsorbents on the surface of the nanofibers. The SEE process consists of three parts: an electrospinning part, an electrospray part and a collect part. The electrospinning was carried out at the predetermined optimal conditions: DC voltage of 20–25 kV, the distance of 15 cm and flow rate of 0.15 mL/h. The electrospray was carried out using the MgO and POM, respectively, dispersed in methanol. Methanol is a more suitable solvent than other solvents such as deionized water, ethanol, diethyl ether and THF for electrospray. The selected MgO and POM were dispersed in methanol (1.0 wt%) by using a horn-type ultrasonicator for 30 minutes. The dispersion was electrically sprayed onto the surface of *meta*-aramid nanofibers during electrospinning from the opposite side at the same time. Electrospray conditions were as follows: applied voltage was 12 kV, the suspension feed rate was 1.5 mL/h and tip-to-collector distance was 10 cm. As a result, the electrosprayed adsorbents were dispersed on and between the nanofibers. And then, the as-prepared MgO/*mANF* and POM/*mANF* composites were post-treated with the sequential salt-removal and

annealing procedure based on the optimized preparation conditions for *meta*-aramid nanofiber with enhanced chemical stability and mechanical property. Finally, the post-treated composites were treated with Unidyne (Daikin, Osaka, Japan), which is the fluorinated water and oil repellent, in order to possess the amphiphobic surface.

Pristine *m*ANF has a uniform diameter of  $207 \pm 54$  nm and uniaxially aligned array (see Figure 4.4). In the case of composites, surface-incorporated with the adsorbents (MgO and POM), the electrosprayed adsorbents were dispersed on and between the nanofibers as in Figure 4.11. The alignment character of nanofibers was preserved regardless of incorporating the adsorbents by electrospray, and it can be explained as the effect of alignment along the longitudinal direction on the mechanical characteristics as shown in Figure 4.10. In order to determine the thermal property of nanofiber composites and the content of adsorbents, thermal gravimetric analysis (TGA) and differential thermal analysis (DTA) were conducted in nitrogen at a heating rate of 10 °C/min. As shown in Figure 4.12, neat *m*ANF showed dramatic weight loss around 465 °C, and also as-prepared nanofiber composite showed similar thermal degradation behavior. There is little difference of the thermal behavior between MgO and POM incorporated nanofiber composites. The content of adsorbents in the nanofiber composites was  $14.1 \pm 0.5\%$ , calculated

from the fraction of the nanofiber and adsorbent. The temperature at 10% weight loss ( $T_{d10}$ ) and dramatic weight loss shows that the surface-incorporated adsorbents onto the nanofiber did not directly affect to the thermal property of the nanofiber composites. In contrary, final form of nanofiber composites ([O]MgO/*m*ANF), which was treated with the fluorinated water and oil repellent, has a different thermal degradation behavior. The nanofiber composite showed progressive weight loss in the range of 250–400 °C, which was not observed in others, and the weight loss originated from the thermal degradation of the fluorinated water and oil repellent. Based on the comparison of three components at 700 °C, the content of the repellent was 15.1 ± 0.3%.

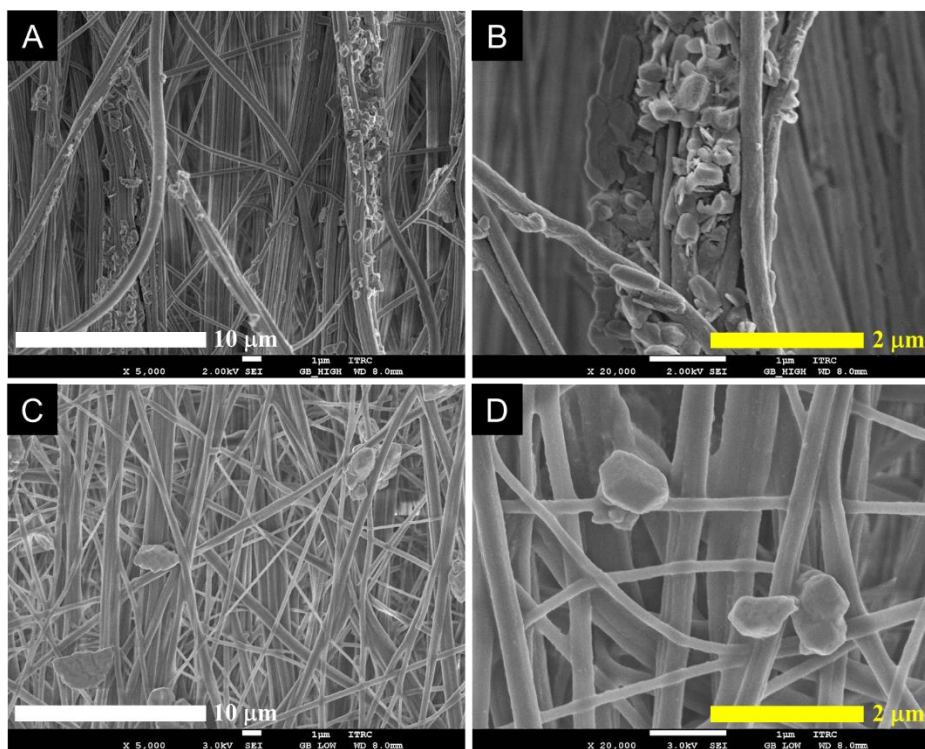


**Figure 4.11.** Morphology of (A and B) the [O]MgO/*m*ANF and (C and D) the [O]POM/*m*ANF nanofiber composites for outer layers of nanofibrous protective materials.



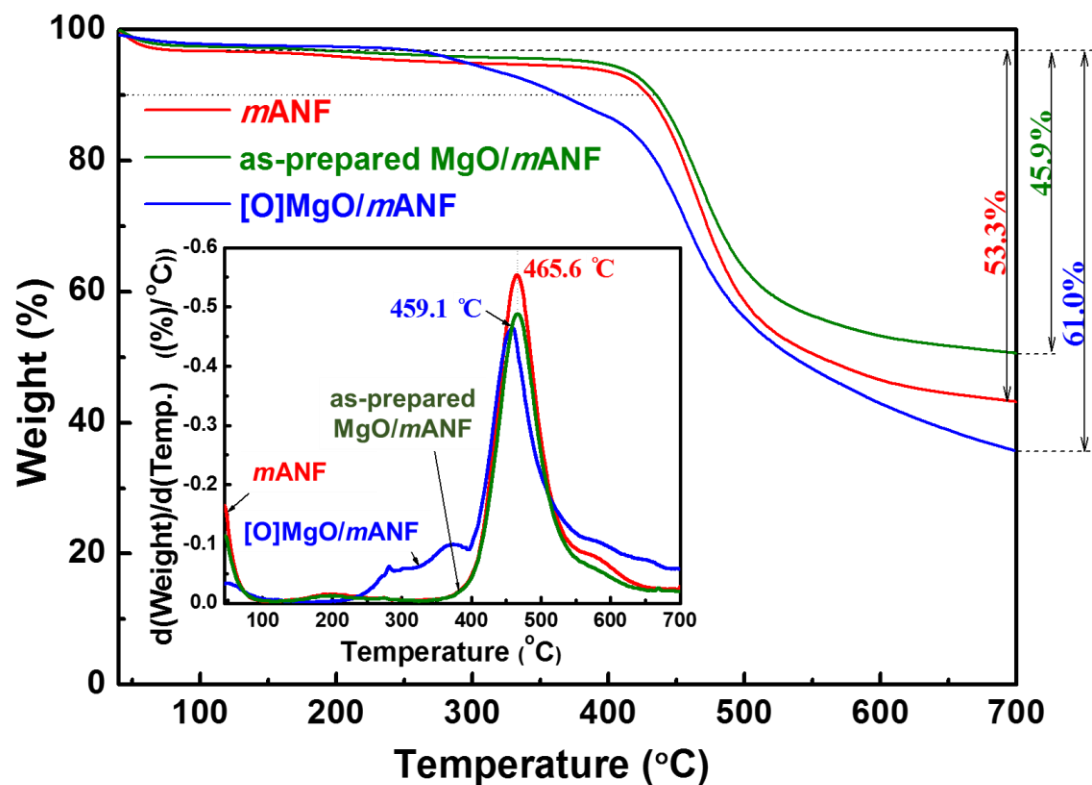


**Figure 4.12.** Thermal degradation behavior (DTA/TGA) of the neat *m*ANF, as-prepared MgO/*m*ANF, and [O]MgO/*m*ANF.

In order to estimate the protective performance of nanofiber composites against liquid CWA, the surface wettability or non-wettability of the nanofiber composites was evaluated using water and oil contact angle (WCA and OCA) measurement with water and dimethyl methyl phosphonate (DMMP, Sarin simulant). The contact angle formed between the tangent plane to the surface of the nanofiber mats and the tangent plane to the surface of the liquid droplet at the point of intersection as shown in Figure 4.13. The *m*ANF and as-prepared nanofiber composites absorbed quickly both water and DMMP (zero degree contact angle). This result indicates that they originally have high affinity to water and oil. In contrary, the nanofibers, which were treated with fluorinated water and oil repellents I and II, exhibited the amphiphobic nature as in Figure 4.14. There were the difference of repellency performance according to the type of repellents. In the case of the repellent I, which was water-based emulsion containing 20–30% fluoroalkyl acrylate copolymer, the nanofiber composite incorporated with MgO ([O]MgO/*m*ANF) exhibited super-hydrophobicity (greater than 150° WCA) and high oleophobicity (higher than 120° OCA) at the same time with just only 1<sup>st</sup> treatment. In order to enhance the amphiphobic nature of surface, the treatments were repeated, but there was no improvement. In the case of [O]MgO/*m*ANF treated with the repellent II, which was 1*H*,1*H*,2*H*,2*H*-perfluorooctyl trichlorosilane, as the

modification was repeated, the WCA increased gradually from 139 to 157°. The OCA increased to 124° up to three times modification, whereas the OCA decreased to 102° at the five times modification. In addition, the same pattern could be seen with the repetitive treatment with higher concentrated repellent II (1.0 % V/V FAS/toluene). The treatment with low concentration (0.1% V/V FAS/toluene) was more effective rather than that with higher concentration (1.0% V/V FAS/toluene) (data not shown). Based on these results, it was concluded that the amphiphobic nanofiber composites for outer layer, composed with Nomex nanofiber and the adsorbents (MgO and POM), can be fabricated effectively through the amphiphobic surface treatment using the repellent I. The nanofiber composites will be able to show the excellent repellency against liquid CWA.

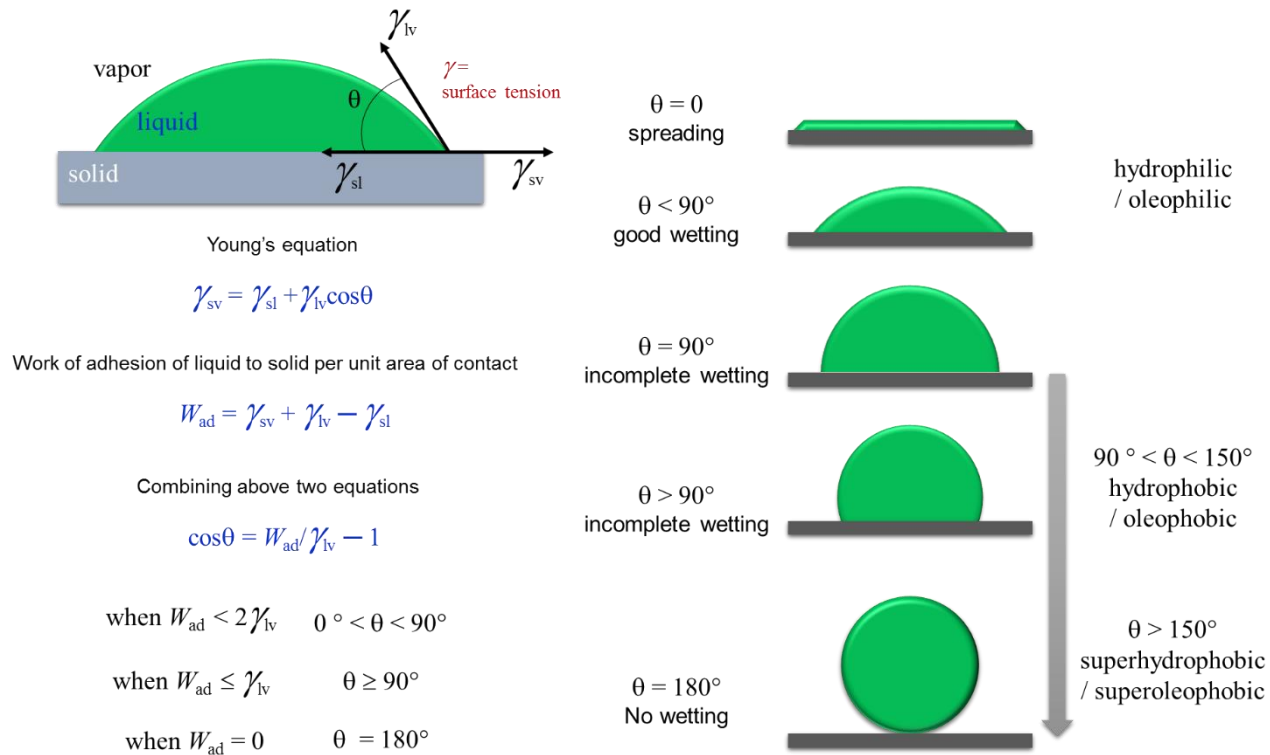


**Figure 4.13.** Schematic of a liquid droplet showing the quantities in Young's equation.

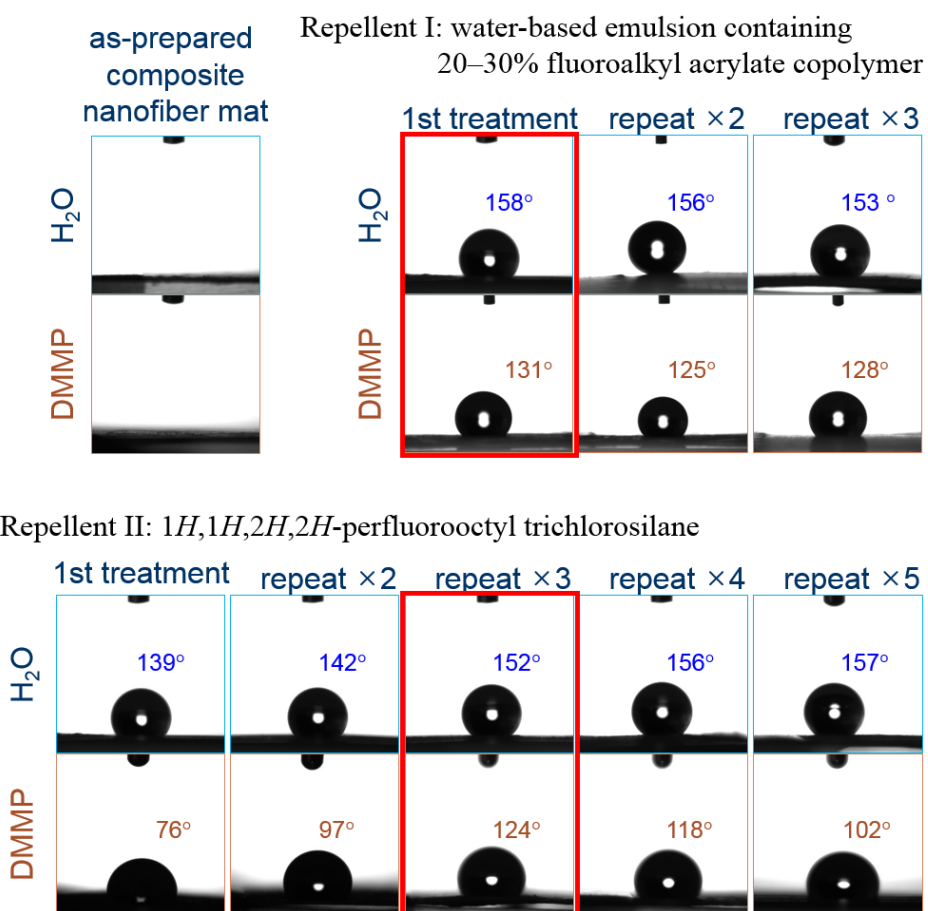


**Figure 4.14.** Amphiphobic surface property of [O]MgO/*m*ANF for outer layers of nanofibrous protective materials.

## 4.4 Summary

In this study, an amphiphobic *meta*-aramid nanofiber mat with improved chemical stability and mechanical properties was fabricated using a sequential post-treatment involving the removal of Cl element between the *meta*-aramid chains, crystallization via heat treatment above  $T_g$ , and surface silanization. Aligned *meta*-aramid nanofibers containing LiCl (*mANF*) were prepared using electrospinning with a drum-collector, and the obtained nanofiber mats were post-treated with washing and annealing. The Cl element present between the chains of the as-spun mat was clearly eliminated during washing treatment, and the washed nanofiber mat (W-*mANF*) showed a glass transition behavior around 272°C ( $T_g$ ). This indicated that heat treatment above the  $T_g$  would allow the rearrangement of the *meta*-aramid chains with no salt, inducing the regeneration of the crystalline structure and inter-molecular hydrogen bonding. Indeed, the *meta*-aramid nanofiber mat heat-treated at 300°C for 20 min (HT300-W-*mANF*) displayed improved chemical stability, confirmed by its survival in DMAc for 24 h, and a 11.8-fold Young's modulus in the longitudinal direction compared with that of the pristine nanofiber mat (*mANF*). These enhancements were attributed to the orientation and crystallization of the salt-removed *meta*-aramid chains during annealing. Finally, the amphiphobic *meta*-aramid nanofiber mat was developed via treatment using water and oil

repellent, showing unwet surface by both water and DMMP (contact angle of 152° and 123°, respectively). Improvement of the chemical stability and mechanical properties of *meta*-aramid nanofibers is a prerequisite for many practical applications requiring high durability, such as protective layers with corrosion resistance, water/gas/particulate filter media, and secondary battery separators. These results will enable the design and production of enhanced nanofibrous materials based on *meta*-aramid. In addition, these findings reveals that the amphiphobic *meta*-aramid nanofiber mat can be usefully applied as a protective material against liquid phase of various contaminants.

## References

1. Wang, C.; Yan, E.; Huang, Z.; Zhao, Q.; Xin, Y. *Macromol. Rapid Commun.* **2007**, *28*, 205.
2. Thandavamoorthy, S.; Gopinath, N.; Ramkumar S. S. *J. Appl. Polym. Sci.* **2006**, *101*, 3121.
3. Ramakrishna, S.; Fujihara, K.; Teo, W. E.; Yong, T.; Ma, Z.; Ramaseshan, R. *Mater. Today* **2006**, *9*, 40.
4. Ramaseshan, R.; Sundarrajan, S.; Liu, Y.; Barhate, R. S.; Lala N. L.; Ramakrishna, S. *Nanotechnology* **2006**, *17*, 2947.
5. Shealy, O. L. *Text. Inst. And Industry* **1971**, *10*.
6. Northolt, M. G. *Eur. Polym. J.* **1974**, *10*, 799.
7. Yao, L.; Lee, C.; Kim, J. *Fibers Polym.* **2011**, *11*, 1032.
8. Lin, J.; Ding, B.; Yang, J.; Yu, J.; Al-Deyab, S. S. *Mater. Lett.* **2012**, *69*, 82.
9. Shin, C.; Chase, G. G. *J. Dispersion Sci. Technol.* **2006**, *27*, 517.
10. Yao, L.; Kim, J. *Adv. Mat. Res.* **2011**, *175-176*, 318.
11. Oh, H. J.; Han, S. H.; Kim S. S. *J. Polym. Sci. Pt. B-Polym.* **2014**, *52*, 807.
12. Oh, H. J.; Pant, H. R.; Kang, Y. S.; Jeon, K. S.; Pant, B.; Kim, C. S.; Kim, H. Y. *Polym Int* **2012**, *61*, 1675.
13. Villar-Rodil, S.; Paredes, J. I.; Martínez-Alonso, A.; Tascón, J. M. D. *Chem. Mater.* **2001**, *13*, 4297.
14. Kalashnik, A. T.; Panikarova, N. P.; Dovbii, Y. V.; Kozhina, G. V.; Kalmykova, V. D.; Papkov, S. P. *Vysokomol. Soedin.* **1977**, *12*, 2747.
15. Brown, J. R.; Power, A. *J. Polym. Degrad. Stab.* **1982**, *4*, 379.
16. Davis, R.; Chin, J.; Lin, C.-C.; Petit, S. *Polym. Degrad. Stab.* **2010**, *95*, 1642.
17. Panar, M.; Avakian, P.; Blume, R. C.; Gardner, K. H.; Gierke, T. D.; Yang, H. H. *J. Polym. Sci. Polym. Phys. Ed.* **1983**, *21*, 1955.
18. Castro-Muñiz, A.; Martínez-Alonso, A. Tascón, J. M. D. *Carbon* **2008**, *46*, 985.



## **Chapter 5**

# **Multilayer Assemblies of Nanofiber Composites as Permeable Protective Materials against Chemical Warfare Agents**

### **5.1 Introduction**

Chemical warfare agents (CWAs) have been used in tactical warfare as incendiary mixtures, smoke, and irritating, burning, poisonous, or asphyxiating gases.<sup>1</sup> CWAs have been classified according to their target organs or tissues as nerve, vesicant, choking, blood and vomiting agents, as well as incapacitants and lacrimators.<sup>2</sup> Many CWAs are dermally active; therefore, a number of studies on materials that provide protection against CWAs have been performed.<sup>3-5</sup> There are various types of defense equipment available to protect the body from CWAs, including detectors, respirators, protective clothing, decontaminants and medical countermeasures.<sup>6</sup> Protective clothing can be classified into impermeable and permeable categories. Impermeable protective clothing offers powerful protection against CWAs, but is unfit for long-term wear because it is cumbersome and uncomfortable. In contrast, permeable protective clothing is composed of outer and inner layers to make it breathable. The outer layer repels the liquid CWA that is trying to penetrate

the protective clothing. The inner layer consists of nonwoven fabric or porous foam impregnated with an adsorbent, such as activated carbon, to chemisorb any gas CWA that enters through the outer layer.

The activated carbon materials used in permeable protective clothing is impregnated with nanoparticles composed of silver, tin, zinc or molybdenum, along with triethylenediamine. A popular example of a permeable protective garment containing activated carbon materials is the joint service lightweight integrated suit technology (JSLIST) overgarment, which has been used by the US Army.<sup>7</sup> Permeable protective clothing like the JSLIST suit offers complete protection against CWAs, but it has associated disadvantages such as moisture retention and heavy weight (2.63 kg per overgarment), resulting in discomfort. These disadvantages prevent users from wearing JSLIST suits for more than 6–8 h at a time. Therefore, there is a need to develop a more comfortable material that is light, with high moisture permeability, but that still protects the wearer from CWAs.

The disadvantages of existing permeable protective clothing can be overcome by replacement with lightweight materials composed of structures such as nanofibers. Nanofibers show improved properties compared with those of conventional fibers because of their small dimensions and unique features, such as high surface-to-volume ratio, small fiber-to-fiber distance, high porosity, large specific surface area, small pore size, and high controllability. These

unique characteristics, plus the functionalities of the materials themselves, impart nanofibers with a number of novel properties that are attractive for advanced applications. Nanofibers have been used in protective clothing for CWAs, as well as for biological warfare agents. Various methods to modify nanofiber surfaces to enhance their protection and decontamination capabilities have been developed based on chemical surface modification and attachment of reactive groups on the nanofiber surface, and especially functionalized nanofibers for protection from chemical warfare simulants based on hydrolysis have been developed and evaluated.<sup>8</sup>

A number of new protective materials with higher adsorption capacity, lighter weight and greater comfort than their predecessors have been designed. Catalysts and adsorbents with detoxification activity such as MgO,<sup>9,10</sup> MnO<sub>2</sub>,<sup>11</sup> ZnO,<sup>12,13</sup> TiO<sub>2</sub>,<sup>14</sup> ZnTiO<sub>3</sub>,<sup>15</sup> M/TiO<sub>2</sub>/SiO<sub>2</sub> (M = Fe, Mn, and V),<sup>16</sup> WO<sub>3</sub>/titanate,<sup>17</sup> N-doped TiO<sub>2</sub>,<sup>18</sup> Au/TiO<sub>2</sub>,<sup>19</sup> and polyoxometalate (POM)<sup>20</sup> have been actively investigated as the fillers incorporated in such permeable protective clothing. Among these fillers, MgO has been widely studied as an effective catalyst against the nerve agent sarin because it is highly active and can readily decompose this nerve agent.<sup>21</sup> MgO can physisorb CWAs on its surface through the formation of hydrogen-bonding, ion-dipole and dipole-dipole interactions.<sup>22</sup> In addition, POM has been considered as a reactive

adsorbent for the decontamination of vesicant agents such as sulfur mustard gas.<sup>23</sup>

In this study, it was presented that a potential application of nanofibrous composite materials impregnated with MgO and POM adsorbents as the inner and outer layers, respectively, of permeable materials that are protective against CWAs. The inner and outer layers of the nanofiber composites were stacked on one another to assemble protective clothing materials. The outer layer consists of both *meta*-aramid nanofibers and the adsorbents and has an amphiphobic nature, so the liquid CWA simulants bounce off it. The inner layer is composed of Nylon 66 nanofibers with MgO and POM as adsorbents, and plays a role in protection by adsorbing gas CWA simulants. The assembly of these two layers improved the thickness, weight, water vapor transmittance, cool/warm feeling and protection against CWA simulants compared with the corresponding properties of existing permeable protective clothing materials. In particular, the thickness and weight density of the material depended on the number of stacked layers. Lightweight assemblies with high protection against CWAs were developed. These assemblies provide good resistance to the penetration of gaseous CWAs, while still allowing water vapor transmission to promote evaporation cooling of the wearer. The assembly of multiple layers developed here reveals a new approach to improve the performance of permeable protective materials, and will aid the design and optimization of permeable protective clothing.

## **5.2 Experiments**

### **5.2.1 Assembly of the outer and inner layers for nanofibrous protective materials against chemical warfare simulants**

To fabricate the nanofibrous protective materials, assemblies of the outer and inner layers were prepared by a spray- and heat-bonding process (Figure 5.1). Multiple layers were sequentially positioned on top of one another. First, the spray glue was spread on an inner layer through a mesh to minimize the loss of available active area on its surface. Another inner layer was then placed above the adhesive surface of the bottom layer. This procedure was repeated one to seven times. The outer layers were positioned on the inner layers perpendicular to the direction of nanofiber alignment (rotated 90° between adjacent layers). Finally, assemblies composed of two outer layers and two to eight inner layers were obtained by heat-pressing at 80 °C under 500 psi for 10 min using a hydraulic press (Carver, model 2702, USA).

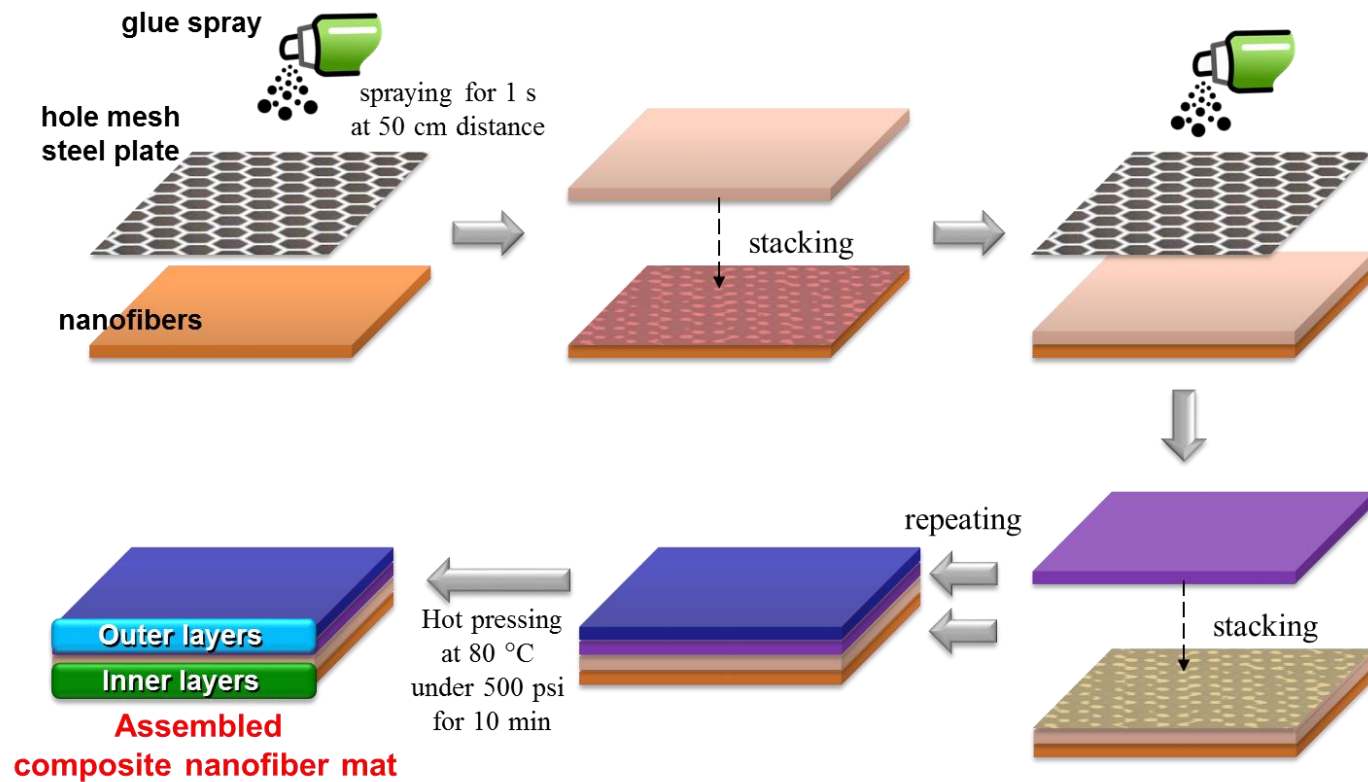


**Figure 5.1.** Fabrication process for assembly of nanofiber composites via adhesion with glue spraying and hot pressing.

### 5.2.2 Characterization of the assembly of the outer and inner layers

To examine the physical characteristics of the assemblies, various characterization techniques, such as air permeability, WVTR, and maximum heat transfer rate ( $q_{\max}$ ), were investigated using the standard methods ASTM D737, ASTM E96, and KES-F7 Thermo LaboII, respectively. The cool/warm feeling of the assembly was examined by measuring  $q_{\max}$ <sup>24</sup> using a Thermo Labo II (KES-F7, KATO Tech Co., Japan), the main components of which were a temperature-detecting box (T-Box) and bottom-temperature box (BT-Box). The assembly, which was maintained at 20 °C, was positioned between the T-Box and BT-Box, which were heated to 32 °C to simulate human skin. Then,  $q_{\max}$  was quickly measured for 0.2 s from the moment of contact. The reported results are the average of five experiments. The permeation of gas CWA simulants (2-CEES and DMMP) through each assembly was determined by permeation experiments according to the TOP 8-2-501 standard, as outlined in Figure 5.2. The TOP 8-2-501 test method is based on the static diffusion procedure described in the U.S. Army Test and Evaluations Command Test Operations Procedure.<sup>25</sup> The permeation test cell was composed of a cap and a base. A circular sample was positioned on the base containing a central well with a 5.7-cm diameter and inlet and outlet ports connected to Tygon tubing. The liquid simulant (2-CEES or DMMP) was dropped onto the surface of the

sample at a fixed ratio of 10 g/m<sup>2</sup> based on sample area. A cap covered the top of the sample and simulant to limit escape of the evaporated gas simulant. The liquid simulant on the sample evaporated into the space covered by the cap, and then the gas simulant crossed through the sample. Input N<sub>2</sub> gas that delivered gas simulant (2,000 cc) to the Tenax-TA tube was regulated using a flow meter (MKP, MPR-3000s) with a flow rate of 200 ccm. The captured gas was evaluated by TD-GC-MS.



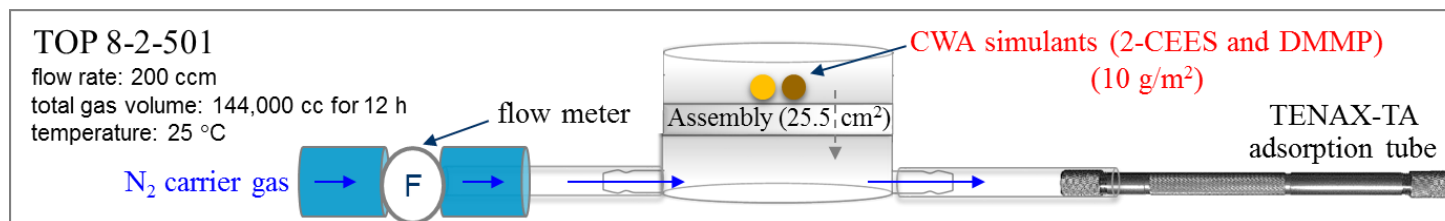


Figure 5.2. Schematic representations of experimental system (static diffusion procedure) to investigate the resistance of the assembly of nanofiber composites to permeation by CWA simulants.

## **5.3 Results and Discussion**

### **5.3.1 Assembly of the outer and inner layers for nanofibrous protective materials against chemical warfare simulants**

The nanofiber mat is too thin to have the proper mechanical properties for practical use. In order to enhance the mechanical property, the nanofibrous protective materials against chemical warfare agents was fabricated by stacking of the inner and outer layers, which were explained in chapter 3 and 4. The schematic of the nanofibrous protective materials composed with the nanofiber composites was illustrated in Figure 5.3. The number of outer and inner layers was coordinated so as to compare the protectability against CWA according to the thickness. Also, in order to compare the effectiveness of the adsorbents (MgO and POM), outer and inner layers incorporated with same type of adsorbent were made a pair. Especially, it was desired that the outer layer of Nomex nanofiber be made with over two layers, because the Nomex nanofiber had an alignment in the same direction. The outer layer showed excellent mechanical property along the alignment direction, but that showed less attractive mechanical property along the transversal direction of alignment (see Figure 4.10). The control of the staking layers allows the regulation of the entire performance. The repellent nature of outer layers enables the assembly to prevent the liquid CWA invasion. Also, the adsorbents, which is located in outer and inner layers, are expected to restrain the gas CWA penetration.

The physical properties, such as thickness, weight per area, cool/warm feeling and air/moisture permeability, of the assembly were compared with the permeable protective clothing of Korea Army as a reference, which is now being used as a chemical protective gear. As exhibited in Figure 5.4, the permeable protective clothing of Korea Army was modeled on the Battle Dress Overgarment (BDO), which had been used before in US Army. The component of that is as follows: 1) outer layer (260 g/m<sup>2</sup> of weight density) composed with 50/50 polyester/cotton fabric with a water/oil repellent finish and 2) inner layer (360 g/m<sup>2</sup>) made of polyurethane foam containing the activated carbon power. That is too heavy and thick, and shows low performance.

### **5.3.2 Characterization of the assembly of the outer and inner layers**

The physical properties of the assembly closely depended on the number of stacked layers, and so, the desired and targeted properties were able to be improved by means of stacking. As shown in Table 5.1, the thickness and the weight per area increased as the piling up of layers. In the case of the assembly composed with 2 sheets of outer and 6 sheets of inner layers, the thickness and weight of the assembly exhibited a similar level compared to that of the reference. So, in order to improve the disadvantage attributed to the heavy weight of the currently used permeable protective clothing, the number of piling up with the layers for the assembly was limited to maximum of 8 sheets.

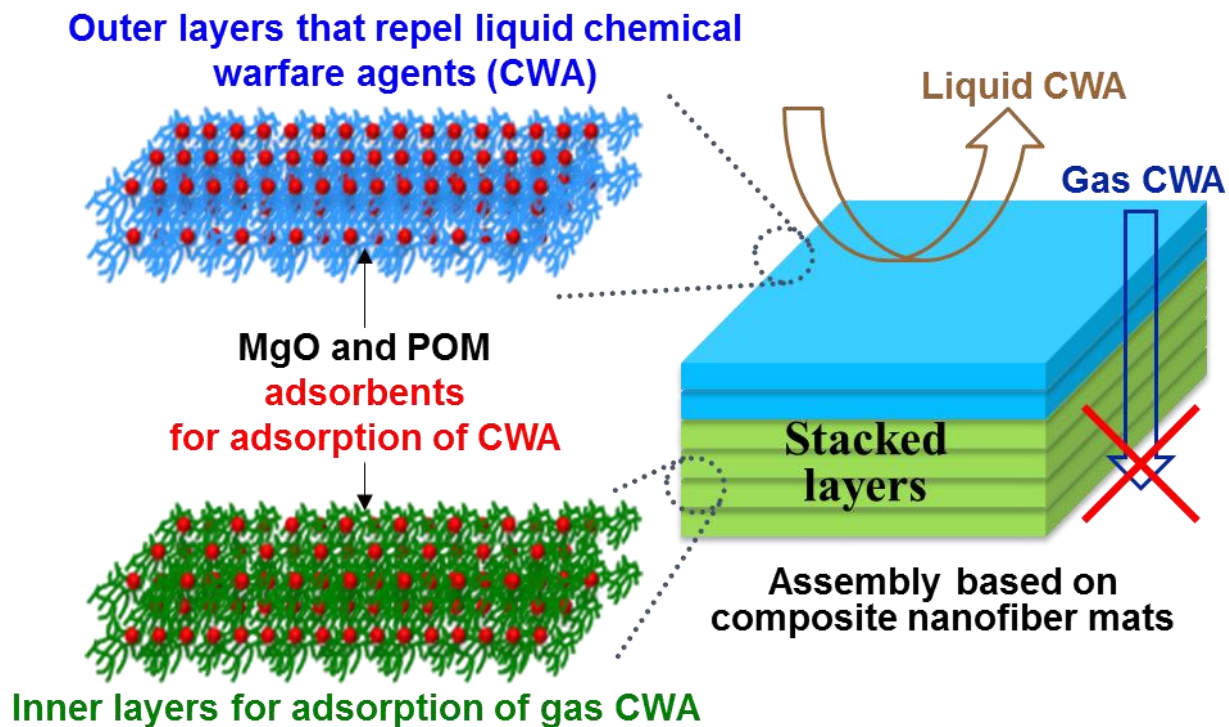
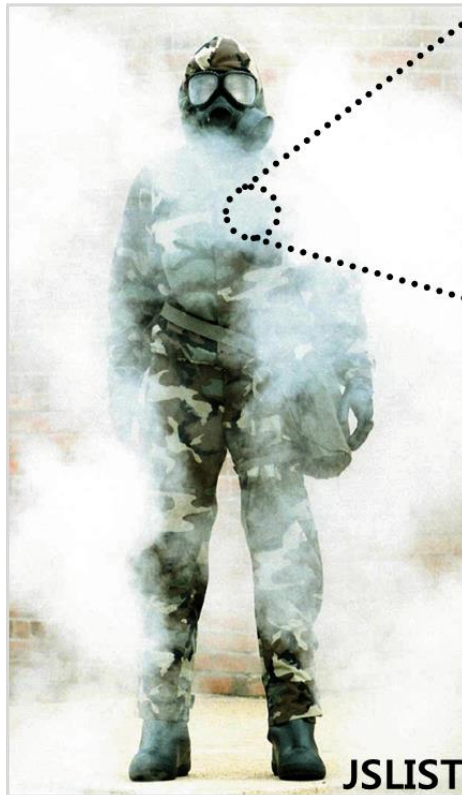


**Figure 5.3.** Schematic representation of the assembled nanofibrous composite composed with inner and outer layers for protective materials against chemical warfare agent (CWA).



● US Army: Joint Service Lightweight Integrated Suit Technology (JSLIST) (current using)

- Outer layer: 50/50 Nylon/cotton poplin ripstop with a durable water repellent finish
- Inner layer: nonwoven front laminated to activated carbon spheres and bonded to a tricot knit back

● Korea Army: similar type with the Battle Dress Overgarment (BDO) of US Army

- Outer layer: 50/50 polyester/cotton poplin with a durable water repellent finish
- Inner layer: polyurethane foam containing the activated carbon powder

**Figure 5.4.** Example of permeable protective clothing against chemical warfare agents.

The maximum heat transfer rate,  $q_{\max}$ , was able to evaluate the cool and warm feeling of a clothing materials. Cool and warm cold feeling represents the transfer of heated measuring body to the specimen which has lower temperature. The degree of transferred heat, which is reached for 0.2 seconds from the moment the specimen contacts with the heated body, is converted to the value of  $q_{\max}$ . The  $q_{\max}$  value may be increased or decreased depending on the specimen. If the value is higher, it indicates that the material gives a feeling of cold and vice versa. The  $q_{\max}$  of the assembly with various thickness was listed in Table 5.1. There was little difference between MgO and POM incorporated assembly with same thickness. In the case of the assembly, the cool feeling was decreased as the increasing thickness by piling up the layers. Also, it is revealed that the assembly, which was composed with 2 sheets of outer and 6 sheets of inner layers, showed a cooler feeling compared to the current used permeable protective clothing. The inner layer of the clothing (I-KA) had a great effect on a warmer feeling of the clothing. Because I-KA was formed of a thick polyurethane foam (1.3 mm), which contained a considerable amount of air. These results show that the assembly made of the nanofiber composites can give cooler feeling compared to the currently used protective clothing.

**Table 5.1.** Weight, thickness and maximum heat transfer rate ( $q_{\max}$ ) of the assembled nanofiber composites

	Outer / Inner layers of Permeable protective clothing for Korea Army (O-KA / I-KA)				Nanofibrous Outer/Inner Layers of MgO or POM incorporated type		
	Thickness ( $\mu\text{m}$ )	Weight per area ( $\text{g/m}^2$ )	Maximum heat transfer rate, $q_{\max}$ ( $\text{W/cm}^2$ )		Thickness ( $\mu\text{m}$ )	Weight per area ( $\text{g/m}^2$ )	Maximum heat transfer rate, $q_{\max}$ ( $\text{W/cm}^2$ )
Outer layer (O)	380	260	0.154	O 1 sheet	75	33	0.126
				O 2 sheets	137	65	0.123
Inner layer (I)	1,300	360	0.092	I 1 sheet	91	62	0.145
				I 2 sheets	166	125	0.143
Assembly (O+I)	1,700	620	0.089	O 2 sheets + I 2 sheets	415	285	0.124
				O 2 sheets + I 4 sheets	542	423	0.121
				O 2 sheets + I 6 sheets	681	581	0.116
				O 2 sheets + I 8 sheets	817	653	0.110

In order to estimate the gas transfer through the protective clothing materials, the air and water vapor permeability of the assemblies with different composition and thickness were compared with the currently used permeable protective clothing as in Table 5.2. The protective clothing showed the higher air permeability than the assemblies, because the outer layer was made of a woven fabric with warp-and weft threads and the inner layer was made of polyurethane foam with many holes. Whereas, the assemblies were consisted of nonwoven nanofiber mats, and so they exhibited the extremely low the air permeability less than 0.5 cfm. The nanofiber mats, consisting the assemblies, has small fiber diameter less than 300 nm and various pores with 140 nm of mean flow pore size. An interesting complicating factor in the analysis of air permeability through the assemblies is that the mean free path of air becomes comparable to the fiber size.<sup>26</sup> There is the air spin at the nanofiber surface, and the normal linear dependence of air permeability with pressure drop becomes less applicable to the air flow field in the pores. It has been evaluated that the pressure drop predicted by assuming continuous flow through the beds of fibers is reduced by a factor of 1/3 for a fiber with 100 nm diameter.<sup>27</sup> For water vapor transport, although the assemblies showed the low air permeability, they exhibited excellent water vapor transport. Especially, the assemblies composing of 2 sheets of outer and 6 sheets of inner layers had similar water vapor permeability compared to the protective clothing. However, the water



vapor permeability of the assemblies, consisted with 2 sheets of outer and 8 sheets of inner layers or more layers, was decreased dramatically.

Based on the results of the air and water vapor permeability, one implication of the assemblies consisted with the nanofiber mat is that the assemblies would provide good resistance to the penetration of chemical warfare agents in gas form, while still allowing significant water vapor transmission to promote evaporate cooling of the body. The nanofiber composite has porous structure with about 140 nm of mean flow pore diameter. The resistance to air flow is quite large because of the small diameter and flow pore size in the assemblies. The high resistance to air flow does not impede the diffusion of moisture through the pore structure of the nanofiber mat. After considering of these results, the assemblies can be considered as promising candidates for protective clothing materials due to its high rates of water vapor transmission and low air flow.

**Table 5.2.** Air permeability and water vapor transmission of the assembled nanofiber composites

	Outer / Inner layers of Permeable protective clothing for Korea Army (O-KA / I-KA)			MgO incorporated type Outer or Inner Layers		POM incorporated type Outer or Inner Layers	
	Air permeability (cfm)	Water vapor transmission (g/m <sup>2</sup> /24h)		Air permeability (cfm)	Water vapor transmission (g/m <sup>2</sup> /24h)	Air permeability (cfm)	Water vapor transmission (g/m <sup>2</sup> /24h)
Outer layer (O)	5.41	4,342	O 1 sheet	0.534	4,809	0.503	4,675
			O 2 sheets	0.272	4,748	0.267	4,480
Inner layer (I)	60.7	3,623	I 1 sheet	0.706	4,575	0.661	4,722
			I 2 sheets	0.326	4,282	0.352	4,331
Assembly (O+I)	4.27	3,292	O 2 sheets + I 2 sheets	0.162	4,062	0.168	4,229
			O 2 sheets + I 4 sheets	0.057	3,662	0.064	3,809
			O 2 sheets + I 6 sheets	0.032	3,229	0.036	3,494
			O 2 sheets + I 8 sheets	0.026	2,188	0.030	2,276

In order to estimate the protective performance of the assemblies against liquid CWA, their surface wettability was evaluated using water and oil contact angle (WCA and OCA) measurement with water, 2-CEES and DMMP. Also, the surface wettability of the outer layer of the protective clothing (O-KA) was measured with same way and compared to that of the assemblies. The samples showed the amphiphobic nature as shown in Figure 5.5. The O-KA showed both hydrophobicity with a WCA higher than  $120^\circ$  and oleophobicity. The assemblies exhibited super-hydrophobicity (greater than  $150^\circ$  WCA) and high oleophobicity (higher than  $120^\circ$  OCA) at the same time. The difference of non-wettable surfaces between the assembly and O-KA was attributed by the surface roughness of samples. The surface geometric structure has been identified as one of the most important factors which affect the wettability of the surface.<sup>28</sup> In the case of the outer layer of assembly, the adsorbents (MgO and POM) were incorporated on the surface of nanofibers and nanofiber mat, and so the outer layer had a rougher surface than that of O-KA. The increase of surface roughness was essential to develop nonwettable surfaces. These increasing roughness induced the improvement of protectability for the assembly against CWA simulants.

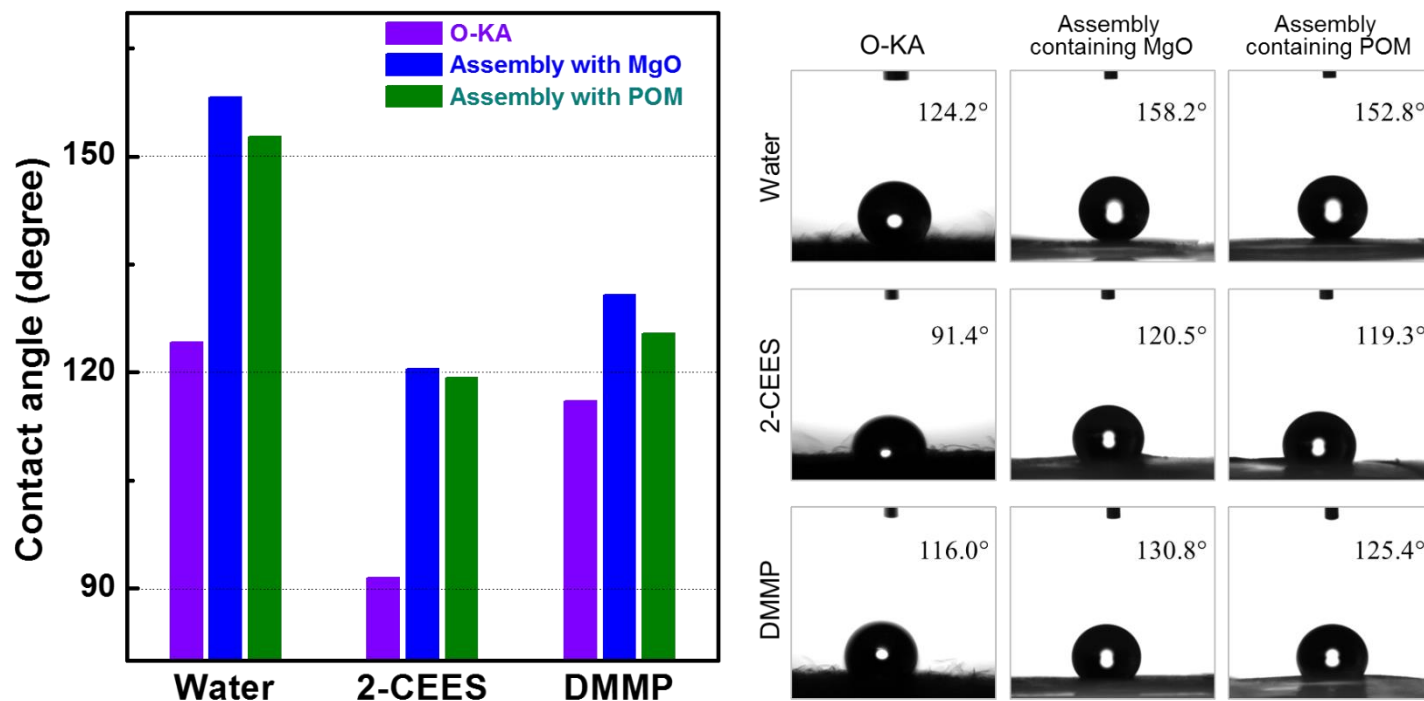


**Figure 5.5.** Amphiphobic surface property of the outer layer of permeable protective clothing for Korea Army (O-KA), and the assembly incorporated with MgO and POM for nanofibrous protective materials against the simulants (2-CEES and DMMP) of the chemical warfare agents.

In order to investigate the resistance of the assemblies to permeation by gas CWA, the permeation test according to the TOP 08-2-501 method was conducted using the simulants (2-CEES and DMMP). Table 5.3 shows the results of permeation test for relative amount of the penetrated simulants through the protective clothing and the assemblies incorporated with MgO and POM. Briefly, the liquid simulants was dropped above the surface of circular-cut assembly specimen with the fixed ratio based on specimen area ( $10 \text{ g/m}^2$ ). Then, a cap covered the top of the specimen and simulants in order to limit escape of the evaporated gas simulants. The liquid simulant, located on the specimen, evaporated in the space covered by the cap, and then, the gas simulant crossed the specimen to the other side. The gas simulant, came out through the specimen, was delivered by  $\text{N}_2$  downstream flowing beneath the specimen. The delivered simulant gas was evaluated by thermal desorption gas chromatography with mass spectrometer (TD-GC-MS).

It was observed that a profile of penetration behavior of the simulants through the assembly by checking the amount of simulant at regular intervals as shown in Figure 5.6. Evaporated 2-CEES gas passed through the assembly with the fast speed of penetration and all mount of the gas penetrated for 6 hours at room temperature. Whereas, in the case of DMMP, the gas slowly and continuously passed through the sample 2-CEES for 12 hours. These results were attributed to difference in volatility between 2-CEES and DMMP. 2-CEES shows much

higher relative volatility ( $<3.4$  mmHg vapor pressure at  $25\text{ }^{\circ}\text{C}$ ,  $16,570\text{ mg/m}^3$  volatility at  $20\text{ }^{\circ}\text{C}$ ) compared to DMMP ( $\sim 1$  mmHg vapor pressure at  $25\text{ }^{\circ}\text{C}$ ,  $347\text{ mg/m}^3$  volatility at  $20\text{ }^{\circ}\text{C}$ ). The penetration behavior of simulants was observed similarly in the cases of the assembly with POM and the protective clothing (data not shown).

The protectability against simulants of the assembly, composed of inner and outer layers, was examined according to the TOP 8-2-501 method. The assembly with 2 sheets of outer layers and 8 sheets of inner layers were excluded the evaluation because it showed lower performance in physical property of weight density and moisture permeability. As shown in Table 6.3, the permeabilities of the currently used permeable protective clothing for Korea Army,  $383\text{ }\mu\text{g/cm}^2$  against 2-CEES and  $186\text{ }\mu\text{g/cm}^2$  against DMMP, were exhibited after 12 hours. This result was similar to the permeability of the assembly with 2 sheets of outer layers and 4 sheets of inner layers containing MgO. It indicates that the assembly had a comparable level of protectability compared to the protective clothing despite thin thickness and lightweight. In addition, the assembly exhibited better moisture permeability, cool/warm feeling than the protective clothing. In the case of the assembly with 2 sheets of outer layers and 4 sheets of inner layers containing POM, it showed higher protectability than the protective clothing. These results indicates that the layers based on nanofibrous composites can be applied to make a lighter

protective clothing materials. Furthermore, the assembly with 2 sheets of outer layers and 6 sheets of inner layers, which had comparable weight density to the protective clothing, provided an improved protectability against the simulants. This means that only one sheet of nanofibrous protective clothing material is much deficient to achieve the protectability, but the assembly with laminated layers can attain more effective protection against CWA than the currently used permeable protective clothing.

**Table 5.3.** Permeation test of the simulant of chemical warfare agents through the assemblies

	Permeable protective clothing with Outer and Inner layers for Korea Army			Assembly with Outer and Inner Layers containing MgO		Assembly with Outer and Inner Layers containing POM	
	2-CEES penetration ( $\mu\text{g}/\text{cm}^2$ )	DMMP penetration ( $\mu\text{g}/\text{cm}^2$ )		2-CEES penetration ( $\mu\text{g}/\text{cm}^2$ )	DMMP penetration ( $\mu\text{g}/\text{cm}^2$ )	2-CEES penetration ( $\mu\text{g}/\text{cm}^2$ )	DMMP penetration ( $\mu\text{g}/\text{cm}^2$ )
Assembly with outer layers (O) and inner layers (I)	382.99	185.52	O 2 sheets + I 2 sheets	771.25	323.67	744.82	311.12
			O 2 sheets + I 4 sheets	362.53	126.30	178.21	60.38
			O 2 sheets + I 6 sheets	251.71	108.72	161.53	52.65



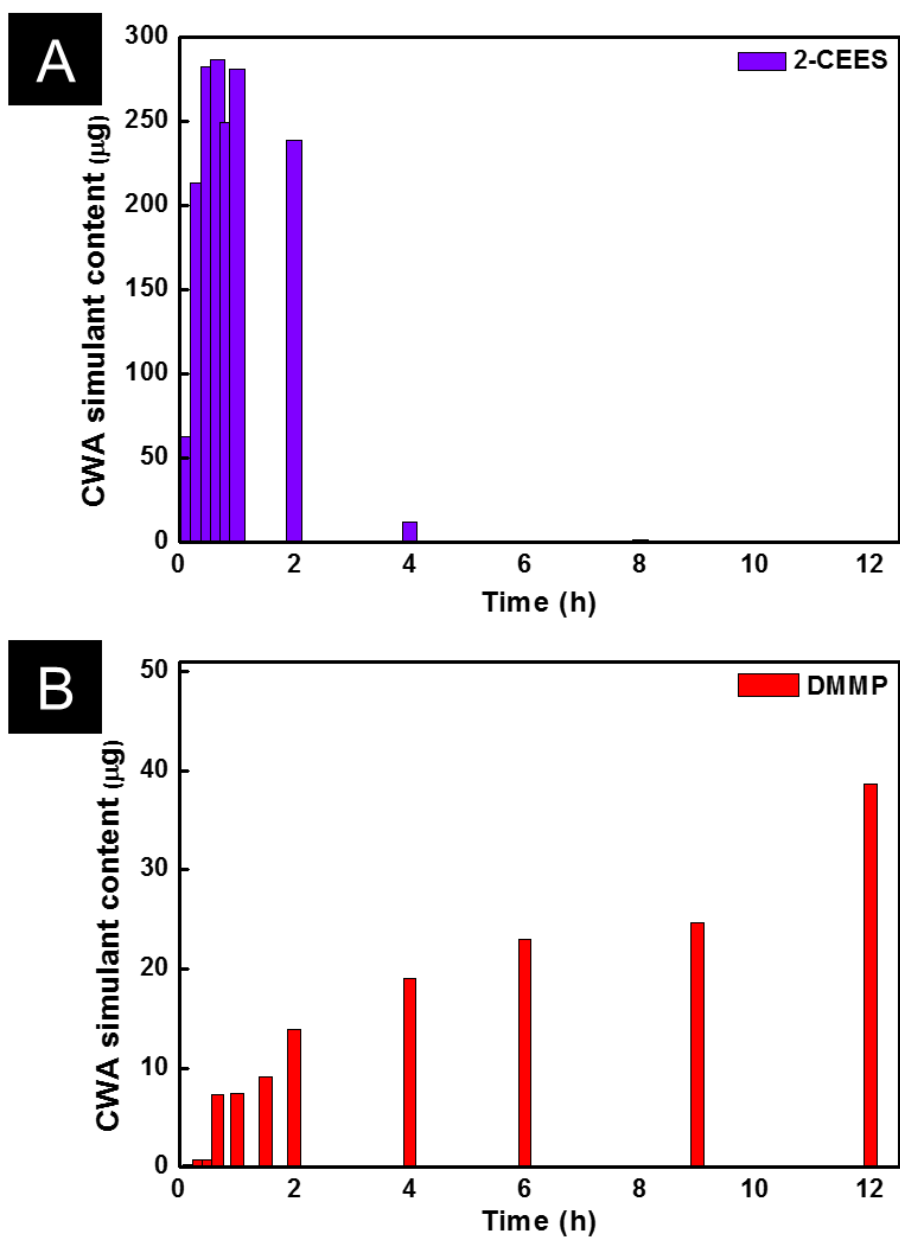


**Figure 5.6.** Penetration behavior of CWA simulants through the assembly containing MgO: (A) 2-CEES and (B) DMMP.

## 5.4 Summary

This study presented the development of the assemblies of several laminated layers with nanofiber composites, and the evaluation of protectability of them against the CWA simulants (2-CEES and DMMP). The multiplied assemblies was fabricated via spray- and heat-bonding process with stacking of the outer and inner layers, which were based on the nanofibrous composite mats made by the simultaneous electrospinning and electrospraying method. The physical properties of the assemblies, such as thickness, weight density, air/moisture permeability, and cool/warm feeling, can be controlled by the number of stacked layers. The assemblies showed high protection ability against CWA simulants because of the repellency by the outer layers and adsorption by the inner layers. Protective clothing materials with lighter weight or higher protection ability can be produced by controlling the number of stacked layers. The assemblies can provide good protection against CWAs, while still allowing considerable water vapor transmission to promote evaporative cooling of the body. Based upon these results, assemblies composed of the nanofibrous composite mats can be used as a protective material against various contaminants such as organic pollutants and harmful particulates, as well as against CWAs. These results will enable the design and production of permeable protective clothing with superior performance to that currently available.

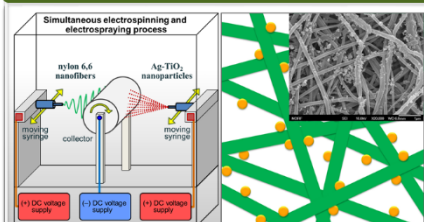
## References

1. *NATO Handbook on the Medical Aspects of NBC Defensive Operations*; Department of the Army; Washington, DC: HQ, DA; AMedP-6, Part 3; **1996**, 1–1. Field Manual 8–9.
2. Szinicz, L. *Toxicology* **2005**, *214*, 167.
3. Dickson, E. F. G. *J. Toxicol. Env. Health Part A* **2008**, *71*, 1382.
4. Gao, P.; King, W. P.; Shaffer, R. J. *Occup. Environ. Hyg.* **2007**, *4*, 562.
5. Pal, T.; Griffin, G. D.; Miller, G. H.; Watson, A. P.; Daugherty, M. L.; Vodinh, T. *J. Hazard. Mater.* **1993**, *33*, 123.
6. Liu, D. K.; Wannemacher, R. W.; Snider, T. H.; Hayes, T. L. *J. Appl. Toxicol.* **1999**, *19*, S41.
7. *Military Textiles*; Wilusz, E. Ed.; Woodhead Publishing Limited: England, **2008**.
8. Ramaseshan, R.; Sundarrajan, S.; Liu, Y.; Barhate, R. S.; Lala N. L.; Ramakrishna, S. *Nanotechnology* **2006**, *17*, 2947.
9. Sundarrajan, S.; Ramakrishna, S. *J. Mater. Sci.* **2007**, *42*, 8400.
10. Wagner, G. W.; Bartram, P. W.; Koper, O.; Klabunde, K. J. *J. Phys. Chem. B* **1999**, *103*, 3225.
11. Mahato, T. H.; Prasad, G. K.; Singh, B.; Batra, K.; Ganesan, K. *Microporous Mesoporous Mat.* **2010**, *132*, 15.
12. Mahato, T. H.; Prasad, G. K.; Singh, B.; Acharya, J.; Srivastava, A. R.; Vijayaraghavan R. *J. Hazard. Mater.* **2009**, *165*, 928.
13. Prasad, G.K.; Mahato, T.H.; Singh, B.; Ganesan, K.; Pandey, P.; Sekhar, K. *J. Hazard. Mater.* **2007**, *149*, 460.
14. Panayotov, D. A.; Morris, J. R. *J. Phys. Chem. C* **2009**, *113*, 15684.
15. Ramaseshan, R.; Ramakrishna, S. *J. Am. Ceram. Soc.* **2007**, *90*, 1836.

16. Neațu, Ș.; Pârvulescu, V.I.; Epure, G.; Petrea, N.; Șomoghi, V.; Ricchiardi, G.; Bordiga, S.; Zecchina, A. *Appl. Catal. B-Environ.* **2009**, *91*, 546.
17. Grandcolas, M.; Sinault, L.; Mosset, F.; Louvet, A.; Keller, N.; Kellera, V. *Appl. Catal. A-Gen.* **2011**, *391*, 455.
18. Cojocaru, B.; Neațu, Ș.; Pârvulescu, V. I.; Șomoghi, V.; Petrea, N.; Epure, G.; Alvaro, M.; Garcia, H. *ChemSusChem* **2009**, *2*, 427.
19. Neațu, Ș.; Cojocaru, B.; Pârvulescu, V. I.; Șomoghi, V.; Alvaro, M.; Garcia, H. *J. Mater. Chem.* **2010**, *20*, 4050.
20. Smith, B. M. *Chem. Soc. Rev.* **2008**, *37*, 470.
21. Koper, O.; Lucas, E.; Klabunde, K. J. *J. Appl. Toxicol.* **1999**, *19*, S59.
22. Ferguson-McPherson, M. K.; Low, E. R.; Esker, A. R.; Morris, J. R. *Langmuir* **2005**, *21*, 11226.
23. Okun, N. M.; Tarr, J. C.; Hilleshiem, D. A.; Zhang, L.; Hardcastle K. I.; Hill, C. L. *J. Mol. Catal. A-Chem.*, **2006**, *246*, 11.
24. Yoneda, M.; Kawabata, S. *J. Text. Mach. Soc. Japan* **1985**, *31*, 79.
25. Test Operations Procedure 8-2-501, Permeation and penetration of air-permeable, semipermeable and impermeable materials with chemical agents or simulants (specimen testing), U.S. Army Dugway Proving Ground, UT, March 1997 (Unclassified Report AD A322329).
26. Kirsch, A. A.; Stechkina, I. B.; Fuchs, N. A. *Aerosol Sci.* **1974**, *5*, 39.
27. *Aerosol Technology*; Hinds, W.; Wiley, New York, **1982**.
28. Zhao, J.; Dai, C.; Fang, J.; Feng, X.; Yan, L.; Zhao, M. *Colloid Surf. A-Physicochem. Eng.* **2014**, *448*, 93.

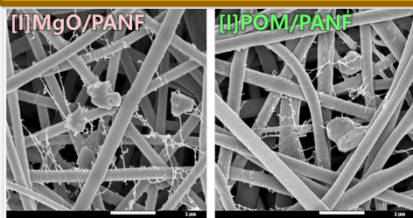
## Conclusion

### Chapter 2 Ag-TiO<sub>2</sub> Decorated Nylon 66 Nanofibrous Protective Materials with both Self-cleaning and Antimicrobial Activities



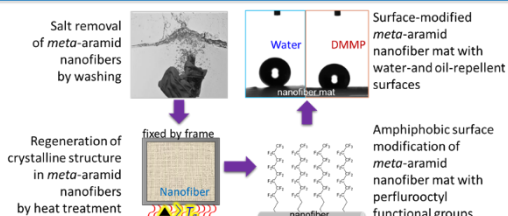
- ◇ **AT-sur-NF with Ag-TiO<sub>2</sub> exposed on the nanofiber surface had both better photocatalytic and antimicrobial activities** than AT-in-NF with Ag-TiO<sub>2</sub> located inside the nanofiber, although the Ag-TiO<sub>2</sub> content in the two types of nanofiber composite was controlled to be the same.
- ◇ **The position of Ag-TiO<sub>2</sub> plays an important role in the performance of nanofiber composites.**

### Chapter 3 Nanofibrous Inner Layer of Chemical Warfare Protective Materials with Adsorptivity of Chemical Warfare Agents



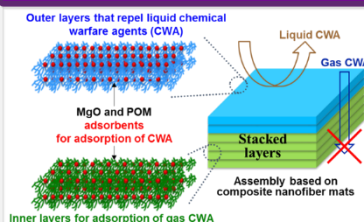
- ◇ **The nanofiber composites exhibited the superior moisture permeability** compared to the inner layer of permeable protective clothing of Korea Army.
- ◇ The nanofiber composites showed a better protectability than that of neat polyamide nanofiber.
- ◇ The use of just one sheet with thickness of 91  $\mu\text{m}$  was inadequate to protect from the CWA.

### Chapter 4 Nanofibrous Outer Layer of Chemical Warfare Protective Materials with Repellency of Chemical Warfare Agents

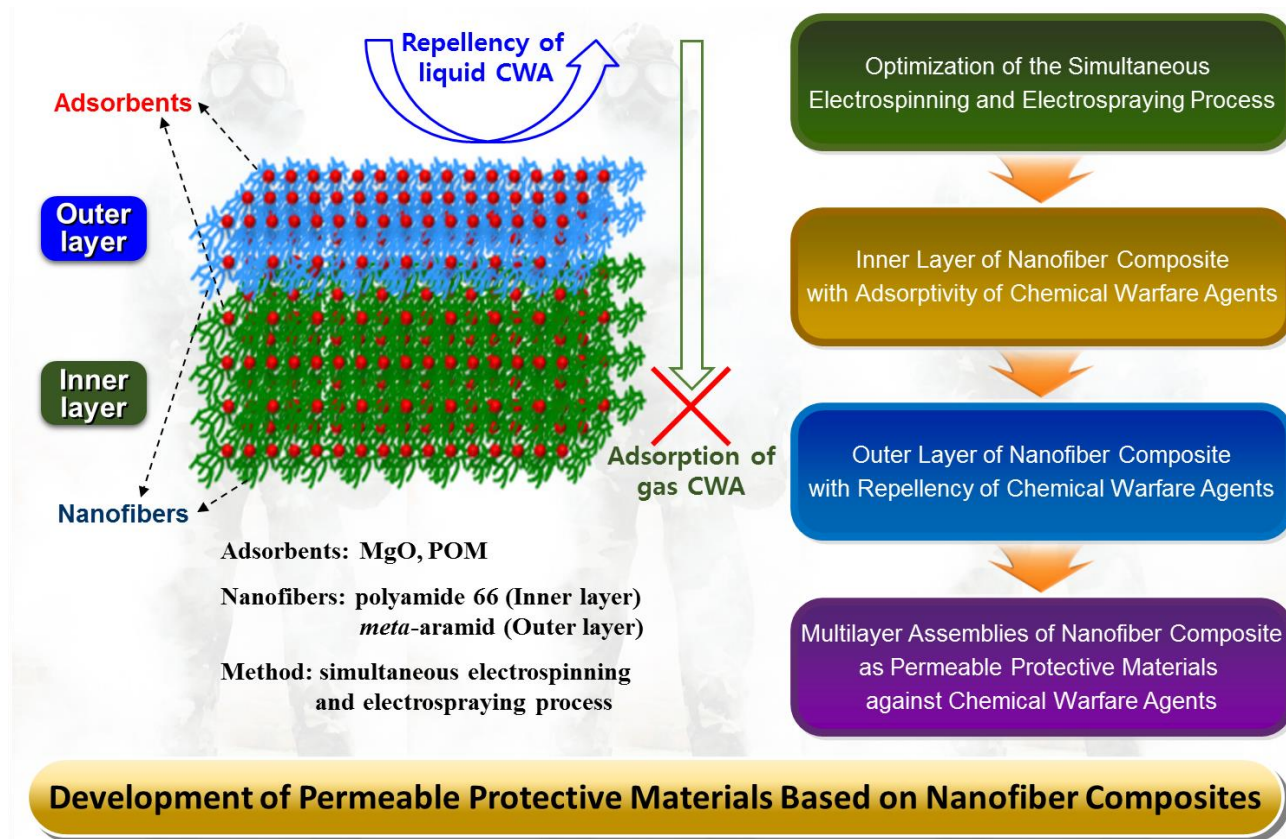


- ◇ **Improvement of the chemical stability and mechanical properties of meta-aramid nanofibers is a prerequisite for many practical applications requiring high durability.**
- ◇ **The amiphobic meta-aramid nanofiber mat can be applied as a protective material against liquid CWA.**

### Chapter 5 Multilayer Assemblies of Nanofibrous Composite Mats as Permeable Protective Materials against Chemical Warfare Agents



- ◇ Protective clothing materials with **lighter weight or higher protection ability** can be produced by **controlling the number of stacked outer and inner layers.**
- ◇ The assemblies can provide **good protection against CWAs**, while still allowing **considerable water vapor transmission** to promote evaporative cooling of the body.



## Korean Abstract

나노소재(nanomaterial)는 기존 소재 대비 우수한 물리적, 화학적 특성을 지닌다. 이에 나노입자(nanoparticle), 나노로드(nanorod), 나노스피어(nanosphere), 나노섬유(nanofiber) 등과 같은 다양한 형태의 나노소재에 대한 연구가 활발하게 진행되고 있다. 이처럼 새로운 기능성 나노소재를 개발하는 것은 나노과학과 나노기술의 혁신에 매우 크게 공헌한다. 다양한 나노소재 중 전기방사(electrospinning)를 이용한 나노섬유는 부피 대비 높은 비표면적(high surface to volume ratio), 다공성(porosity) 등의 특징으로 인해 새로운 기능성 소재로 큰 주목을 받고 있다. 나노섬유를 여과(filtration), 조직공학(tissue engineering), 보호소재(protective material), 전기 및 광학소재(electronic and photonic material), 약물전달(drug delivery) 등 다양한 분야에 적용하기 위한 연구가 활발하게 진행되고 있다. 본 연구에서는 전기방사와 전기분무 방법을 동시에 활용하여 고분자 나노섬유 복합체(polymeric nanofiber composite)를 개발하고, 이의 보호소재로의 적용가능성을 평가하였다.

2장에서는 Ag-TiO<sub>2</sub> 나노입자가 나노섬유 내부, 외부에 존재하는 두 종류의 나노섬유 복합체를 소개하였다. 나노입자가 나노섬유 표면에 존재하는 경우 나노입자가 나노섬유 내부에 존재하는 경우 대비 광활성(photocatalytic activity)을 통한 메틸렌블루(methylene blue) 분해와 은(Ag)으로 인한 항균성 발현이 더 우수하게 나타나는 것을 확인하였다.

이를 통해 기능성 나노소재의 위치(position)가 복합나노섬유 소재의 성능 발현에 매우 중요한 인자임을 제시하였다.

3장에서는 침투성 화생방 보호복(permeable protective clothing against chemical warfare agents) 소재로 활용하기 위한 내피용 나노섬유 복합체를 소개하였다. 내화화성이 우수한 지방족 폴리아미드(aliphatic polyamide) 나노섬유의 표면에 화학작용제 방호기능을 지닌 산화마그네슘(magnesium oxide, MgO)과 폴리옥소메탈레이트 (polyoxometalate, POM)를 도입한 나노섬유 복합체를 각각 제조하고, 이들이 지닌 공기투과도, 투습도, 기체 화학작용제 유사체(chemical warfare simulant)에 대한 보호성능(protectability)을 평가하였다. 이를 통해 해당 나노섬유 복합체의 화생방 보호복 내피(inner layer)로의 활용가능성을 확인하였다.

4장에서는 액체 형태 화학작용제의 외부로부터의 유입을 막기 위하여, 내화화성과 물리적 특성이 증대된 방향족 폴리아미드(aromatic polyamide) 나노섬유로 제조하고, 이의 표면에 발수 및 발유성(water and oil repellency)을 부여하였다. 이를 통해 화생방 보호복 외피(outer layer)로 활용가능한 나노섬유 복합체를 개발하였다.

5장에서는 3장과 4장에서 소개한 나노섬유 복합체들을 수 겹으로 적층하여 다층형 조립체(multilayer assembly)를 제조하였다. 다층형 조립체의 두께, 중량감, 접촉냉온감, 공기투과도, 수투과도 등 다양한 물성을 현재 활용하고 있는 침투성 화생방 보호복 소재와 비교,



평가하였다. 특히 다층형 조립체는 적층수의 조절을 통해 두께 및 중량감을 자유자재로 조절할 수 있으며, 현용 침투성 화생방 보호복 대비 우수한 투습도와 접촉냉온감을 지녔을 뿐만 아니라 기체 및 액체 형태의 화학작용제 유사체에 대한 뛰어난 보호성능을 지녔다. 이와 같은 나노섬유 복합체 기반 다층형 조립체는 침투성 보호복 소재의 보호성능 및 활용성을 향상시킬 수 있는 새로운 기능성 소재로 활용할 수 있다. 아울러, 이러한 연구결과는 침투성 보호복 소재의 설계 및 최적화에 성공적으로 기여할 수 있을 것으로 전망한다.

주요어: 나노섬유, 복합체, 전기방사, 전기분무, 폴리아미드,  
메타-아라미드, 보호소재, 발수성, 발유성, 화학작용제,  
화학작용제 유사체.

학번: 2006-20861

## List of papers, patents and symposiums

### PAPERS

1. Su-Yeol Ryu, Dong Suk Kim, Jae-Deok Jeon, and Seung-Yeop Kwak, Pore Size Distribution Analysis of Mesoporous TiO<sub>2</sub> Spheres by <sup>1</sup>H Nuclear Magnetic Resonance (NMR) Cryoporometry, *Journal of Physical Chemistry C*, 2010, 114, 17440–17445.
2. Su-Yeol Ryu and Seung-Yeop Kwak, Role of Electrical Conductivity of Spinning Solution on Enhancement of Electrospinnability of Polyamide 6,6 Nanofibers, *Journal of Nanoscience and Nanotechnology*, **2013**, 13, 4193–4202.
3. Su-Yeol Ryu, Myung-Kyu Park, and Seung-Yeop Kwak, Silver-Titania/Polyurethane Composite Nanofibre Mat for Chemical and Biological Warfare Protection, *International Journal of Nanotechnology*, **2013**, 10, 771–788.
4. Jo-Il Kim, Su-Yeol Ryu, Jong-Min Park, Joo-Yoon Noh, Min-Jung Kang, Seung-Yeop Kwak and Jae-Chul Pyun, Nylon Nanoweb with TiO<sub>2</sub> Nanoparticles as a Solid Matrix for Matrix-Assisted Laser Desorption/Ionization Time-of-flight Mass Spectrometry, *Rapid Communications in Mass Spectrometry*, **2014**, 28, 2427–2436.  
(Co-First Author)

5. Su-Yeol Ryu, Jae Woo Chung and Seung-Yeop Kwak, Probing the Role of Side-chain Interconnecting Groups in Structural Hydrophobicity of Comb-like Fluorinated Polystyrene by Solid State NMR Spectroscopy, *Langmuir*, **2015**, *31*, 9473–9482.
6. Su-Yeol Ryu, Jae Woo Chung and Seung-Yeop Kwak, Dependence of Photocatalytic and Antimicrobial Activity of Electrospun Polymeric Nanofiber Composites on the Positioning of Ag-TiO<sub>2</sub> Nanoparticles, *Composite Science and Technology*, **2015**, *117*, 9–17.
7. Su-Yeol Ryu, Myung-Kyu Park, and Seung-Yeop Kwak, Effect of Salt Removal and Heat-Pressing Treatments on Mechanical Properties of Electrospun *Meta*-Aramid Nanofibers, *International Journal of Nanotechnology*, **2015**, *13*, 426–437.
8. Su-Yeol Ryu, Jae Woo Chung and Seung-Yeop Kwak, Amphiphobic *Meta*-Aramid Nanofiber Mat with Improved Chemical Stability and Mechanical Properties, *Polymer*, under review.
9. Su-Yeol Ryu, Jae Woo Chung and Seung-Yeop Kwak, Tunable Multilayer Assemblies of Nanofibrous Composite Mats as Permeable Protective Materials against Chemical Warfare Agents, *ACS Applied & Interfaces*, under review.

## PATENTS

1. 곽승엽, 전재덕, 류수열, 미세다공성 티타늄실리케이트 입자를 포함하는 직접메탄올연료전지용 고분자 전해질막 및 그 제조 방법과 이를 사용하는 막전극 접합체 및 직접메탄올 연료전지, 대한민국 특허등록번호 10-0896111 (2009. 4. 27)
2. 곽승엽, 정재우, 류수열, 이아름, 알파-사이클로덱스트린 관형집합체의 제조방법 및 알파-사이클로덱스트린 관형집합체 번들 응집체, 대한민국 특허등록번호 10-0916051 (2009. 8. 31)
3. 곽승엽, 전재덕, 류수열, 황산화 사이클로덱스트린 및 미세다공성 티타늄실리케이트 입자를 포함하는 직접메탄올 연료전지용 고분자 전해질막 및 그 제조방법과 이를 사용하는 막전극 접합체 및 직접메탄올 연료전지, 대한민국 특허등록번호 10-0953720 (2010. 4. 12)
4. 곽승엽, 류수열, 황산화 이산화티탄을 포함하는 직접메탄올 연료전지용 전해질막 및 그 제조방법과 이를 사용하는 막전극 접합체 및 직접메탄올 연료전지, 대한민국 특허등록번호 10-1100897 (2011. 12. 23)
5. 곽승엽, 류수열, 항균 및 유해물질분해 기능성 나노섬유매트 및 그 제조방법과 이를 구비하는 보호장구, 대한민국 특허등록번호 10-1290715 (2013. 7. 23)
6. 곽승엽, 류수열, 화학작용제 흡착제거를 위한 기능성 재료가 도입된 나노섬유웹 및 그 제조방법과 이를 사용하는 화학작용제 보호의, 대한민국 특허출원번호 10-2009-0110283 (2009. 11. 16)

## SYMPOSIUMS

1. 춘계 고분자학회 (2008), Preparation and Characterization of Nafion/Sulfated Titanium Dioxide Composite Membrane by In-situ Hydrothermal Crystallization for Direct Methanol Fuel Cells.
2. Nanoporous Materials-V (2008), Ionic Cluster Pore Size Distributions of Porous Nafion Membranes in Aqueous Environments Measured by  $^1\text{H}$  NMR Cryoporometry.
3. International Conference on Intelligent Textiles (2008), Preparation of Nafion/Sulfated-Titanium Dioxide Nanocomposite Membrane Using *in situ* Hydrothermal Crystallization for Direct Methanol Fuel Cells.
4. 춘계 고분자학회 (2009), Preparation and Characterization of Carbon Nanotube/Polyurethane-Nanofiber Composite for Adsorption-Removal of Blister Agents.
5. 추계 고분자학회 (2009),  $^{19}\text{F}$  Solid-state NMR Study of Molecular Mobility in Comb-Like Fluorinated Polystyrenes Having Different Side Chain Interconnecting Groups.
6. 춘계 고분자학회 (2010), Ag-TiO<sub>2</sub> spreaded Nylon 66 Composite Nanofiber Web for Chemical Warfare Protective Clothing.
7. Nanotech 2010 (2010), Ag-TiO<sub>2</sub> Coated Polyurethane Composite Nanofiber Web for Application in the Protection against Chemical and Biological Warfare Agent.

8. 추계 고분자학회 (2010), Synthesis of Ag-TiO<sub>2</sub> Nanocomposite by Photoreduction of Ag on TiO<sub>2</sub> and Its Application to Polymer Nanofiber Mat.
9. ACS 241st National Meeting (2011), Synthesis of Ag-TiO<sub>2</sub> by Photoreduction of Ag<sup>+</sup> ions on TiO<sub>2</sub> and Its Application to chemical-biological protective textile based on electrospun nanofibers.
10. The 11th Asian Textile Conference (2011), Composite Nanofiber Mat with Transition Metal Incorporated Mesoporous TiO<sub>2</sub> for Protective Clothing against Chemical and Biological Warfare Agents.
11. 지상무기학술대회 (2012), Preparation of Composite Nanofiber Mat with Ag-TiO<sub>2</sub> photocatalyst and Its Application to Chemical-Biological Protective Clothing.
12. 춘계 고분자학회 (2012), Optimal Electrospinning Conditions for Polyamide 6,6 Nanofibers: Effect of Electrical Conductivity.
13. International Textile Conference 2013 Commemorating the 50th anniversary of The Korean Fiber Society (2013), Fabrication of Titanium Dioxide/Polyurethane Composite Nanofiber Mats and Its Photocatalytic Performance.
14. 한국군사과학기술학회 (2013), Preparation of Composite Nanofiber Mat with Multi-walled Carbon Nanotube and Evaluation of Protection against Chemical Warfare Agent Simulant.

15. Hong Kong International Conference on Engineering & Applied Science (2013), Electrospinning of Nylon 6,6 Nanofibers: Effect of Organic Salt Addition on Morphology and Electrospinning Conditions.
16. 한국군사과학기술학회 (2014), Composite Nanofiber Mat against Chemical Warfare Agent.
17. 지상무기학술대회 (2014), Preparation of Nanofiber Composites and Its Application to Protective Clothing Materials against Chemical Warfare Agent.
18. Fiber Society Spring Conference (2015), Electrospun Nanofiber Composite with Photocatalytic and Antimicrobial Activities.
19. 한국군사과학기술학회 (2015), Composite Nanofiber for Inner Shell of Protective Clothing against Chemical Warfare Agents.
20. 한국군사과학기술학회 (2016), Assembly of Nanofibrous Inner and Outer Layers for Protection against Chemical Warfare Agents.